

Measurement of Molecular Conductance

by

Shreya Bhattacharyya

A Dissertation Presented in Partial Fulfillment  
of the Requirements for the Degree  
Doctor of Philosophy

Approved June 2011 by the  
Graduate Supervisory Committee:

Stuart Lindsay, Chair  
Ana Moore  
Marcia Levitus

ARIZONA STATE UNIVERSITY

August 2011

## ABSTRACT

This dissertation describes the work on two projects which involves measuring molecular conductance and studying their properties on the nanoscale using various Scanning Tunneling Microscopy (STM) techniques. The first molecule studied was a porphyrin-fullerene moiety known as a molecular Dyad for photovoltaic applications. This project is further divided into two section, the first one involving the characterization of the Dyad monolayers and conductance measurement in the dark. The Dyads are designed to form charge separated states on illumination. The lifetime of the charged states have been measured efficiently but the single-molecule conductance through the molecules have yet to be characterized. The second part of the project describes the set-up of a novel sample stage which enables the study of molecular conductance under illumination. This part also describes the subsequent study of the molecule under illumination and the observation of a unique charge-separated state. It also contains the verification of the presence of this charge-separated using other characterization techniques like transient absorption spectroscopy. The second project described in the dissertation was studying and comparing the predicted rectifying nature of two molecules, identical in every way except for one stereocenter. This project describes the formation of monolayers of the molecule on gold and then studying and analyzing the current-voltage characteristics of the molecules and looking for

rectification. Both the molecules proved to be rectifying, one more than the other as predicted by theoretical calculations.

## ACKNOWLEDGEMENTS

I must thank all those that have helped me over the years. I would like to thank my advisor Stuart Lindsay for his patience. I want to thank my fellow graduate student, Dr. Ashley Kibel who has helped with out with the instrumentation. Dr. Iris Visoly-Fisher introduced me to the STM. Dr. Gerdenis Kodis helped me finish my project and my paper. Professor Devens Gust and Dr. Marcia Levitus was always available for discussions.

This is a shout-out to the "basement creatures" (especially Dr. Kaushik Gurunathan) and all my friends on campus.

I would like to thank my parents and my brother for everything.

This would not have possible without the support of my husband, Dr. Michael McCamy.

## TABLE OF CONTENTS

	Page
LIST OF FIGURES . . . . .	ix
CHAPTER 1 INTRODUCTION . . . . .	1
1.1 Self Assembled Monolayers . . . . .	2
Characterization of SAMs . . . . .	3
1.2 Instruments used in molecular electronics research . . . . .	4
Scanning Tunneling Microscopy . . . . .	6
Atomic Force Microscopy . . . . .	13
1.3 Molecular Electronics . . . . .	15
Electron energy levels in organic molecules . . . . .	17
Conductance of Nanostructures in a nano-junction . . . . .	20
Electron transport through single molecular wires tethered in a nano-junction . . . . .	22
Charge transfer (Marcus Theory) . . . . .	25
Experimental methods utilized in molecular electronics research .	27
Anchoring group effect in single molecule measuremennts . . . . .	30
CHAPTER 2 Organic Photovoltaics . . . . .	32
2.1 Energy crisis . . . . .	32
Potential of solar energy . . . . .	34

	Page
2.2 Energy conversion in photovoltaics . . . . .	35
Drawbacks of semiconductor photovoltaics . . . . .	38
2.3 Benefits of Organic Photovoltaics . . . . .	40
2.4 Challenges to Organic Photovoltaics . . . . .	41
2.5 Organic Photovoltaic Architecture . . . . .	43
The Grätzel Electrochemical Cell . . . . .	44
Transparent conducting oxides . . . . .	46
2.6 Mimicking Photosynthesis: Porphyrin based Molecular Dyads . .	48
CHAPTER 3 Molecular conductance measurement on novel substrate . .	52
3.1 The ITO Surface . . . . .	52
3.2 Verification of Suitability of ITO Surface for Break-junction Mea-	
surements . . . . .	54
Formation of alkane monolayers on ITO . . . . .	54
Measuring the electronic decay constant for alkanes on the ITO	
surface . . . . .	57
Conclusions . . . . .	63
3.3 Conductance Measurement of Dyads in the Dark . . . . .	63
Synthesis of significant molecules . . . . .	63
Dyad monolayer deposition . . . . .	65
Dyad monolayer calculation from absorbance spectra . . . . .	67

	Page
Dyad monolayer confirmation: X-ray photoelectron spectroscopy	70
Electrochemistry of Dyads: cyclic voltammetry . . . . .	71
Break-junction measurements . . . . .	72
Data analysis: "Step" analysis . . . . .	74
3.4 Conclusion . . . . .	77
CHAPTER 4 STM break junctions under illumination . . . . .	78
4.1 Experimental Set-Up . . . . .	78
Laser beam delivery . . . . .	78
Beam diameter measurement . . . . .	79
Illuminated STM . . . . .	80
Sensitivity of dyads to atmospheric oxygen . . . . .	82
4.2 Results . . . . .	83
Control experiments . . . . .	88
Spectroscopy . . . . .	90
4.3 Conclusion . . . . .	93
CHAPTER 5 Molecular Rectification . . . . .	97
5.1 Introduction . . . . .	97
5.2 Experimental procedure . . . . .	100
Molecular monolayers . . . . .	100
Molecular conductance measurements . . . . .	104

	Page
Data Analysis . . . . .	107
5.3 Conclusion . . . . .	110
CHAPTER 6 Conclusion . . . . .	111
6.1 Conclusion of project one . . . . .	111
6.2 Future directions of project one . . . . .	111
6.3 Conclusion of project two and future directions . . . . .	112
BIBLIOGRAPHY . . . . .	113



## LIST OF FIGURES

Figure	Page
1.1 Self-assembled monolayers . . . . .	2
1.2 Schematic of STM working principle. . . . .	7
1.3 STM tip. . . . .	9
1.4 Inverting operational amplifier. . . . .	10
1.5 Working principle of AFM . . . . .	14
1.6 Aviram-Ratner diode . . . . .	16
1.7 Single molecule wired between two electrodes . . . . .	23
1.8 Marcus energy diagram . . . . .	26
1.9 STM break junction . . . . .	28
1.10 STM break junction under potential control . . . . .	30
1.11 Decay constant determination from alkane molecules . . . . .	31
2.1 US fossil fuel consumption . . . . .	32
2.2 Potential of solar energy . . . . .	34
2.3 Photovoltaic working principle . . . . .	36
2.4 Comparison of solar cell efficiencies . . . . .	42
2.5 Grätzel cell . . . . .	45
2.6 Flourinated tin oxide . . . . .	47
2.7 Dyad molecule . . . . .	49

Figure	Page
3.1 STM image of Indium tin oxide . . . . .	52
3.2 Contact angle data . . . . .	55
3.3 Break junction histograms of alkanes . . . . .	58
3.4 Beta value . . . . .	62
3.5 Synthesis schematic for 5-(4-Carboxyphenyl)-20-(4-pyridyl)-10,15-bis(2,4,6-trimethylphenyl)porphyrin (II). . . . .	64
3.6 Synthesis schematic for dyad molecule. . . . .	65
3.7 Schematic of Dyad monolayer formation on ITO . . . . .	66
3.8 Absorbance spectra . . . . .	68
3.9 Angle resolved XPS data . . . . .	70
3.10 Cyclic Voltammetry of dyad III on ITO . . . . .	71
3.11 Raw data showing steps in the current-time traces. . . . .	73
3.12 Conductance histogram of dyads on ITO . . . . .	74
3.13 Conductance histogram of dyad after using step analysis program . . .	76
4.1 Beam diameter measurement. . . . .	79
4.2 Instrumentation of the illuminated STM set-up . . . . .	80
4.3 Schematic of break junction of molecules under illumination. . . . .	81
4.4 Molecules tested by illuminated break junction method . . . . .	84
4.5 Conductance histograms of Dyad in dark and under illumination . . .	85
4.6 Variation of excited molecules with laser power density . . . . .	86

Figure	Page
4.7 Conductance histogram of molecule I in dark and under illumination	88
4.8 Conductance histogram of molecule II in dark and under illumination	89
4.9 Spectroscopy of dyads on ITO . . . . .	91
4.10 Energy level diagram . . . . .	94
5.1 Aviram-Ratner molecule . . . . .	98
5.2 Molecules with identical molecular weight and formula but reversal in the direction of the amide bond . . . . .	101
5.3 Ellipsometry data of molecule 1 deposited on gold . . . . .	103
5.4 I-V curves of molecule 1 on gold . . . . .	105
5.5 Fraction of the total I-V curves showing rectification at the current set-point of 0.2 nS. . . . .	107
5.6 Fraction of the total I-V curves showing rectification at the current set-point of 1.4 nS for molecule 1. . . . .	108
5.7 Fraction of the total I-V curves showing rectification at the current set-point of 1.4 nS for molecule 2 and control at set-point of 0.2 nS. . .	109

## Chapter 1

### INTRODUCTION

Nanostructured molecular architectures for energy conversion are potential alternatives to solid state devices. This dissertation will look at molecules that could be applied as light energy harvesting assemblies in photovoltaic devices. The entire work will be broadly divided into two main projects. The first project (project one) involves measuring photoconductance of a covalently bound donor-acceptor assembly and will be narrated in Chapters 3 and 4. The second project (project two) looks at rectification in a set of molecules with a dipole for photovoltaic applications. Chapters 1 and 2 are dedicated to understanding molecular electronics and the instruments and techniques utilized in this field.

The first part of Chapter 1 will go into the details of self-assembled monolayers (SAMs) and a description of one of the analytical instruments and techniques used to characterize them, namely optical ellipsometry (Note: there are many techniques to characterize SAMs, the details of which are beyond the scope of this dissertation). The second part of the chapter describes the tools utilized in molecular electronic research. It will look into the working of the Scanning Probe Microscope (SPM), namely the Scanning Tunneling Microscope (STM) and the Atomic Force Microscope (AFM). Details will be provided on the individual components that make up the instruments as a thorough understanding is required for the ad-

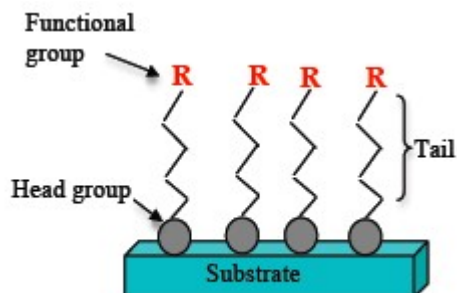


Figure 1.1: Self-assembled monolayers on a substrate.

vanced experimental techniques employed in studying single molecule junctions. The third part of the chapter describes the theory of molecular electronics. It starts with a look at molecular orbitals and then goes into the theories that govern electron transport and transfer in a single molecule. Finally, this section ends with a discussion of some of the techniques that have been used to probe a single molecule wired in between two electrodes.

## 1.1 Self Assembled Monolayers

Self-assembled monolayers (SAMs) are ubiquitous to the field of chemistry, nanotechnology and molecular electronics. These systems are composed of a head group that attaches strongly to a surface (gold is an example of a surface that been studied extensively but molecules self-assemble on a wide variety of surfaces) (Berger et al., 1997; Nuzzo and Allara, 1983), and an alkyl chain that may or may not contain other functional groups. SAMs based on alkanethiols are very

well ordered on the molecular scale, and their ease of preparation and robustness lend them to both research and application (Schoenfish and Pemberton, 1998). Molecular conductance through these chains is of particular interest in the field of nanoscale molecular electronics. Better understanding and quantification of electron transfer within these molecular frameworks enable more unique and novel applications in the future (Fan et al., 2002). However, SAMs are not restricted to alkanethiols and can be extended to any molecule that will self-assemble to form a well-ordered monolayer (Dhirani et al., 1996). Scanning tunneling microscopy (STM) is ideally suited for these types of measurements because it is based on electron tunneling which is very sensitive to small changes in distance between the STM tip and surface and can measure very small surface features including atoms and adsorbed molecules (Poirier, 1997). STM has the capability to both spatially select and make direct electronic measurements of molecules supported on a surface.

### *Characterization of SAMs*

Various tools have been utilized to characterize SAMs. One of the techniques used to describe and characterize their physical properties is explained below:

Ellipsometry: Ellipsometry is an optical technique utilized for the investigation of dielectric properties of thin films. For the purpose of this dissertation, it will be used to measure the number of monolayers on a particular surface (like gold).

Ellipsometry uses a system that determines the amount of layers based on the optical refractive index. A laser is shot at the surface of the gold at a certain (given) phase angle. The light is then tracked by a detector which can then determine what the phase angle of the reflection is. Based on the preexisting (tested) values of the real (Ns) and imaginary (Ks) reflections of the light from the gold itself (done before the layers are grown on the sample), it can then determine the number of angstroms present on the surface of the gold created by the layers. Based on what is used to create the layers, the number of angstroms can be used to determine the exact number of layers present on the sample. Typically, ellipsometry is performed over a certain time interval (i.e. a number of hours). Periodically, the sample is tested under the ellipsometer for changes in the number of angstroms. Presented on an angstroms vs. time graphs, this tracks how fast and how much the number of layers increases.

## 1.2 Instruments used in molecular electronics research

In order to understand properties of molecules it is important to understand how they behave on the single molecular level. However, to conduct such precise measurements, it is mandatory to use instruments that are capable of reliably conducting nanoscale measurements. The discovery and development of scanning probe microscopy has paved the way for many important discoveries in the field

of molecular electronics.

Interacting with atoms and molecules on the nanoscale is not trivial and for a long time was the biggest hindrance in the development of nanoscience and nanotechnology. However, with the invention of Scanning Probe Microscopy (SPM) this problem went from being a concept to an achievable reality. Ever since its invention, SPM has grown in leaps and bounds and today it is used extensively to interact with nanoscale materials. The last three decades has seen some groundbreaking discoveries and breakthroughs employing the SPM.

Imaging and spectroscopy is not unique to the field of chemistry and physics. Scientists have been interacting with molecules and structures with the help of light and/or electrons to get information about them. However, what is unique to the SPM is that an actual probe is utilized to image the surface and molecules and interact with them. Thus, a lot of information about the surface topography could be obtained which were previously unattainable with spectroscopy and microscopy alone. The mechanism of interaction is different depending upon the type of microscopy and the imaging mode, but the generated signal is almost always highly correlated to features in the topography. Better still, in many forms of SPM, the probe does not have to come in physical contact with the surface so information can be obtained in a very non-intrusive way without destroying the sample. However, if required, the probe could be made to interact with the surface



as well, making it possible to watch chemical modifications and reactions being carried out in-situ. These myriad modifications possible with the SPM made it an indispensable tool to nanoscale science. Going back to imaging, the way it is done is by raster scanning with the SPM probe while keeping an interaction constant by adjusting the height of the probe. The height adjustment required the height of the surface at each point. The type of signal that is produced from the interaction between the probe and the surface determines what type of surfaces can be imaged and what the features in the image actually represent. The two main categories of scanning probe microscopy are scanning tunneling microscopy, which utilizes a tunneling current signal between probe and conductive surface, and atomic force microscopy, which utilizes the bending of a flexible cantilever as a surface sensor.

### *Scanning Tunneling Microscopy*

The Scanning Tunneling Microscope (STM) was invented by Binnig and Rohrer at IBM in 1981 (Binnig and Rohrer, 1983), an invention which won them the Nobel Prize. It is based on a principle in quantum mechanics called "electron tunneling", which we will talk about in great detail later. The instrument consists of a sharp conductive metallic probe that ideally has a single atom at its very end. The probe is slowly brought within a few nanometers of a conductive surface until the set point (which is a very small prefixed tunneling current and can be set by the software) is attained. For a bare conductive metal-

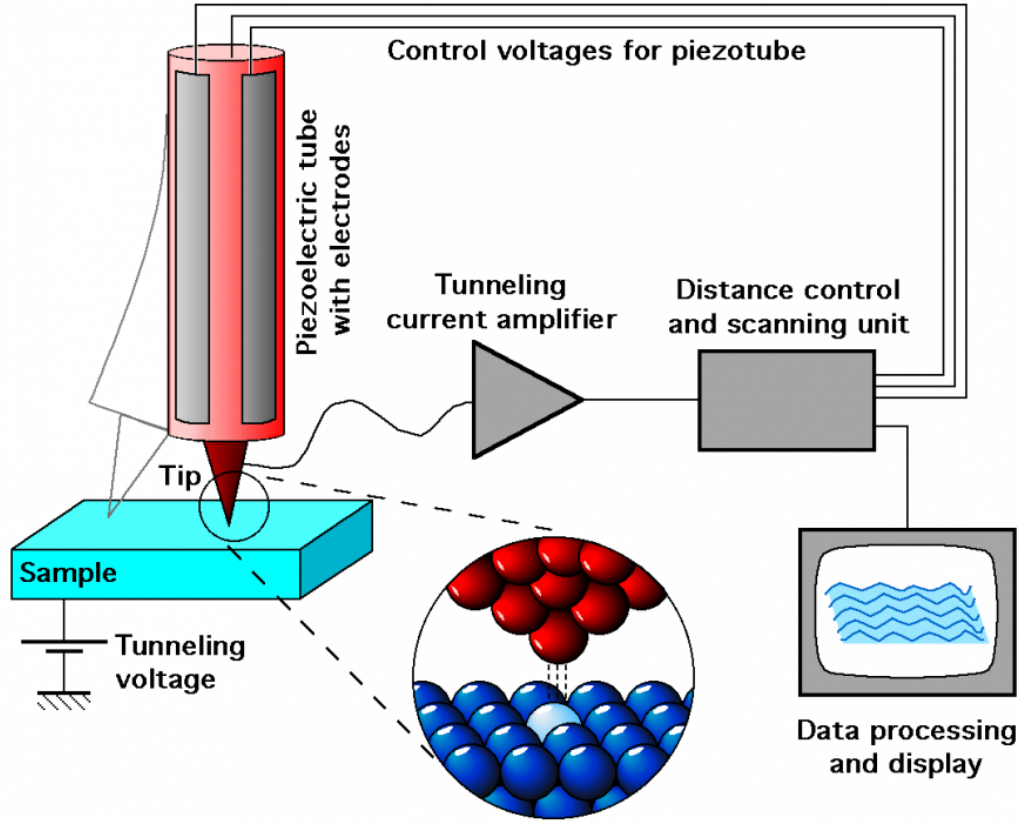


Figure 1.2: Schematic of STM working principle. Zoomed in region pictorially depicts the electron tunneling between the tip and the sample. (Figure modified from M. Schmidth, TU Wein STM gallery, 2005)

lic surface (like gold) the tunneling current ( $i$ ) is attained without actual physical contact to the surface. From the Schrodinger's equation, we know that the wavefunction for a particle to tunnel through a one dimensional potential barrier is  $\Psi(x) = A \exp\left(-\sqrt{\frac{2m(V-E)}{\hbar^2}}x\right)$ , where  $E$  is the energy of the particle and  $V$  is the potential barrier. The square of the wavefunction  $\Psi(x)^2 = A^2 \exp\left(-2\sqrt{\frac{2m(V-E)}{\hbar^2}}x\right)$  gives the probability of finding the particle in the one dimensional space. From the decaying wavefunction, the current in the tun-

nel gap is expected to decay as:

$$\exp - 2\sqrt{\frac{2m(V-E)}{\hbar^2}}x$$

After replacing the value of the constants in the previous equation, we get:

$$i = i_0 \exp - 1.02\sqrt{\phi}d \quad (1.1)$$

where  $d$  is the gap distance and  $\phi = V - E$  which is the work function of the metal electrode (in eV).

This implies that the tunneling current will increase/decrease exponentially as the STM tip is moved closer/further from the surface. When the current is held constant while scanning across a surface, the probe height is adjusted accordingly in response to the unevenness of the surface and thus we can get a high resolution image of the surface topography. Figure 1.2 pictorially depicts the working principle of the STM. The individual components and the instrumentation require further discussion. The probe used for imaging with the STM is known as the STM tip. It is typically made of gold or platinum which are inert metals and highly conductive. Tungsten has been widely used as well but suffer from the problem of getting oxidized readily when exposed to the atmosphere (Hockett and Creager, 1993). The STM tip has to be extremely sharp (single atom at the end) and hence is extremely fragile and has to be prepared before every experiment. The slightest mechanical contact with another surface is enough to cause damage to the the tip

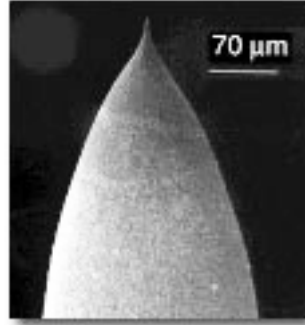


Figure 1.3: Transmission Electron Microscope image of a typical STM tip. The radius of curvature of the end of the tip should be less than 100 nm in order to get a good image. (Image from Agilent Technologies Ltd.)

and render it useless for the experiment.

It can be prepared by mechanically shearing a wire with a wire cutter (Baykul, 2000) or by electrochemical etching (Baykul, 2000; Nagahara et al., 1989). The resolution of the image obtained by the STM is limited by the radius of curvature of the STM tip. Figure 1.3 shows an STM tip electrochemically etched from a platinum-iridium wire (image from Agilent Technologies Ltd.) having a very sharp radius of curvature. In order to ensure a good image, the end of the tip has to be less than 100 nm, preferably less than 50 nm. Hence, the preferred method is electrochemical etching since it yields very sharp and symmetric tips and therefore reduces experimental artifacts.

The STM scanner contains a groove which can accommodate the STM tip. Now, the tunneling current between the tip and the surface is normally in the

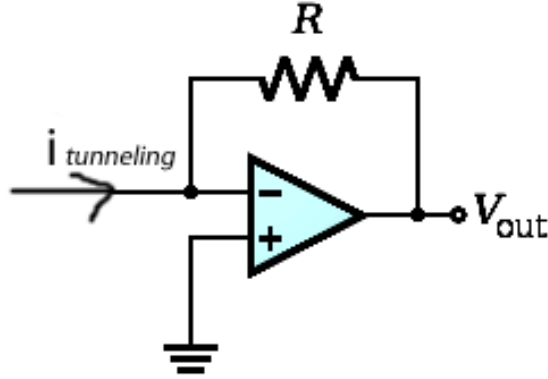


Figure 1.4: Circuit of an inverting operational amplifier. It takes the small tunneling current signal (input) and converts it into easily measurable voltages.

nanoampere range or even lower. To avoid stray noise pick-up, a current to voltage converter is built into the STM scanner. A current-voltage op-amp is a circuit that converts small current signals to a more easily measured proportional voltage.

Illustrated in figure 1.4 is an ideal op-amp. It has two characteristics that imply the operation of the inverting amplifier 1) infinite input impedance and 2) infinite differential gain. This essentially means that there is no current flowing through the op-amp and all the input current must be flowing through  $R$ . Also both the (+) and (-) pins are at the same voltage but the (+) pin is grounded and must be at 0 volts potential. This means that the (-) pin is also at 0 volts potential. For the STM, the input current is  $i_{\text{tunneling}}$ . From Ohm's law, we have

$$-i_{\text{tunneling}} = \frac{V_{\text{out}} - V_{\text{in}}}{R} \text{ where } V_{\text{in}} \text{ is grounded. So, the equation becomes}$$

$$-i_{\text{tunneling}} = \frac{V_{\text{out}}}{R}. \text{ Or } i_{\text{tunneling}} \text{ is proportional to the } V_{\text{out}} \text{ and this is a very}$$

important result. This preamplifier is housed within the scanner and its range can be switched between  $0.1 \frac{nA}{V}$  to  $100 \frac{nA}{V}$ . Most STM preamplifiers can be switched out easily depending on the range of the current being measured.

Another extremely important component of the STM scanner is the piezoelectric device controlling the height and  $x,y$  position of the tip. Piezoelectric devices are widely used to control the nanoscale movements required for imaging using the STM. Voltage changes produces mechanical deformations in the piezo which in turn controls the movement of the tip in a precise manner. The exact amount of the deformations depends on the material of the piezo. STM scanners are typically made from lead zirconium titanate (PZT) (Lindsay, 2010). Figure X shows the construction of a typical PZT element inside the STM scanner. The inside electrode is typically grounded so that changing the voltages on all the outer electrodes to a particular voltage causes the tube wall to either become thinner or thicker depending upon the sign of the applied voltage. This, in turn, causes the length of the tube to either grow or contract, since the volume of the tube remains constant. Applying different voltages on the coupled sets of electrodes around the outside of the tube can cause the tube to bend in the  $x$  and  $y$  axes, allowing for motion in the  $x$  and  $y$  directions.

In an STM experiment, the sample is pinned down/stuck onto a sample plate and manually positioned within a few millimeters of the tip. The tip is then made

to approach the surface automatically with the help of stepper motors until the predetermined set current is reached. To image a sample, either the tip can be raster scanned with the PZT to which it is attached while controlling tip height with the same PZT, or the sample can be raster scanned on a PZT stage while the height of the tip is adjusted to keep the tunneling current constant. This value for the voltage, required to adjust the PZT height, is converted by the software into an image of the topography as long as the calibration values of the scanner are known.

The applications of the STM are wide and far reaching. Perhaps the most widely known applications is that it can provide atomic resolution. Thus, individual atoms can be seen with this simple device. It can produce very accurate images for conductive surfaces and have been used to "grab" individual atoms and manipulate substances on the nanoscale. It had been applied to study semiconductor defects and has many other applications. However, the biggest drawback is that the surface has to be homogeneously conductive on the nanoscale. This made a lot of samples inaccessible for imaging with the STM. However, this problem was sorted out with the invention of the Atomic Force Microscope (AFM).

### *Atomic Force Microscopy*

The AFM was invented in 1986 by Binnig, Quate and Gerber (Binnig et al., 1986) and is in many ways similar to the STM. However, instead of a conductive tip that measures tunneling current, the AFM uses a flexible cantilever with a very sharp probe attached to its end and measures forces of attraction/repulsion between the probe and the surface. The force produces deflections in the cantilever and the deflections are measured by a laser which reflects off the back of the cantilever and gets recorded by a photodiode detector. Thus, the applications of the AFM are not restricted to conductors and semiconductors only but can be used on all kinds of surfaces. There are many modes of operation of the AFM. The most basic imaging mode is known as contact mode. As the name implies, this involves actual physical contact with the surface. Like the STM, a set point is predetermined and assigned but instead of current, it is a force set point. The tip/cantilever is approached to the surface until the cantilever registers the force and in this process it gets bent. The bending of the cantilever is measured by angular displacement of the laser beam which is reflected from the back of the cantilever. The force/bending is kept constant as the cantilever is scanned across the surface it is imaging. When the tip hits a hill or depression on the surface, this is registered as a change in the force of the tip-surface interaction. This is corrected



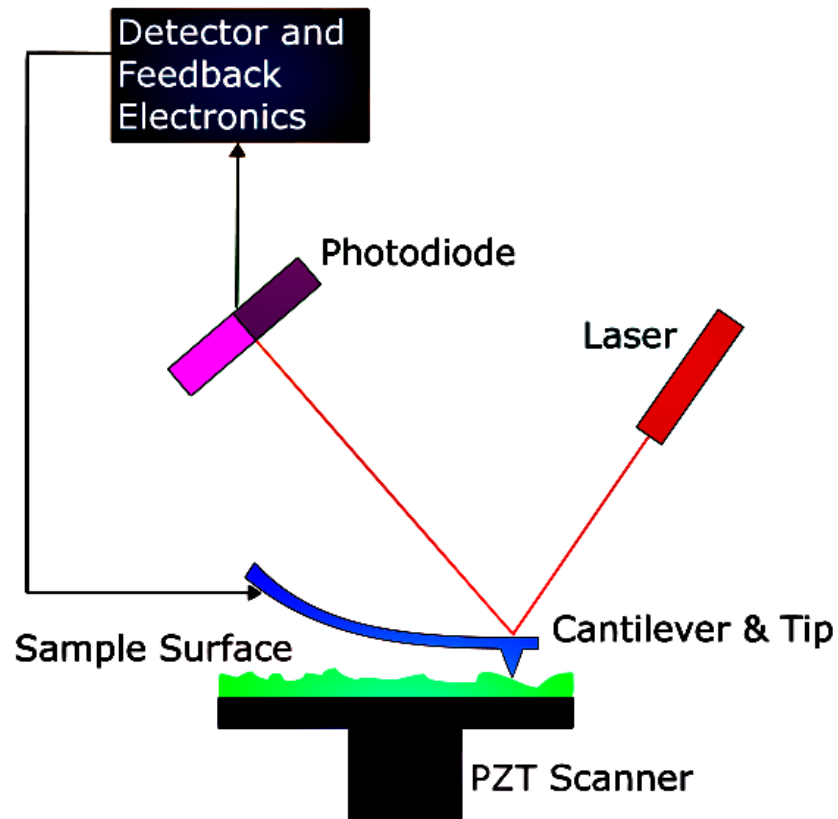


Figure 1.5: Schematic to illustrate the working principle of the atomic force microscope (Source: modified from Wikipedia)

quickly by applying a voltage to the piezo which then relieves or applies force to bring it back to the set point and topography of the surface is mapped out.

Another popular mode of imaging is known as the dynamic force microscopy. The most common form of dynamic force microscopy is referred to as amplitude modulation atomic force microscopy (AM-AFM) or tapping mode. Here, the tip is vibrated at a frequency close to its resonance and then the surface is approached to the tip. As the distance between the tip and sample decreases, it starts to dampen the cantilever vibrations. Then the vibration amplitude reaches a set

point and it is held constant while the tip moves across the surface and produces an image. The most common type of dynamic force microscopy is known as the intermittent contact mode or "tapping mode". As the name suggests, the cantilever literally taps on the surface making contact with the atoms and operating in both attractive and repulsive force regime. The vibration amplitude is held constant by the servo which detects changes in the force depending on how close to the surface the cantilever/tip is at. There are many other modes for AFM imaging and each has their own specific applications as well, but will not be discussed here.

### 1.3 Molecular Electronics

Molecular electronics, as the name suggests, involves the use of organic molecules and structures in electronic devices. Of late, a lot of research has been targeting the use of such molecules in actual devices. (Voss, 2000) There are many reasons for this growing trend. The size of organic molecules, for example, are usually between 1-100 nm, a scale that permits functional nanostructures. The molecules form self-assembled structures by intermolecular interaction which is another valuable property in molecular electronics (Ratner, 2002). Molecules can be synthesized according to the exact specification of the device and have the ability to be engineered to give the precise electrical responses necessary for applications (Gust and Moore, 1989). The synthesis and the starting materials are typically

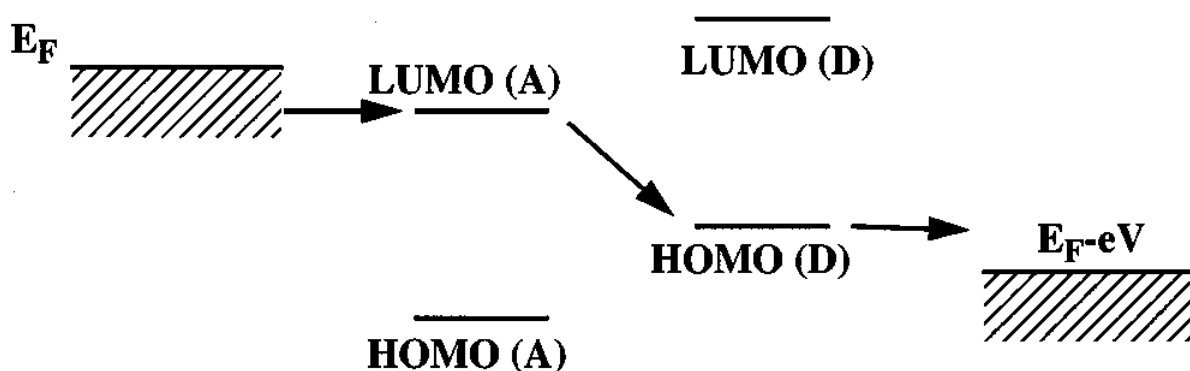


Figure 1.6: The Aviram-Ratner mechanism for molecular rectification.  $E_F$  refers to the Fermi levels of the electrodes. (A) stands for electron acceptor and (D) stands for electron donor (Aviram and Ratner, 1974).

much cheaper than conventional semiconductor devices. Simple rearrangements of these molecules can lead to fine tuning of the electrical device at the most basic level. Molecules can also recognize other molecules through chemical bonding or change behaviors depending on change in the solvent environment. Many of them are pretty robust and stable and not as sensitive to the environment as some solid state devices.

The concept of molecular electronics was illustrated in 1974 by Avi Aviram and Mark Ratner in a paper which outlined the design of an organic single molecule rectifier (Aviram and Ratner, 1974). The organic rectifier, like its solid-state counterpart, (see figure 1.6) would allow current to pass only in one direction when connected between two electrodes and biased in that particular direction. Since

the visionary theoretical prediction, a lot of research has been directed in using molecules to make transistors, rectifiers, switches, photovoltaics and other devices. (Nitzan, 2001) The synthesis and characterization of organic molecules have been done by chemists for many years. However, the key challenge in molecular electronics is to translate that solution-phase properties into a solid-state device setting. In order to do this, it is essential to understand the how electrons are transported through the molecules on the nanoscale. To get a complete picture of electron transport through organic molecules, it is important to understand molecular orbitals and energy levels with the aid of quantum mechanics.

### *Electron energy levels in organic molecules*

The electronic energy levels in a quantum system are given by the following equation:

$$E = \frac{\langle \psi | H | \psi \rangle}{\langle \psi | \psi \rangle} \quad (1.2)$$

Where  $\psi$  is the wavefunction and  $H$  is called the Hamiltonian. One method to solve for electronic states is to use a trial wavefunction and substitute in equation 1.2. For example:

$$\psi = \sum_i c_i f_i \quad (1.3)$$

And this trial function can be plugged into the equation for the energy, giving

$$E = \frac{c_1^2 \langle f_1 | H | f_1 \rangle + c_1 c_2 \langle f_1 | H | f_2 \rangle + c_2 c_1 \langle f_2 | H | f_1 \rangle + \dots}{c_1^2 \langle f_1 | f_1 \rangle + c_1 c_2 \langle f_1 | f_2 \rangle + \dots} \quad (1.4)$$

if we say  $H_{ij} = \langle f_i | H | f_j \rangle$  and  $S_{ij} = \langle f_i | f_j \rangle$  and  $H_{12} = H_{21}$  then the previous equation reduces to the form:

$$E = \frac{c_1^2 H_{11} + 2c_1 c_2 H_{12} + \dots}{c_1^2 S_{11} + 2c_1 c_2 S_{12} + \dots} \quad (1.5)$$

The coefficients are calculated by setting the energy to minimum, taking its derivative and equating it to zero. So we get the following matrix determinant which is equal to zero:

$$\begin{vmatrix} H_{11} - E_\phi S_{11} & H_{12} - E_\phi S_{12} & \dots \\ H_{12} - E_\phi S_{12} & H_{22} - E_\phi S_{22} & \dots \\ \vdots & \vdots & \ddots \end{vmatrix} = 0 \quad (1.6)$$

Obviously for complex molecules, solving this matrix can be incredibly difficult.

**Linear Combination of Atomic Orbitals (LCAO):** According to this method, a molecule is formed by the linear combination (addition or subtraction) of two or more atomic orbitals. A molecular orbital (MO) formed by addition of the wavefunctions is known as a bonding MO ( $\sigma$ ). By the same logic, when the atomic orbitals are out of phase, then the MO formed is known as anti-bonding ( $\sigma^*$ ).

**Frontier Molecular Orbital Theory:** This theory is also an application of the (MO) theory. This concept was put forward by Kenichi Fukui in 1952 who realized that a lot of reaction mechanisms can be explained by looking at the Highest

Occupied Molecular orbital (HOMO) and Lowest Unoccupied Molecular orbital (LUMO). It was based on three main observations of the molecular orbital theory:

- The occupied orbitals of different chemical species repel each other
- Positive charges on one molecule attract the negative charges of the other and vice versa
- The HOMO and the LUMO of different chemical species interact causing attractions.

From these observations, the FMO theory simplifies reactivity between HOMO of one species and the LUMO of the other. This helps to predict many reactions and is especially helpful understanding the charge transport in organic molecules. the difference between the HOMO and LUMO can be regarded as the band gap in organic semiconductors.

Calculating electronic energy states accurately can get complicated very quickly, even when certain terms are left out of the equation and trial wavefunctions are utilized. For this reason, another method to calculate energy states is often employed which does not rely on the use of wavefunctions. This method is referred to as Density Functional Theory and was first postulated as a method to determine energy levels and electron densities in materials by Hohenberg and Kohn

in 1964 (Hohenberg and Kohn, 1964). Density functional theory is well utilized in molecular electronics to determine energy states for determination of electron transfer rates.(Evers et al., 2004; Tomfohr and Sankey, 2004).

### *Conductance of Nanostructures in a nano-junction*

Let us take a look at how we calculate the conductance of a molecule confined in a nanogap between two electrodes.

Landauer-Buttiker Formula: Electron transport through a single molecule between two electrodes is very different from current passing through bulk materials. If the transport is assumed to be an elastic tunneling process, then the tunneling current can be described by Landauer's formula for linear conductance. This is only applicable for an electrode-molecule-electrode junction and is as follows:

$$G = \frac{2e^2}{h} \sum_{ij} |T_{ij}|^2 \quad (1.7)$$

where  $T_{ij}$  is the matrix elements that connect electron states  $i$ , one side of the junction to electronic states  $j$ , on the other side of the junction.

When the two electrodes in question are gold, then  $T_{ij} = 1$  and the conductance ( $G_0$ ) is given by  $G_0 = \frac{2e^2}{h}$ , the numerical value of which equals  $77.5 \mu S$ . This value of the Landauer conductance is one of the fundamental constants associated with electron transport. (Lindsay, 2010) This has also been proven by stretching a gold filament to its breaking point. It was found that the conductance steps occur in

exact multiples of  $(G_0)$ . (He et al., 2006) These results, obtained for a molecule in a junction can easily be extended to a molecular wire in a junction at small voltages. the Hamiltonian for the system, in that case is given by  $H = H_0 + V$  where  $H_0$  is the Hamiltonian of the uncoupled molecule and the electrodes and  $V$  represents the coupling between the molecule and electrodes. In the weak coupling limit, the operator  $T$  is

$$T = V + VG(E)V$$

where  $G(E)$  is the Green's function and is represented by

$$G(E) = \frac{1}{E - H + i\Gamma}$$

The first term represents direct electron transport from the left electrode to the right electrode, which is small if electron transport through molecule dominates the total transport current. For a linear molecule consisting of  $N$  bridge sites, we have

$$\begin{aligned} T_{ij} &= \langle i | VG(E)V | r \rangle \\ &= \langle i | V | 1 \rangle \langle 1 | G(E) | N \rangle \langle N | V | j \rangle \end{aligned}$$

Conductance (from equation 1.7) can be expressed in terms of current ( $I$ ) and

voltages ( $V$ ) by the following equation:  $I = GV = \frac{2e^2}{h} \sum_{ij} |T_{ij}|^2 V$

Writing the equation a little differently to conform to literature notations we have:



$$I = \frac{2e\pi}{\hbar} \sum_{ij} |T_{ij}|^2 \left( f(E_i) - f(E_f) \right) \delta \left( E_i - E_f + eV \right) \quad (1.8)$$

The terms  $\left( f(E_i) - f(E_f) \right)$  and  $\delta \left( E_i - E_f + eV \right)$  come from the sum of density of all states in both the electrodes. Now, we know that the molecular states can be calculated from Density Functional Theory and a Green's Function method, the electronic states of the right and left electrode can be obtained. This method shows a good agreement to experimental findings. (Tomfohr and Sankey, 2004)

It can be assumed that the HOMO-LUMO gap in molecules will dictate the conductance of the molecules. In conjugated systems, the HOMO-LUMO gap is determined by the difference between  $\pi$  and  $\pi^*$  states and for aromatic systems, the delocalization energy gives an idea of the overlap between neighboring  $\pi$  orbitals. So, the HOMO-LUMO gap in conjugated systems is much smaller than saturated chains and the conductance of conjugated chains are typically higher as well.

### *Electron transport through single molecular wires tethered in a nano-junction*

With this theoretical background of electron transport through molecules wired in a junction, let us take a look at the experimental evidence that has been found for the same over the past decade. A wire-shaped molecule that can efficiently transport charge has been actively pursued as it may provide interconnections for

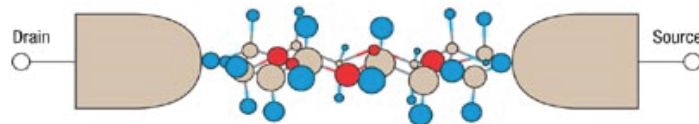


Figure 1.7: To reach the ultimate goal in device applications, experimental techniques to fabricate such an electrode-molecule-electrode junction, and theoretical methods to describe the electron transport properties must be developed. (Tao, 2006)

molecular devices. Many wire-shaped molecules have been studied, which can be divided into two major categories: saturated and conjugated chains. The way to study these molecular wires is to anchor them, with the help of terminal functional groups, in between two electrodes and study how they conduct electricity, as depicted in figure 1.7. Let us understand the electron transport on a case by case basis.

#### Saturated chains:

Alkanes with two terminal binding groups are systems that have been thoroughly investigated (Slowinski et al., 1997; Venkataraman et al., 2006; Wang et al., 2003). Their HOMO-LUMO gaps are very large and hence they are considered to be very poor conductors. However, they can be used as a model system to test experimental techniques and theoretical calculation. Experimental evidence suggests that the conductance ( $G$ ) of the alkanes decreases exponentially with increasing

number of carbon atoms in the alkane chain ( $N$ ) and follows the equation:

$$G = A \exp(-\beta_N N) \quad (1.9)$$

$A$  is a constant that is determined by the electrode molecule coupling strength and is, therefore, very much dependant on the end groups. Studies indicate that the stronger the binding strength of the of the molecule and the electrode, the higher is the value of  $A$  (Chen et al., 2006; Lee et al., 2006; Mueller, 2006). The  $\beta_N$  is a very important parameter known as the tunneling decay constant and gives an idea of the efficiency of electron transfer along a molecule. The exponential decay suggests electron tunneling as the conduction mechanism for these molecules.

Conjugated chains:

Since the conductance falls off exponentially for saturated chains, it is very difficult to get accurate values of conductance for large (longer than 2 – 3) molecules. For longer molecules, alternating single and double bonds or a conjugated  $\pi$  system is essential as the HOMO-LUMO gap for such molecules is much smaller and the charge transport, more efficient. The mode of electron transport is no longer tunneling in such systems but is replaced by a mode of transport known as hopping. In the hopping process, electrons "hop" from one site to another and this process shows a weaker dependence on the length of the molecule. Electron transport through molecules such molecules are better understood by evoking equation 1.8 as we will see in Chapter 4.

### *Charge transfer (Marcus Theory)*

Electronic energy levels in molecules alone cannot completely predict electron transfers within a molecule! In fact, inter and intra-molecular electron transfers are controlled by thermodynamics. The difference in Gibbs free energy ( $\Delta G^0$ ) is a very important factor that predicts whether an electron transfer will at all occur or not. Even when there is no free energy difference, electron transfers do not occur randomly. That is because of another very important factor called solvation energy or Re-organizational energy ( $\lambda$ ). An electron does not exist by itself in solution but has a solvation sphere around it at all times. When the electron is transferred from a donor (D) to an acceptor (A), the solvation sphere undergoes rearrangement which requires energy. This is why the thermodynamics of electron transfer is so important.

Marcus theory was originally developed by Rudolph A. Marcus in 1956 to explain the rate at which electrons hop from one species (electron donor) to another (electron acceptor). Originally formulated for outer sphere electrons, it was later modified to include inner sphere electron transfers in which the chemical species was joined by a bridge. This got Marcus the Nobel Prize in Chemistry in 1992 (Marcus, 1956). The pictorial depiction is given in figure 1.8. In the figure, the  $x$ -axis is the reaction co-ordinate and the  $y$ -axis is the free energy.  $\lambda$  is known as the

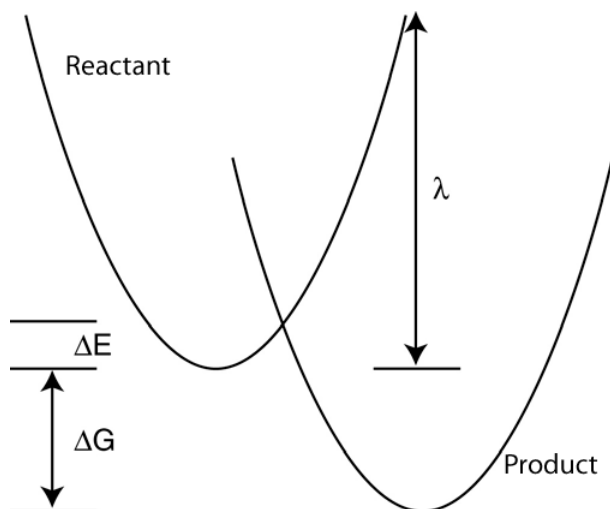


Figure 1.8: Marcus energy diagram

reorganization energy or the solvation energy. The left parabola is the potential energy of the donor-acceptor (D-A) moiety in its initial state and the right hand parabola is the final state after electron transfer. The unusual dependence of the electron transfer rate on the free energy change  $(\lambda + \Delta G^0)^2$ , which leads to the Marcus inverted region, follows from assuming that the potential energy of the initial and final states varies quadratically with the reaction co-ordinate, solving for activation energy and using it in the Arrhenius equation. So the final form of Marcus equation looks like this:

$$\kappa_{et} = 2\pi \hbar |H_{AB}|^2 \frac{1}{\sqrt{4\pi k_b T}} \exp\left(\frac{-(\lambda + \Delta G^0)^2}{4\lambda k_b T}\right). \quad (1.10)$$

where  $\kappa_{et}$  is the rate of electron transfer,  $|H_{AB}|$  is the electronic coupling between the initial and final states and  $k_b$  is the Boltzmann constant. This equation clearly

shows that even if the free energy difference between the initial and final states is zero, the rate of electron transfer is thermodynamically controlled due to the solvation energy  $\lambda$ . Marcus theory will be invoked in Chapter 2 while discussing the design of molecular photovoltaics.

### *Experimental methods utilized in molecular electronics research*

In order to put the the lofty idea of molecular electronics into practice, it is important to obtain reliable and stable measurement techniques to test molecular devices. The tests need to be done in a way that does not alter the molecules themselves (Hippis, 2001). One technique is to wire the molecule in between two electrodes and study them. Of course the big question here is, how do we wire these molecules? The simplest way to do so would be to create a small nanogap made of two electrodes and tether the molecules in the junction to create a nanocircuit. The experimental details are describes in the following paragraphs.

One method, reported by Tour et. al. in was to measure the conductance of of benzene-1,4-dithiols with the help of mechanically controlled break junctions (Parks et al., 2007; Reed et al., 1997; Strachan et al., 2005). The molecules were allowed to self-assemble on a gold wire and the wire was stretched until it broke, thereby allowing the study of conductance through these molecules (Reed et al., 1997). Another method that was found to be reliable for measuring molecular

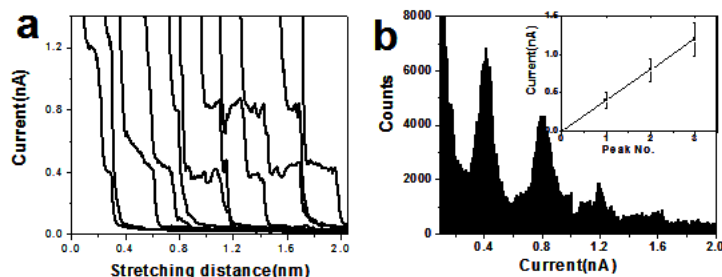


Figure 1.9: a-Current recorded by pulling shows step wise features and b-Conductance histogram constructed from individual measurements shows well defined peaks (Xu and Tao, 2003)

conductance is the STM break-junction method. Introduced by Xu and Tao (Xu and Tao, 2003), this method produces results that are reproducible and matched theoretical calculations. There are several variations of the break junction method but the central concept is to use bis-functional molecules tethered across a nanogap, made out of conductive electrodes, and then measure the conductance (Chen et al., 2005; Fujihira et al., 2006; Li et al., 2006). In the STM break junction method, bis-functional molecules are allowed to self-assemble on a conductive surface which also acts as the electrode. The STM tip functions as the second electrode. The probe is driven into the surface and retracted and the process is repeated constantly while monitoring the current decay. There is a chance of the tip "grabbing" the free end of a molecule in this process and there will be a single molecule caught in the tip-surface junction. If there is no molecule, then the current decays exponentially, according to equation 1.1. However, if there happens

to be a molecule in the junction, the current trace will show a "step" or plateau. This is because, although the voltage on the piezo is still pulling the tip away from the surface, the current remains constant as the gold filament stretches but the trapped molecule does not.

Data selection: Histograms are compiled using a subset of the curves. The number of curves selected can vary between 20-80 %. In order to retain the curve in the final data set, it was required that the slope in between the steps were in the order of a decade  $\text{\AA}$ . If the slopes are larger than this, then the curves are rejected. Curves showing only a sharp decay pattern with no steps are also rejected as they give no information about the molecule and only add to the background noise. Sometimes stray noise signals generate what appear to be steps. However, these can be easily distinguished from actual steps because they either occur at periodic intervals or show no bias dependence. When all the traces with the steps are plotted in a histogram, it produces peaks which corresponds to multiples of the conductance of a single molecule (He et al., 2006). With the invention of the SPM and its further development, the single molecule measurements started to become more of a reality. The STM break junction method, introduced by Xu and Tao has had ground-breaking results in measuring single molecule conductance. This method will be utilized extensively in chapters 3 and 4.

Another method of studying single molecules is using the STM break junction



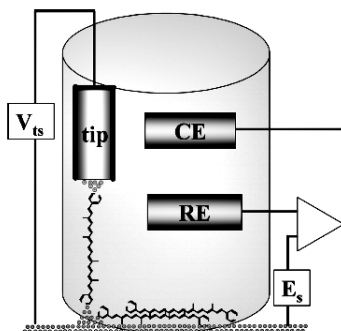


Figure 1.10: Schematic of experimental set-up of the STM break junction under potential control (Visoly-Fisher et al., 2006)

method under potential control. An electrolyte is used in this kind of study along with three electrodes, the reference, counter and the working electrodes. It can also be seen as creating an electrochemical gate. It was utilized by Visoly-Fisher et. al. to study carotenoids, which are used during electron transfer in photosynthesis. It was found that, once oxidized, the carotenoids become more conductive (Visoly-Fisher et al., 2006).

### *Anchoring group effect in single molecule measurements*

In an interesting study reported by Chen et. al. in 2006, it was proved that anchoring groups play a large role in STM break junction measurements (Chen et al., 2006). The study was conducted by using bifunctional alkanes, having  $-SH$ ,  $-NH_2$  and  $-COOH$  terminal groups. The superexchange mechanism predicts that the conductance decreases exponentially with molecular length according to equation 1.9. So, it is obvious that the conductance ( $G$ ) falls exponentially with

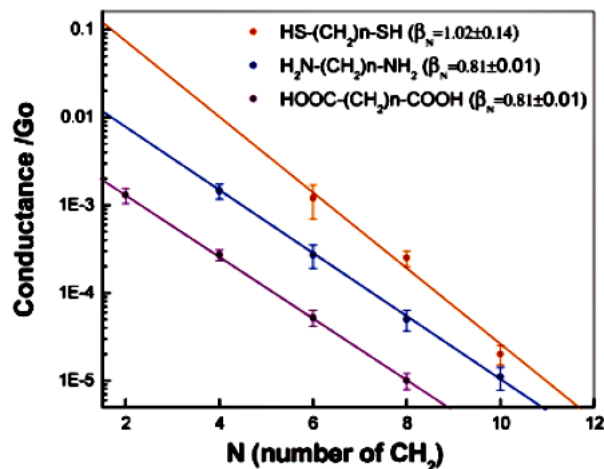


Figure 1.11: Logarithmic plot of single molecule conductance versus chain length in different molecules with. The three lines denotes the difference in decay constants for alkanes with different end groups (Chen et al., 2006)

$N$  or the number of  $-CH_2$  units in the alkane chain. This paper also indicated that  $\beta_N$  is dependant on the anchoring groups as well (see figure 1.11). However, in keeping with literature, the value does lie between 0.8 to 1.0 per  $-CH_2$  unit. These concepts will be invoked extensively in chapter 3 to verify experimental techniques.

## Chapter 2

### Organic Photovoltaics

This chapter deals with the motivation behind the entire thesis. It starts with the energy crisis and then goes into the discovery and development of organic photovoltaics.

#### 2.1 Energy crisis

Traditional sources of energy in use today are mostly derived from non-renewable fossil fuel sources (see figure 2.1). In the United States, 86% of the energy consumption is fossil fuels (US EIA 2007) and 90 % of greenhouse gas emissions come from fossil fuels (US EPA 2000). Harvesting, processing and distributing these fossil fuels release billions of metric tons of harmful gases and significant amounts

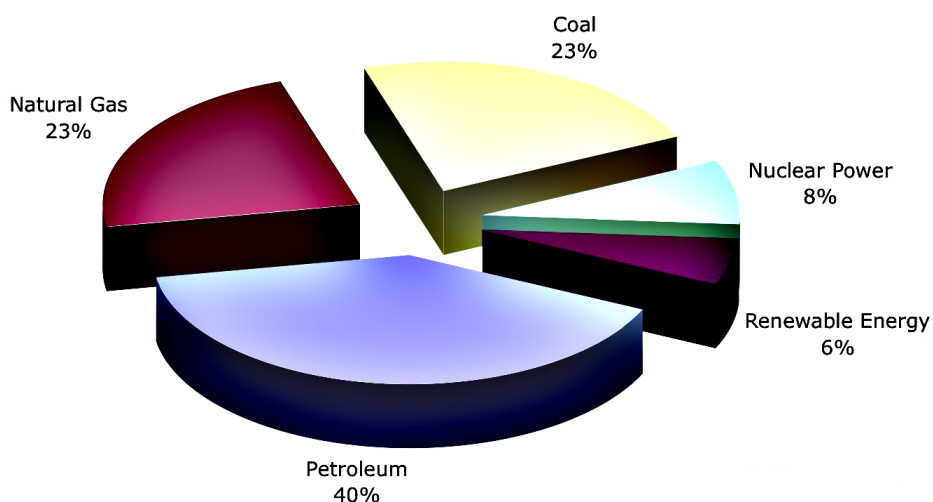


Figure 2.1: 86 % of energy consumption in the United States is fossil fuels (source: US Energy Information Agency)

of radioactive elements into the earth's atmosphere. Oil refineries and offshore drilling affects causes air and water pollution and affects aquatic ecosystems (Gore and Peters, 1993). EPA (2005) has explicitly stated that the fossil fuel emission needs to be reduced to 70 % by 2018 which is a daunting task, given the current energy demands of the society (Williams et al., 2005). Moreover, the sources of the fossil fuels are finite and perishable and has been the cause of much political and unrest and economic collapses in the world (Commoner, 1976). The short terms prices of fossil fuels fluctuate with the change in the geopolitical environment and natural disasters. In July 2008, the inflation-adjusted price of crude oil reached \$ 147.30/barrel in the United States. Many reasons were attributed to the price increase like the declining petroleum reserves, peak oil worries, political climate and other factors. The effects of the crisis were far reaching and long term. Some predict that it will bring about a recession similar to the Great Depression (McDonald and Schrattenholzer, 2001). This is the reason for the drive to obtain energy from renewable and natural resources. One of the most obvious choice is to harness solar power as it is an almost infinite source and energy obtained from the sun does not release harmful gases to pollute the planet.

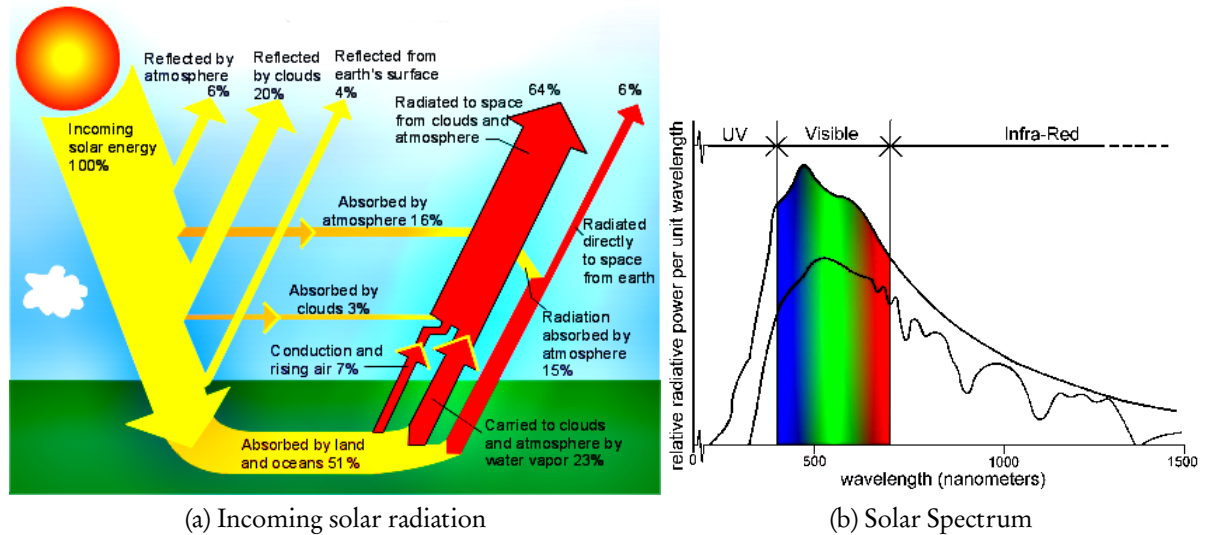


Figure 2.2: Figure (a) shows the amount of energy actually reaching the earth's surface and figure (b) is a diagram of the solar spectrum (Source: figures modified from [www.nasa.gov](http://www.nasa.gov))

### *Potential of solar energy*

The concept of utilizing energy from the sun is, by no means, new. Our ancestors have been utilizing it since ancient times as solar thermal to heat water and other such activities. Solar radiation, along with its secondary resources like wind power, hydroelectricity account for the most available renewable energy resource on the planet. Solar energy is also lauded an almost infinite energy resource that is clean, pollution free and very often noise free. The amount of solar radiation hitting the earth's outer atmosphere is 174 petawatts (Bird and Riordan, 1984; Vitousek et al., 1997). Not all of it absorbed as a lot of it gets reflected back to outer space (see figure 2.2a) and some gets converted to heat energy. In spite of the variations, the amount of energy reaching the earth from the sun every hour is enough

to meet the annual energy demand of the planet. Lets verify this statement with some simple calculations (numbers have been rounded off for simplicity in calculations):

Amount of solar energy reaching the earth annually =  $4 \times 10^{18}$  Joules

$4 \times 10^{18}$  Joules/year  $\div$  365 days/year =  $1 \times 10^{16}$  Joules/day

$1 \times 10^{16}$  Joules/day  $\div$  24 hours/day =  $4 \times 10^{14}$  Joules/hour

Amount of energy consumed annually by the entire population on the planet

=  $3 \times 10^{14}$  Joules

The spectrum of solar radiation coming to earth's surface is spread mostly across the visible region (see figure 2.2b) with parts in the near-infrared and near-ultraviolet regions. This will be an important factor when we talk about designing organic photovoltaics. The solar constant is the amount of incoming solar radiation per unit area (on a plane perpendicular to the rays) and is measured by satellites to be around 1,366 kilowatts per square meter. (Zahran et al., 2008)

## 2.2 Energy conversion in photovoltaics

Photovoltaic technology is based on the conversion of light to electricity. Certain materials exhibit the photoelectric effect, which essentially means that they can absorb light photons and release electrons. These free electrons can be channeled to produce electric current, thereby producing electricity. The photovoltaic ef-

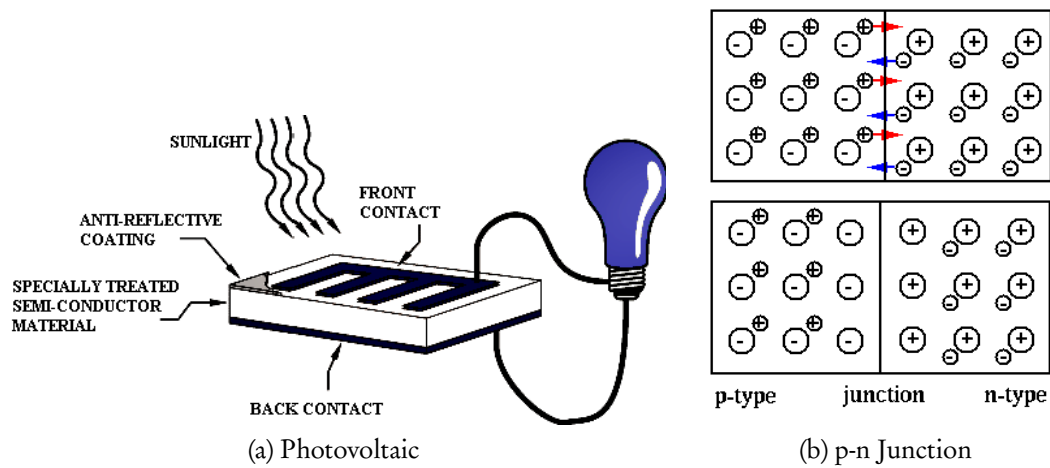


Figure 2.3: Figure (a) is a schematic depiction of a typical photovoltaic device ((Zahran et al., 2008))and (b) is a junction between a p-type and a n-type semiconductor

fect was first observed by Edmund Becquerel in 1839. In 1905, Albert Einstein explained the photoelectric effect and the nature of light which ultimately won him the Nobel Prize in physics. The first solar cell was patented by Russell Ohl in 1946. In spite of extensive research in the semiconductor photovoltaic area, commercial solar panels suffer from low efficiency and high costs which make them inaccessible to a lot of the population. Traditional photovoltaics are made of inorganic semiconductors (like silicon). Silicon is largely used as the band gap matches the solar spectrum. The function of a photovoltaic is to absorb photons from sunlight and convert it into electricity. Therefore, there are two main processes occurring in any given photovoltaic device (Green, 1993).

- Absorbtion of photons in the solar radiation to produce electron-hole pairs (excitons).

- Transportation of the charge carriers to the respective electrodes to produce electric current.

Both the process of absorption and transport are critical to a solar cell's potential as a viable energy conversion device. If the cell does not efficiently absorb at high intensity solar wavelengths, then the cell has little utility. Furthermore, if those excited electrons and holes are not able to be transported, they eventually recombine and the absorbed energy is lost. Balancing good absorption with good transport is a critical challenge in photovoltaic design (Green, 2002).

Typically, a silicon wafer is diffused with a n-type dopant at one end and a p-type dopant at the other end to produce a p-n junction (see figure 2.3b) However, for simplification, it can be thought of as a layer of p-type silicon in contact with a n-type silicon layer. As a result of this contact, electrons will travel from the n-type side of the junction to the p-type side and create a volume that is charged at the interface of the junction and is referred to as the depletion region. This depletion region produces an in-built electric field which acts as a diode. There are two main processes occurring in a typical photovoltaic device. Now, when a light photon hits the silicon wafer there are three possibilities:

- Low energy photons can pass right through.
- Photons can get reflected off the surface of the device.



- Photons having energies equal to or higher than the bandgap (of silicon in this case) get absorbed and produce an electron-hole pair and may generate some amount of heat.

Once the electron gets excited into the conduction band of the semiconductor, there are two possibilities: the electron may drop back to the ground state and recombine or it may be extracted to produce an electric current. Electrodes are connected to both ends of the semiconductor. For a silicon semiconductor solar cell, the back contact electrode is typically aluminium (see figure 2.3a) and the top electrode is a transparent conducting oxide (TCO which will be discussed in more detail later in the chapter). When the electrodes are shorted together the extra electrons at the n-side flow into the electrode and go over to the p-type side and recombine with the holes. This defines the short circuit current. If the device is operating on an open circuit charge builds up on the device to produce an open circuit voltage. Obviously, charge carrier recombination does not produce any useful work and a lot of research is directed at preventing this process, thereby trying increase the efficiency of solar cells.

#### *Drawbacks of semiconductor photovoltaics*

Semiconductor photovoltaic cells are currently on the commercial market, available to both residential and industrial consumers. Many power companies even allow photovoltaics to be tied to the existing grid and buy any excess electricity

that the consumer does not utilize. Although semiconductor photovoltaics are making headway in becoming larger-scale energy production sources, the drawbacks of their use currently stops many consumers from purchasing. The efficiency of a cell depends upon the quality and processing of the semiconductor, which is often proportional to the cost of the cell. This expense, compared to the low upfront cost of more conventional energy sources, can make consumers reluctant to purchase photovoltaics. The commercial photovoltaics available for installation on rooftops are mainly made of single crystal or polycrystalline silicon and in some cases cadmium sulfide thin films. The cost of manufacture of such solar panels is very high. The solar cells available to the average consumer produce energy at a cost that is much higher than fossil fuel sources. For example, the United States Department of Energy recently published that the levelised cost of energy for rooftop photovoltaics in 2008 was between 0.20 cents and 0.80 cents per kWh. (Fthenakis et al., 2009) This is quite expensive compared to the average retail price of electricity in 2008, which was 0.11 cents for residential consumers. (Fthenakis et al., 2009) For this reason, research in organic molecules as photovoltaic materials has grown over the past few years. Organic solar cells are based on mimicking photosynthesis and the light conversion mechanism utilized by plants everyday to convert photons into some other form of energy. Although efficiency has remained an issue in organic photovoltaic research, the prospect of

a less costly device has continued to spur more investigation in the field.

### 2.3 Benefits of Organic Photovoltaics

Many diverse approaches are being followed in order to bring down the cost and improve efficiency of organic photovoltaics. Using organic molecules or dyes to absorb photons is a very simple method to cut some of the costs involved in the manufacture of solar cells. The basic architecture of an organic photovoltaic consists of an organic molecule or dye layer sandwiched between a transparent conductive oxide (TCO) and a metal electrode. The photons from sunlight enter the solar cell through the TCO and produce electron-hole pairs (or excitons) once they get absorbed by the organic layer. The excitons migrate to the electrodes to produce photovoltage or photocurrent. The most important factor in favor of using organic materials in solar cells is the reduction in cost of the device. As discussed earlier, semiconductor solar cells are extremely expensive to manufacture and this cost of production deters most people from taking advantage of solar energy. Organic molecules, on the other hand, can be spin coated or self-assembled onto electrodes to produce low cost solar cells. This factor might make organic photovoltaics good competitors for semiconductor solar cells, even at lower efficiencies. Since much organic photovoltaic (OPV) research involves the processing of organics in low cost ways, this is clearly a goal for the OPV field. There are other benefits as well to OPV research. Organic molecules are versatile mate-

rials, and thus can be changed and modified to suit different needs. Chemical variations in molecules change how they absorb light and this can be utilized to tune the absorption of the photovoltaic to the solar spectra (see figure 2.2b) in order to more efficiently capture available radiation (Currie et al., 2008). Bulk material flexibility is also seen as a potential benefit of OPVs. This leads to the idea that organic films can be made on flexible substrates, which may eventually lead to flexible photovoltaics. (Brabec, 2004) Since traditional semiconductor photovoltaics are typically rather rigid, they are limited in where they can be placed and how they can be transported. A flexible photovoltaic has many commercial applications and is a key potential benefit to organic solar cells. (Pagliaro et al., 2008)

## 2.4 Challenges to Organic Photovoltaics

Although the benefits of organic photovoltaics certainly make them promising candidates for commercial solar cells, there are certain challenges that have and continue to keep them from large scale commercial markets. Most challenges in the design and fabrication of these photovoltaics is centered around the low efficiencies of such devices. Figure 2.4 shows the efficiencies of different types of research solar cells versus the year that the efficiency was determined. Clearly, the graph shows that organic photovoltaics are among the lowest efficiency de-

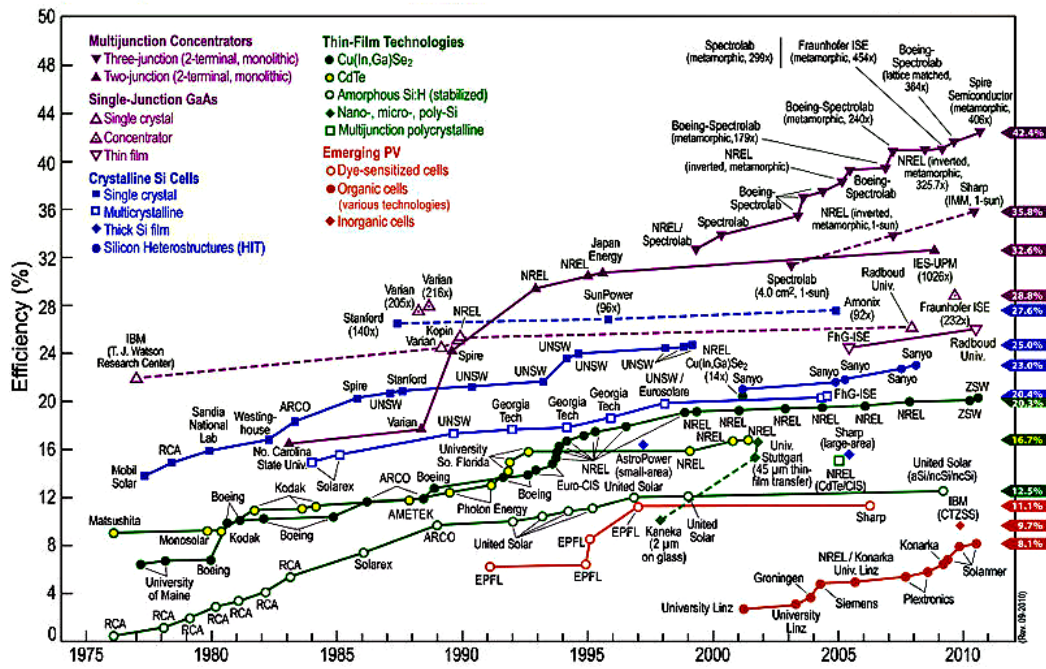


Figure 2.4: Best research cell efficiencies by type of solar cell and year (Source:www.nrel.gov)

vices.

The reason for the traditionally low efficiencies in organic photovoltaics are explained here. Every photon that gets absorbed by the film leaves an electron in a higher energy excited state and a hole. In order to produce photocurrent or photovoltage, this electron and hole pair need to travel to their respective electrodes, which are determined by the electronic work functions. The efficiency of the device can be determined by the rates of carrier transport minus the recombination rate.

Unfortunately, in most organic devices the rate of absorption is small (organic molecules typically have absorption cross sections on the order of  $\text{Angstrom}^2$

), while the rate of recombination is relatively high. Combined with low mobilities (as low as  $10^{-4} \text{ cm}^2 \div [V \times s]$  for electron and hole mobilities for some polymer-fullerene blends discussed later in the chapter) which limit the rate of particle capture by the electrodes, and the efficiencies of these devices turn out to be low. Exacerbating the problem is the fact that most changes that can improve one part of the efficiency equation tend to negatively affect the other parts. For example, increasing the thickness of the organic layer does increase the amount of light being absorbed, but a fewer percentage of the excitons generated get to the electrodes. This is because excitons must diffuse to the electrodes. The diffusion length before recombination of excitons in typical organic film is on the order of 5-20 nm. So, a film that is any thicker than 20 nm does not collect all the generated excitons due to charge recombination. (Halls et al., 1996; Haugeneder et al., 1999) Decreasing the thickness of the film increases how many excitons make it to the electrodes, but obviously decreases the amount of light absorbed. So beneficially changing this rate equation in significant ways requires more sophisticated methods.

## 2.5 Organic Photovoltaic Architecture

As previously mentioned, organic photovoltaics suffer from low efficiencies that are a result of competing factors in the rate equation that determines efficiency.

There have been numerous methods to increase the efficiency that go beyond simply changing the thickness of the organic layers, which, as mentioned, can only affect efficiencies by a very limited amount. For this reason, several more sophisticated methods of producing more efficient organic photovoltaics have been utilized with some success, although efficiencies, and practicality in some cases, have meant that these breakthroughs have not been incorporated into commercial solar cells to date.

### *The Grätzel Electrochemical Cell*

A major breakthrough in organic photovoltaics came about in 1991 with the Grätzel cell created by by O'SRegan and Grätzel. A schematic of a typical Grätzel cell is shown in figure 2.5. The uniqueness in the Grätzel cell came from the utilization of nanoporous  $TiO_2$  on top of sheets of conducting glass. The  $TiO_2$  was then exposed to a trimeric Ruthenium dye (S) which adsorbed onto the surface. The nanoporous nature of the  $TiO_2$  increased the surface area by a huge amount and the resulting  $TiO_2$  was able to absorb up to 46 % of incident solar light. The dye-sensitized  $TiO_2$  was then put into contact with an electrolyte solution such as  $I_2/(I_3)^-$  which was in contact with another transparent electrode, like ITO. In this solar cell configuration, when the dye absorbs light, it injects the excited electrons into the  $TiO_2$ , leaving the dye positively charged. The electrolyte can then

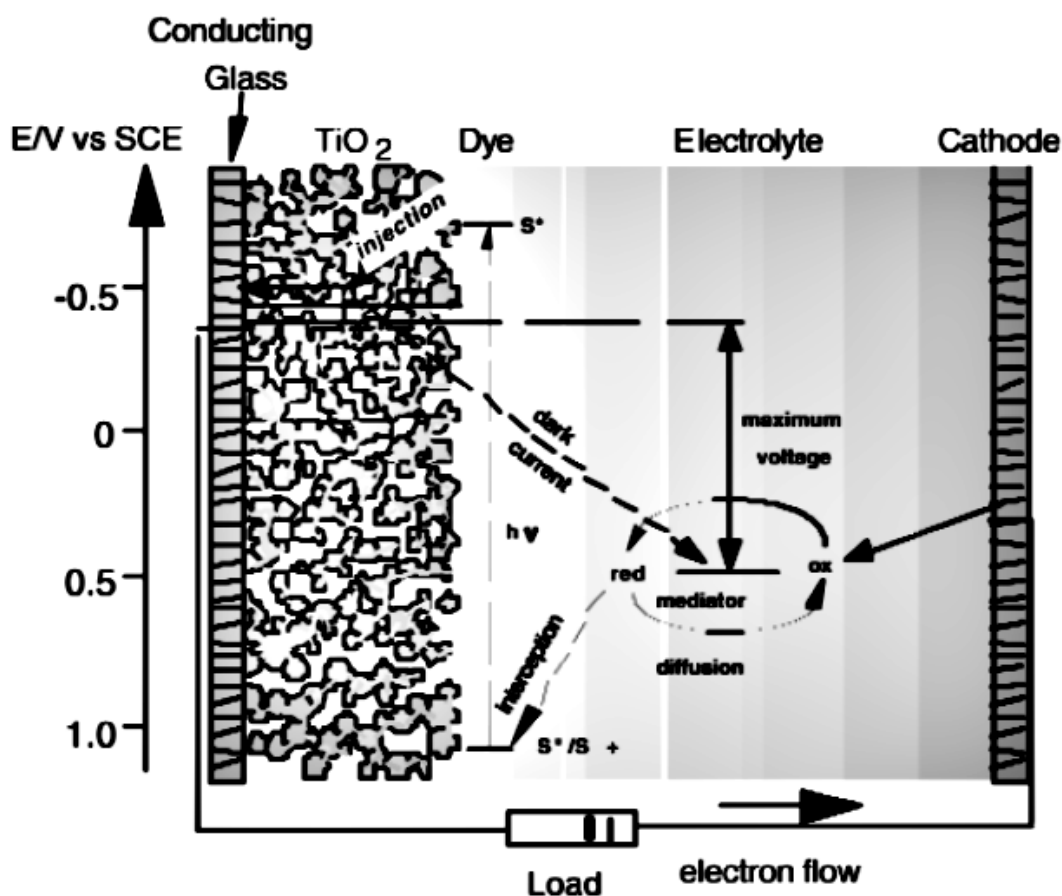
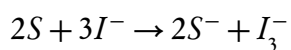


Figure 2.5: Diagram of the Grätzel cell (O'Regan and Gratzel, 1991)

quickly donate an electron to the dye leaving it neutral, and leaving the electron permanently injected into the  $TiO_2$ . The equation for the process is as follows:



The efficient interception of recombination by the electron donor ( $I_3^-$ ) is crucial for obtaining good collection yields and a high cycle life of the dye. (?) The ITO then donates an electron to the electrolyte ion in the solution. By connecting the  $TiO_2$  through a load to the ITO in contact with the electrolyte, the circuit can be



completed and power generated. This solar cell scheme gets around some of the typical problems with many OPV devices. There is no need, for instance, for the exciton to diffuse within the organic, since the electron can immediately inject into the  $TiO_2$  and the hole can be filled by the dye being in constant contact with the liquid electrolyte. Rates of electron and hole transfer increase without changing the amount of absorbed light. In addition, the nanoporous  $TiO_2$  provides a very high surface area electrode, allowing for more organic dye to absorb onto the surface. This, then, increases the absorption of the device, without creating a thick, non-conducting organic film. Originally these cells had efficiencies from 7.1 % -7.9 %, which is much higher than other organic photovoltaic devices. Current research in Gratzel-type cells has led to photovoltaics achieving up to 10.6 % efficiency (Gratzel, 2004). Grätzel cells, unfortunately, do suffer from difficulties in practical application. They currently require a liquid electrolyte in order to operate. This necessity has made it impractical to use in any significant way as a photovoltaic device. The other problem with the Grätzel cell is that the efficiency is still not high enough to compete with the traditional semiconductor solar cells.

#### *Transparent conducting oxides*

The light absorbers in photovoltaic devices need to be sandwiched in between two electrodes. However, if both the electrodes were made of metals, then very little sunlight would actually reach the molecules. Hence, these devices require

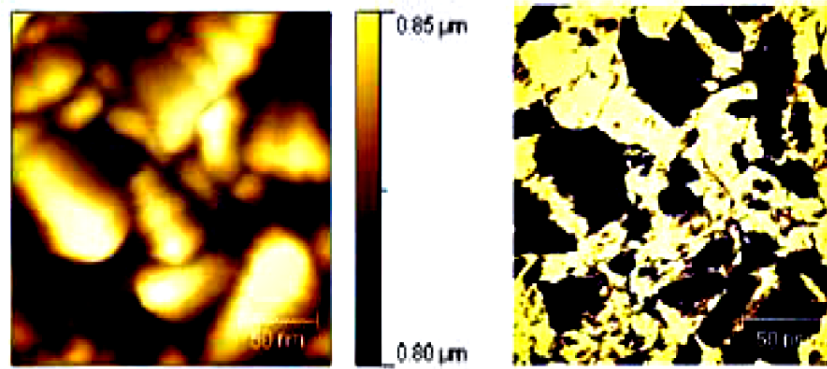


Figure 2.6: Conductive AFM image of fluorinated tin oxide. Left shows the surface topography and right shows the conductance map. (Source: AFM image from Ashley Kibel)

something that is almost as conductive as a metal yet is transparent to visible light like  $\text{SiO}_2$  glass. This is where the transparent conductive oxides (TCOs) come in. They are doped metal that have 80 % or more transmittance in the visible region. Therefore they allow the photons to reach the active layer of the photovoltaic devices. However, they provide an Ohmic contact for the transportation of the charge carriers generated in the device. Mostly these are thin films having polycrystalline or amorphous microstructures and are coated onto glass. The TCO used most extensively is Indium Tin Oxide (ITO) which is essentially a solid solution of Indium (III) oxide ( $\text{In}_2\text{O}_3$ ) and Tin (IV) oxide ( $\text{SnO}_2$ ). Other TCOs popularly used are Fluorinated tin oxide (FTO) and Aluminium doped zinc oxide. The way ITO is fabricated in by sputter coating onto glass. For large scale manufacturing, these TCO work extremely well. However, for nanoscale applications, the surface was found to be extremely inhomogeneous, both structurally

and electronically. Figure 2.6 shows the structure of FTO and the conductance map shows patches where the FTO does not conduct at all. This became an issue for single molecule nanoscale measurements. The ITO surface was comparatively less inhomogeneous than the FTO. Another advantage ITO has is that, it has -OH groups on its surface which can form hydrogen bonds or covalent bonds with other carboxylic acid groups of organic molecules. (Armstrong et al., 2003; Gardner et al., 1995) This fact is utilized to create organic monolayers on the ITO. (Yan et al., 2000) However, the affinity for the attachment depends considerably on how the ITO is cleaned and prepared. These issues will be discussed in greater detail in chapter 3. (Milliron et al., 2000; Osada et al., 1998; Sugiyama et al., 2000; Wu et al., 1997)

## 2.6 Mimicking Photosynthesis: Porphyrin based Molecular Dyads

Natural photosynthetic reaction centers serve as inspiration for construction of solar energy conversion devices that generate long-lived charge separated states by photoinduced electron transfer on illumination. One very interesting way (and one that will be explored in much further detail in the subsequent chapters) to approach the problem of charge recombination is to put the donor-acceptor species on the same molecule to increase the lifetime of charge separated states. The Gust-Moore group at Arizona State University has been exploring this concept for over

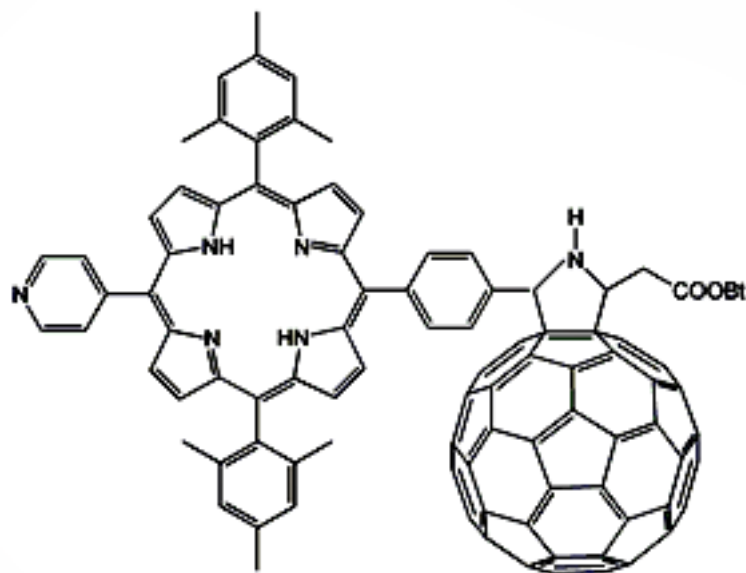
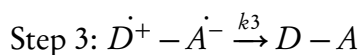
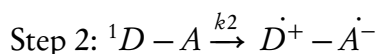
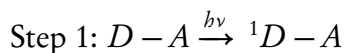


Figure 2.7: Molecular dyad synthesized by the Gust Moore group at Arizona State University. The electron donor (porphyrin) is placed in close proximity with the acceptor (fullerene) to facilitate electron transfer. (Source: Synthesised by Paul Liddell at ASU, figure by Shreya Bhattacharyya)

two decades (Gust and Moore, 1989; Gust et al., 1998). Let us look at the design of artificial reaction centers with the help of Marcus' theory of electron transfer which was described in Chapter 1. The simplest reaction center will consist of an excited singlet state electron donor (D), and a covalently attached acceptor (A). Illumination of this donor (D) with the appropriate wavelength of light will lead to the following sequence of reactions:



The excited singlet state of the donor transfers an electron to the acceptor in step

2 to give a charge separated state, which returns to the ground state by charge recombination in step 3. Recall, equation 1.10 which gives us the rate of charge transfer. In order to construct a successful reaction center,  $k_2$  has to be rapid, to overcome other pathways of decay of the excited state. The magnitude of the exponential term depends on  $(\Delta G^0)$  and  $\lambda$  and to maximize the rate, the  $(\Delta G^0)$  should be close to 0. The other term which influenced the rate of charge transfer was the matrix term  $H_{AB}$  which depends on the coupling between the initial and final states. Therefore, the donor and acceptor must be spatially close to each other for efficient electron transfer. A covalently linked porphyrin satisfied the all the criteria required to create an artificial reaction center.

Why were porphyrins the molecule of choice? The strongest absorption band for porphyrins (around 416 nm) is known as the Soret band, and the other bands between 500 and 800 nm are referred to as Q-bands. Porphyrins are utilized within chlorophyll molecules as light absorbers in photosynthesis. Since porphyrins are utilized as light absorbers in photosynthesis, it is natural to believe that they could be used to absorb light in an organic photovoltaic. In order to reduce the rate of recombination, Gust-Moore group at Arizona State University has researched ways to covalently attach electron and hole acceptors to porphyrins (Liddell et al., 1994) in order to increase the lifetime of the charge separated state, hoping to extract the charges more efficiently.

A common electron acceptor utilized in these molecules is fullerene. When attached to a porphyrin (see figure 2.7) the assembly can be referred to as a porphyrin-fullerene Dyad. Due to the energy levels of the porphyrin and fullerene (the excited electron in porphyrin is at 1.90 eV compared to the lower 1.74 eV excited singlet state of the fullerene) the porphyrin, upon absorbing light, readily donates its excited electron to the fullerene (Gust et al., 2000). When the porphyrin is able to transfer the electron to the fullerene, the excited state lifetime of the free base porphyrin-fullerene dyad extends from 20 ps to 290 ps (Kuciauskas et al., 1996).

## Chapter 3

### Molecular conductance measurement on novel substrate

This chapter talks about break-junctions measurements using ITO and gold as electrodes. Since the measurements were the first of its kind, it was essential to verify the suitability of the ITO surface for measurements with known molecules and then study the conductance of the dyads.

#### 3.1 The ITO Surface

Recall, from Chapter 2, that in order to build a successful photovoltaic device, one of the electrodes has to be made of a transparent conductive oxide. The TCO used was ITO as it is extensively used in photovoltaic applications. However, as seen in figure 3.1 the ITO presents a poorly defined surface that is highly rough

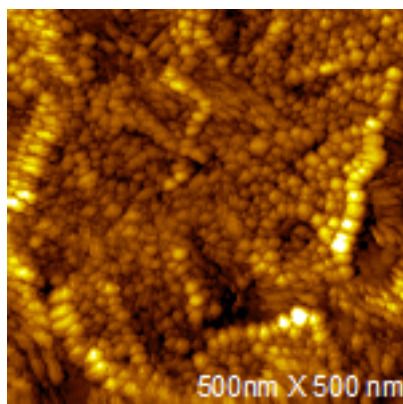


Figure 3.1: STM image of indium tin oxide cleaned with UV-ozone plasma. The surface roughness ranges from 1-3 nm. Image was taken with a gold tip. Tip bias = -0.4 Volts. Current set point = 0.1 nA.

and not well-characterized in terms of nanoscale conductance. The figure shows a typical surface cleaned with oxygen plasma and imaged with a gold STM tip. The regions that appear dark are lower and the the regions that appear dark are higher as seen by the STM tip. The surface is therefore very uneven, the roughness varying from  $1 - 3nm$ . Conductive AFM measurements performed on the ITO show that the current is not uniform on the nanoscale and also varies depending on the cleaning methods and the source of ITO. However, this problem is worse for other transparent conducting oxides tested (like fluorinated tin oxide) and hence we decided to use ITO for all our experiments. As stated earlier, most break-junction measurements have been conducted using a gold surface and gold electrodes. Gold is considered the ideal surface because of the flat terraces and its ability to easily form SAMs. This is where the ITO posed as a major hurdle. The surface did not show any flat regions and hence it was difficult to position the STM tip safely on the surface. Also, there has only been one report of break junction measurements on the ITO and that too with the conductive AFM and an ITO coated AFM tip. (Chen et al., 2007) Hence our STM break junction measurements on the ITO were both challenging and unique in nature.



### 3.2 Verification of Suitability of ITO Surface for Break-junction Measurements

As mentioned before, STM break junctions on ITO was a novel concept and hence the most important step was to verify the reliability of the surface.

#### *Formation of alkane monolayers on ITO*

Previous reports have indicated affinity of ITO surface for carboxylic acid groups. (Armstrong et al., 2003; Gardner et al., 1995; Yan et al., 2000) The nature of the bond between carboxylic acid terminated molecules and ITO surface is not fully understood. One school of thought is that hydrogen bonding occurs between the hydroxyl groups on the ITO surface and the -OH of the carboxylic acid. (Berlin et al., 1998; Zotti et al., 1998). There is also scientific evidence in favor of a covalent ester bond formation between the -OH and the -COOH with the elimination of a water molecule. (Wang et al., 2001) Whatever be the nature of the bond, there is enough experimental evidence of carboxylic acid groups attaching pretty firmly to the ITO. Hence the alkane of our choice was terminated with a carboxylic acid at one end. The other end of the alkanes had to attach to the gold STM tip and so we chose a thiol because of its affinity for gold. The mercapto carboxylic acid alkanes (obtained from Sigma Aldrich) had varying lengths of the alkane chain (2,5 and 7  $-CH_2$  units). They will be referred to as C-3, C-6 and

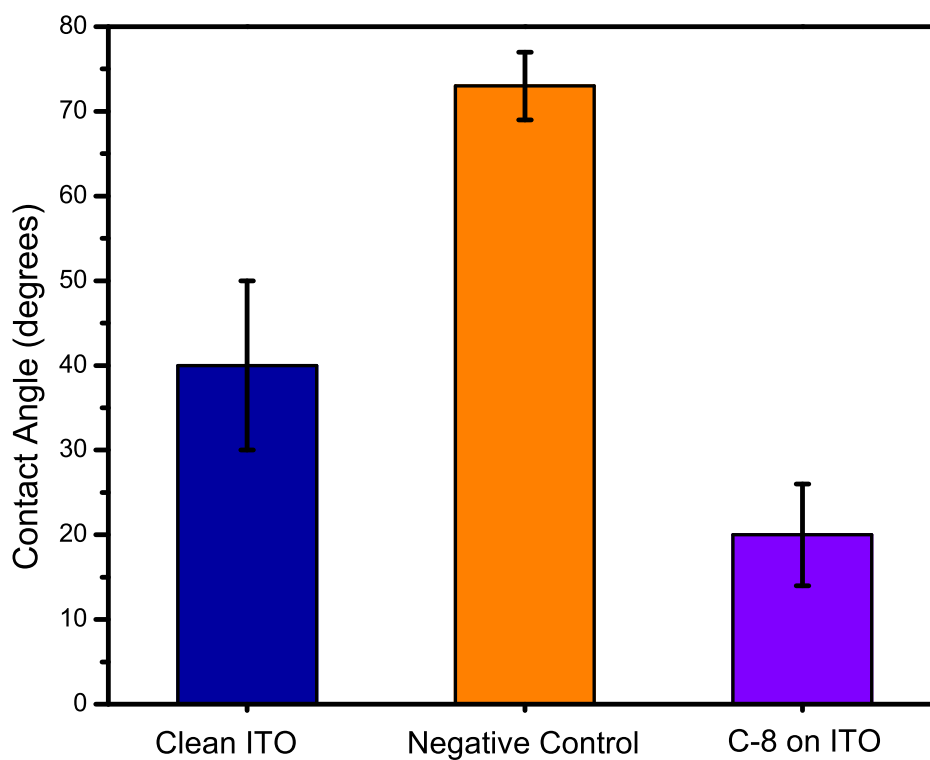


Figure 3.2: Contact angle data for oxygen plasma cleaned ITO (left). Central bar shows 7 chain alkane with a carboxylic acid attachment but without the mercapto group, which was used as a negative control. The contact angle is high due to the hydrophobic alkane tails on the surface. C-8 molecule (mercapto carboxylic acid with 7  $-CH_2$  groups) deposited on ITO (right) presents a hydrophilic surface due to the  $-SH$  groups on the surface. The standard deviation has been reported as error. Data provides evidence of a molecular layer on the ITO surface with the  $-SH$  groups free to attach to the gold STM probe.

C-8 respectively for the sake of convenience. The ITO was cleaned by sonicating in deionized water ( $18.2M\Omega$ ), ethanol and acetone for 5 minutes each and drying in nitrogen. The alkane solution was prepared by weighing a known amount of the powdered alkane into 5 ml of ethanol to make a 5mM solution. The ITO was then immersed into the solution and left for 12-24 hours. (Chen et al., 2007) After deposition, the ITO slide was washed with copious amounts of ethanol to remove the weakly bound species and dried in nitrogen. Perhaps due to the nature of ITO surface, the Fourier Transform Infra-Red spectroscopy measurements did not provide any conclusive evidence but contact angle data showed the presence of molecules on the ITO surface. In the figure 3.2 the first bar is data from a clean ITO slide with no molecules on it. The third bar (right) is data from the SAM slide after the C-8 molecules have been deposited on them. The contact angle decreases considerably due to the polarity of the exposed  $-SH$  group at the end of the alkane chain. The negative control experiment was done with hexanoic acid, which has 7 ( $-CH_2$ ) units and a carboxylic acid at one end similar to C-8 but no thiol group at one end. Therefore, after attachment to the ITO surface, only the hydrophobic alkane chains are exposed. This would cause the contact angle to increase by a great amount as the surface would now be hydrophobic and this was actually reflected in the data obtained (middle bar). This evidence points in the direction of molecules deposited on the surface of ITO. The conductance his-

tograms that will be described in the next section also provide conclusive evidence of the molecules on the surface.

*Measuring the electronic decay constant for alkanes on the ITO surface*

From chapters 1 and 2, we know that electron conductance in alkanes is described by the equation:  $G = A \exp(-\beta_N N)$ .  $N$  was varied systematically in the experiments and conductance histograms can give us  $G$ . If the  $\ln G$  is plotted versus  $N$ , the results should be a straight line, the slope of which should equal the decay constant (or  $\beta$ ). The intersection of that straight line with the x-axis should give the value of  $A$ . These values, when compared to the values reported in literature give a very good insight about the ITO surface.

Break-junction measurements were performed on the alkanes of three different chain lengths (C-3, C-6 and C-8) after preparing the SAMs as explained in the previous section. The solvent used was mesitylene (obtained from Sigma Aldrich) which had been previously sparged with argon for ten minutes. This particular solvent was chosen as its boiling point is high and so it would not evaporate during the course of the measurements (which lasted for more than 6 hours). Also, it is a non-conductive solvent. It is possible to perform measurements with a conductive solvent but the STM tip has to be coated with polyethylene or wax in a manner so as to leave a single atom exposed on the end. However, to simplify the measurements, the solvent was chosen to be non-conductive to begin with.

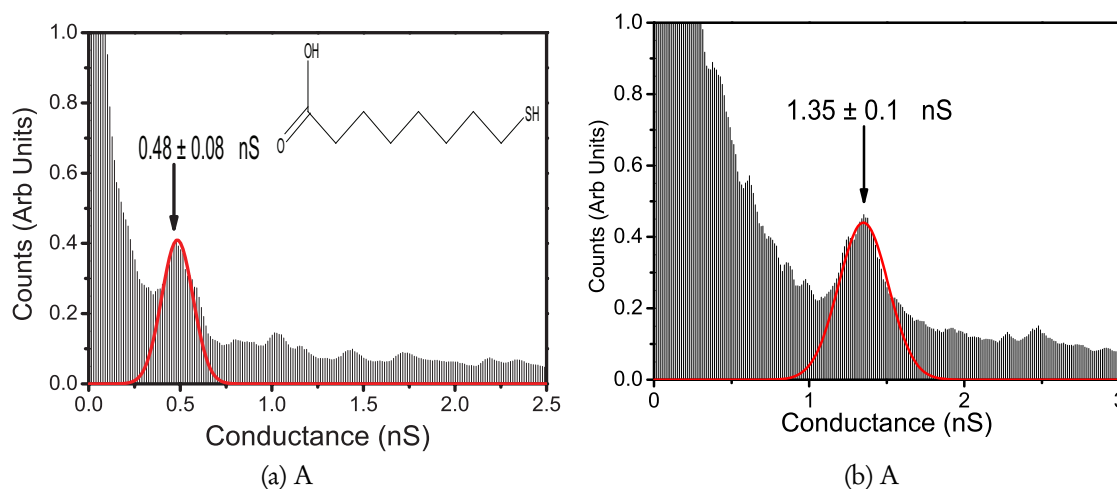


Figure 3.3: Conductance distribution histogram (solid line is a Gaussian fit) of C-8 molecule on ITO (left). Conductance distribution histogram (solid line is a Gaussian fit) of C-6 molecule on ITO (right). Measurements were conducted using oxygen-free mesitylene as solvent. Both current distributions were converted to conductance using the probe bias of -0.4 V.

The entire microscope was situated on an environmental chamber and argon was allowed to flow through it to ensure an oxygen free environment. The gas flow was stopped during break junction measurements to ensure a stable environment. Measurements were performed at three different sample voltages (200 mV, 300 mV, 400 mV) on each of the alkanes and repeated at least three times at each voltage to ensure reproducibility of the data. The experiments were controlled by a Labview program and a National Instruments data acquisition device (NI USB-6221). Picoscan software was first utilized to approach the tip to the surface at a current set-point of 0.1 nanoAmperes under a tip bias of -0.4 Volts. The surface was scanned to form an image which is essential to determine the quality of the tip

and the surface. The Picoscan servo was turned off and the labview program took control of the tip through an external z-position input on the STM controller. The tip was held at a user-determined set-point value above the sample for a short period of time using a software PID controller which read the current through the data acquisition device. (Note: PID stands for Proportional, Integral, Derivative. The PID loop is designed to eliminate the need of continuous user control. It involves automatically adjusting a variable to hold the measurement at a set-point where the measurement is supposed to be. Choosing the proper values for P, I and D is called PID tuning and is done manually with the Labview software.) The PID control was broken after a set time and the tip was retracted at a rate of  $20 - 40\text{ nm/s}$  and then re-approached to the surface where it was held under PID control again. This process was repeated multiple times at several different places on the surface. Data was recorded on a Tektronix TDS 2004B oscilloscope which recorded current, piezo voltage and bias. Once a set of data for was recorded on the oscilloscope it was immediately transferred via USB cable to a computer where it was added to an open file through another labview program. The entire process to withdraw the tip and record the data took approximately 10 seconds, so a typical experiment of about 6 hours could collect as many as 2000 curves. A labview program was created in order to analyze the break junction data. Chapter 1 explained that when a molecule is trapped in the tip-surface gap during withdraw,

a step/plateau is observed in the current versus distance retraction curve. When the current curves that have steps in them are compiled into a conductance histogram, peaks appear that represent the molecular conductivity of the molecules being studied. The number of curves collected during each run was around 2000 and around 15 percent (300 curves) were utilized to create the histogram. How do we select the final subset of curves? Recall, from Chapter 1, that in order to retain the curve in the final data set, it was required that the slope in between the steps were in the order of a decade  $\text{\AA}$ . If the slopes are larger than this, then the curves are rejected. Curves showing only a sharp decay pattern with no steps are also rejected as they give no information about the molecule and only add to the background noise. Sometimes stray noise signals generate what appear to be steps. However, these can be easily distinguished from actual steps because they either occur at periodic intervals or show no bias dependence. When all the traces with the steps are plotted in a histogram, it produces peaks which corresponds to multiples of the conductance of a single molecule (He et al., 2006). One important point to keep in mind here is that, the aforementioned data analysis was used for alkanes only. For the Dyads, we will be using a slight modification of this data analysis method which will be discussed later in this chapter.

Two of the histograms obtained are shown in the figure 3.3. A Gaussian distribution function is fitted on the first peak and the mean of the distribution is the

conductance of the molecule. It is worthwhile to note here that the conductance peak of the histograms are broader than those obtained for a gold-thiol break-junction measurement. This is because the ITO-carboxylic acid bond has more possible geometries of attachment and is more complex in nature than a simple gold-thiol covalent bond. This leads to a wider distribution in the conductance values. In fact, the second conductance peak is not even clearly visible in the histograms obtained.

In order to obtain the  $\beta$  and  $A$  values, the natural log of conductance was plotted versus  $N$ . It is important to mention here that although the number of carbon atoms in the alkane chain was 2, 5 or 7, the value of  $N$  used for the calculations were (3+1), (5+1) and (7+1). This is because the ITO and the carboxylic acid group attach with the help of the hydroxyl (-OH) group and the electron has to tunnel through the carbon in the carboxylic acid (-COOH) group. The  $\beta_N$  values reported extensively in literature is 1.0 – 0.8 per  $-CH_2$  unit for an Au-dithiol junction. (Xu and Tao, 2003) The value obtained here (as illustrated in figure 3.4), using linear fit parameters are 0.88 (per  $-CH_2$ ). Therefore the decay constant is in very good agreement with the literature values. The  $A$ -value reported in literature for Au-thiol molecule-electrode junction is 477 nS (Chen et al., 2006; Xu and Tao, 2003) and that for ITO-carboxylic acid junction is 424 nS. (Chen et al., 2007) The slight difference in the  $A$  values can be attributed to the difference in the nature



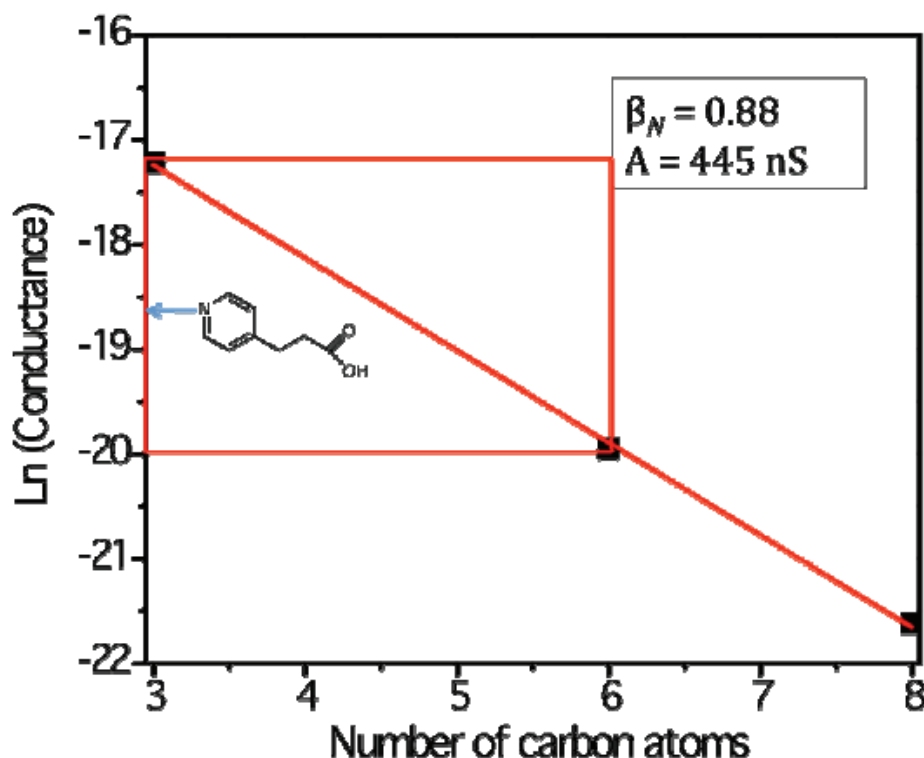


Figure 3.4: Black squares are the natural logarithm of conductance versus number of carbon atoms in the mercapto-terminated series, mercapto-propionic acid (C-3), mercapto-hexanoic acid (C-6) and mercapto-octanoic acid (C-8). Error bars do not show on this log scale. Red line is the linear fit of the data points. The values of  $\beta$  and  $A$  are obtained from the slope and the intercept of the linear fit on the y-axis respectively. (Battacharyya et al., 2011)

of the molecule-electrode contact. The value of  $A$  depends on the actual contact geometry and while the Au-thiol contact is relatively simple, the ITO-COOH contact geometry is much more complicated. The orbital overlap in the Au-thiol bond is well matched and the bond is a well-defined covalent bond. The same cannot be said for the ITO-COOH bond. This explains the difference in the literature  $A$ -values. The value of  $A$  obtained in this work is 445 nS which is right in

between the two values reported.

### *Conclusions*

The purpose for these measurements was to test the reliability of ITO for nanoscale measurements. That is why the molecules tested were extremely simple in nature and could be thought of as ideal molecules. It was seen that even with the simple and ideal molecules, the measurements were not straightforward. The raw data showed steps that had a wide distribution and when put together in a histogram, the standard deviation from the mean conductance was also spread over a wide range. The second conductance peak was not clearly visible at all, whereas for gold-thiol systems, as many as three conductance peaks are clearly visible. In spite of the difficulties, it was clear that reliable single molecule measurements on the ITO, though difficult, were not impossible.

### 3.3 Conductance Measurement of Dyads in the Dark

As illustrated in the previous section, the ITO surface proved suitable for carrying out break-junction measurements. Hence the next step was to deposit Dyad monolayers on the ITO and measure conductance values.

### *Synthesis of significant molecules*

All molecules were synthesized by Dr. Paul Liddell from the Gust-Moore group at Arizona State University. Figure 3.5 illustrates the synthesis of 5-(4-Carboxyphenyl)-20-(4-pyridyl)-10,15-bis(2,4,6-trimethylphenyl)porphyrin which will be referred

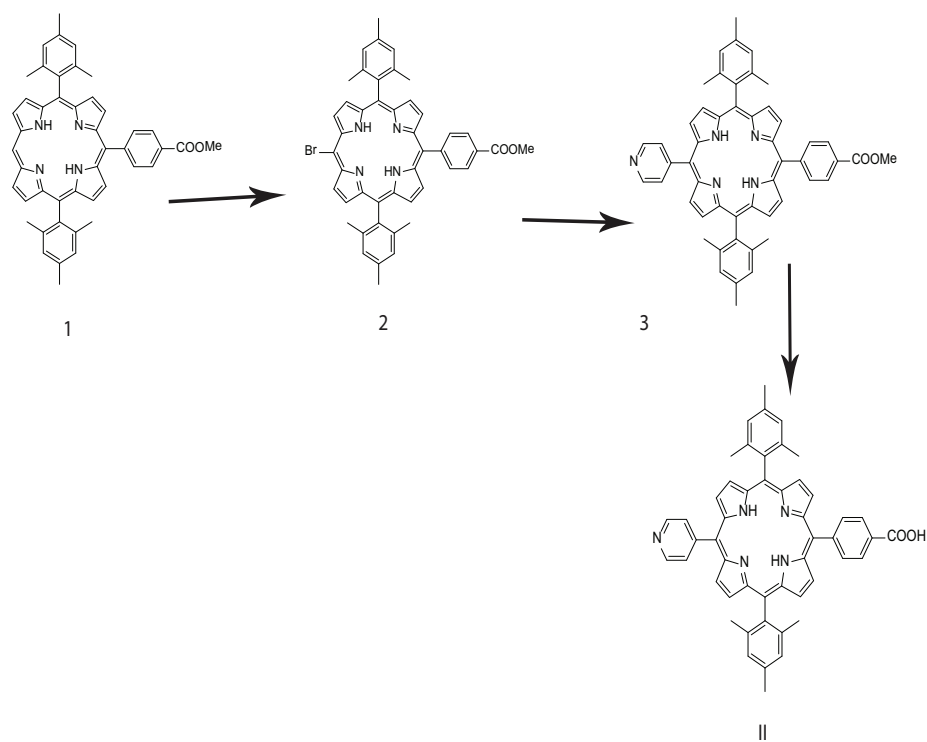


Figure 3.5: Synthesis schematic for 5-(4-Carboxyphenyl)-20-(4-pyridyl)-10,15-bis(2,4,6-trimethylphenyl)porphyrin (II). (Synthesized by Dr. Paul Liddell)

to as molecule II. This molecule has been used as a control in chapter 4. The purity of all the reaction intermediates (1,2,3) as well as the final product II was verified with the help of NMR spectroscopy. The figure 3.6 shows the synthesis of the porphyrin-fullerene dyad. The molecule is preserved in the form of the more stable dyad tert-butyl ester (5) until it is ready for use. Once ready to be used, the molecule is de-protected with the help of trifluoroacetic (TFA) acid and washed repeatedly with water till all the TFA is rinsed out and the molecule is neutralized. This step is important as the neutralized molecule has the -COOH group which binds with the ITO surface. The final deprotection step was done in

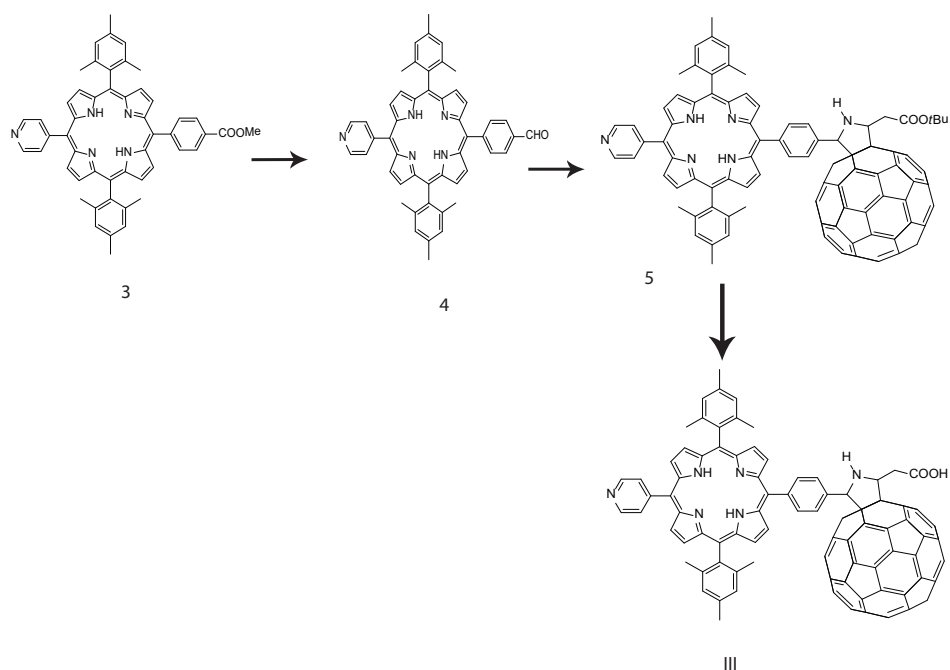


Figure 3.6: Synthesis schematic for porphyrin-fullerene dyad (III).

the Lindsay lab at the Biodesign Institute, ASU.

### *Dyad monolayer deposition*

The commercially available ITO consists of a thin film, a few microns thick, of ITO deposited on a glass slide. The ITO was cleaned by sonicating in water, ethanol and acetone for 5 minutes each and drying in nitrogen. It was then cleaned with oxygen plasma for 5 minutes to ensure the removal of all organic contaminants from the surface. (Milliron et al., 2000; Osada et al., 1998; Sugiyama et al., 2000; Wu et al., 1997) The dyad solution was prepared by dissolving a pinch of the powder in 5 ml mesitylene which had been previously purged with argon. The

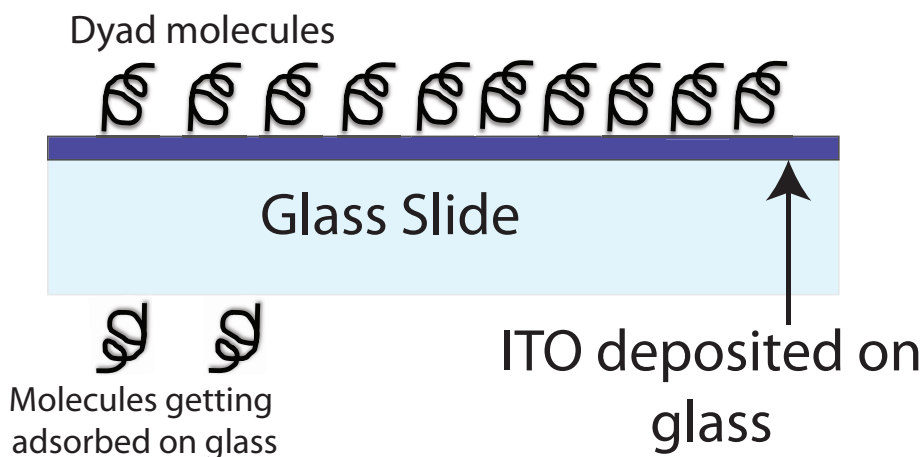


Figure 3.7: Schematic of Dyad monolayer formation on ITO. Some Dyad molecules tend to adsorb to the glass slide and are removed with solvents to maintain data accuracy.

resulting solution was sonicated for 2 minutes. The solution was then diluted 50 times and the UV-visible spectrum was recorded. Homogeneity between different batches of solutions was ensured by keeping the absorbance same from one batch to the other with the help of adequate dilution with mesitylene. The ITO was then immersed in the dyad solution and left overnight (24 hours) for monolayer deposition. After deposition, the ITO was washed with copious amounts of oxygen-free mesitylene. As seen in the figure 3.8 UV-visible spectrum was the recorded to ensure monolayer formation before utilizing the sample for break-junction measurements. The dyad molecules adsorb on glass (refer figure 3.7). Hence, before recording the absorbance of the sample, it was necessary to remove

the dyads sticking onto the glass surface of the slide which would otherwise skew the data. The glass surface was carefully washed with dichloromethane (DCM) repeatedly and then dried with nitrogen to ensure removal of dyads. The absorbance data thus obtained was due to the dyads attached on the ITO surface only.

#### *Dyad monolayer calculation from absorbance spectra*

In order to get reliable results from the break-junction measurements, it was very important to verify that we indeed have a monolayer on the surface. One way to do this was to calculate the estimated surface coverage of the slide from the absorbance ( $A$ ) data. From Beer-Lambert's law, we have:  $A = \epsilon \times c \times l$  where ( $c$ ) is the concentration of the molecules, ( $\epsilon$ ) is the extinction co-efficient and ( $l$ ) is the pathlength traveled by light and is usually unity. This is a good way to determine the concentration of unknown solutions when the extinction co-efficient is known.

For the Dyads, the extinction co-efficient was determined in a solution. However, the concentration that was required to be measured was that of the Dyad molecules deposited on ITO. In order to enhance the absorption signal, a "sandwich" of two slides was used for the measurements. The gap between the slides was purged with Argon before the measurements. Spectroscopic measurements

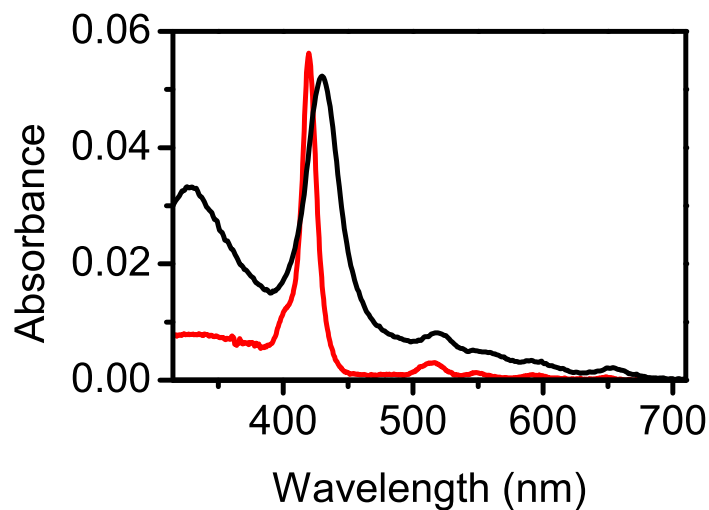


Figure 3.8: Red line represents the absorbance spectrum of Dyads in mesitylene solution after being diluted 50 times from the original deposition concentration. Black line represents the spectrum of the Dyads deposited on ITO/glass substrate. The Soret band appears at 419 nm for the solution spectrum whereas it is slightly shifted (to 430 nm) and broadened for the Dyads on ITO. The four Q-bands appear at 519, 554, 593, and 652 nm. (Battacharyya et al., 2011)

showed that the absorbance of the double slide increased by 0.052 at the Soret band wavelength (430 nm) after formation of the molecular adlayer (see figure 3.8). So, the absorbance of each slide increases by 0.026. The extinction coefficient of the dyad in mesitylene solution,  $\epsilon$  is  $507,770 \text{ (moles/liter)}^{-1}\text{cm}^{-1}$  at 419 nm. Taking into account the fact that the Soret band width in the film (see figure 3.8) is 2.67 times broader than that in the solution, it can be estimated that  $\epsilon$  of the film is  $190,000 \text{ (moles/liter)}^{-1}\text{cm}^{-1}$  at the Soret maximum of the film. So, the concentration of molecules on the slide:

$$c_{slide} = \frac{A}{\epsilon l} = \frac{0.02}{190,000 \times 1} \approx 0.1 \text{ micromoles}$$

Lets say the number of molecules in a  $1\text{cm}$  pathlength with an area of  $1\text{cm}^2$  and concentration of  $10^{-7}$  moles/L is  $N$ .

$$N = 1\text{cm} \times 1\text{cm}^2 \times 10^{-7} \frac{6.023 \times 10^{23}}{1000} \approx 6 \times 10^{13} \text{ molecules in a } 1\text{cm}^2 \text{ cross-section}$$

beam of  $1\text{cm}$  pathlength. (Note:  $6.023 \times 10^{23} = \text{Avogadro's number}$ )

If all these molecules were on a  $1\text{cm}^2$  surface area, then the area per molecule would be

$$\frac{10^{-4}\text{m}^2}{6 \times 10^{13}} = 1.6 \times 10^{-18}\text{m}^2 \text{ or } 1\text{nm}^2.$$

Molecular mechanics modeling shows that a densely packed monolayer could accommodate  $0.6 \times 10^{14}$  molecules/ $\text{cm}^2$  and hence these numbers are consistent with the formation of a monolayer.



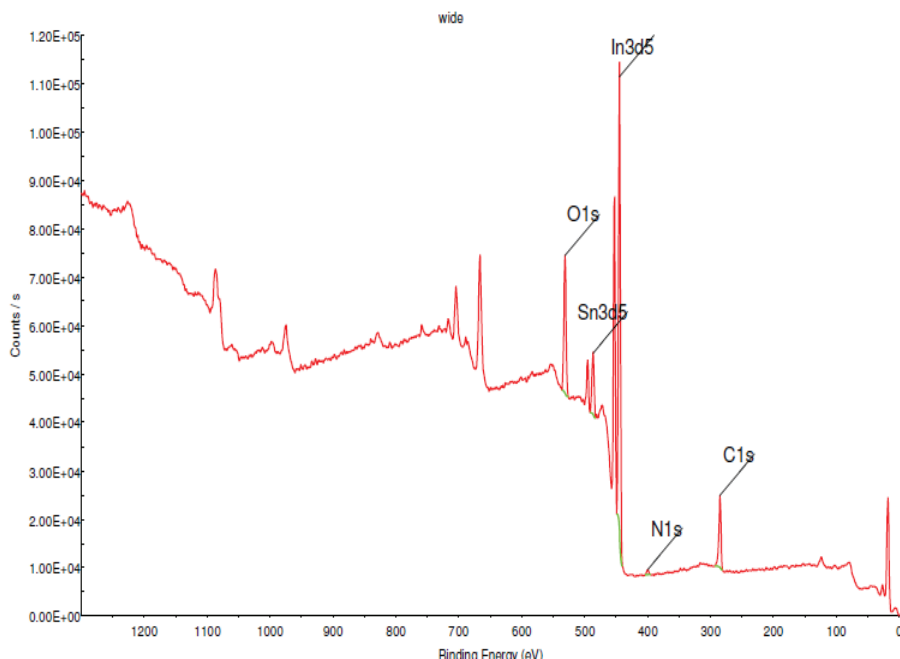


Figure 3.9: Angle resolved XPS data of Dyad molecules on ITO at a surface angle of 0 degrees.(Battacharyya et al., 2011)

*Dyad monolayer confirmation: X-ray photoelectron spectroscopy*

Dyad samples were prepared using previous procedures. The X-ray photoelectron spectroscopy (XPS) measurement was conducted by Timothy Karcher at the LeRoy Eyring Center at ASU. The figure 3.9 shows the spectrum of Dyads at a surface angle of 0 degrees. The nitrogen signal indicates the presence of the molecular adlayer. Fits to the angular dependence of these data yield a molecular layer thickness of 1.95 nm which is consistent with a slightly tilted monolayer.

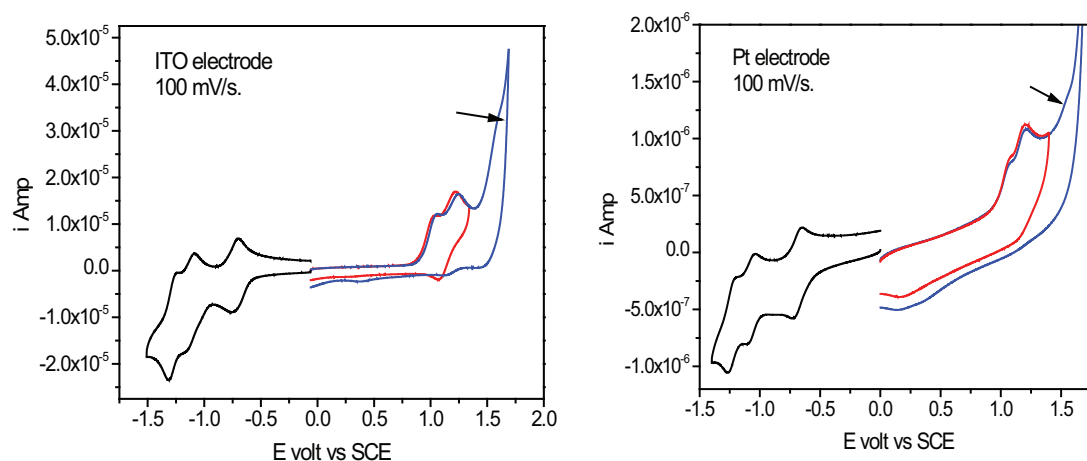


Figure 3.10: Cyclic voltammograms of Dyad molecules dissolved in dichloromethane containing 0.1 M tetra-*n*-butylammonium hexafluorophosphate with ITO the as working electrode (right) and the same solution with Pt as the working electrode (left). (Data obtained in collaboration with Dr. Miguel Gervaldo, Gust-Moore group, Arizona State Univeristy)

### *Electrochemistry of Dyads: cyclic voltammetry*

Cyclic voltammetry (CV) of dyad III in dichloromethane solution containing 0.10 M tetra-*n*-butylammonium hexafluorophosphate supporting electrolyte was carried out using an ITO working electrode, a platinum counter electrode, and a Ag/AgCl quasi-reference electrode. The electrochemical reduction shows three reversible one electron processes between 0 and -1.5 V vs SCE. The two first reductions, at -0.73 and -1.13 V, correspond to the formation of the mono- and dianion of the C60 unit respectively, and the third one at -1.28 V is due to porphyrin anion formation. The cathodic sweep shows three oxidation waves. The two first oxidations, at 1.04 and 1.22 V, correspond to the formation of the mono-

and dications of the porphyrin unit respectively, and the third one at 1.56 V is due to C60 cation formation. For purposes of comparison, we note that the CV of III in dichloromethane solution containing 0.10 M tetra-n-butylammonium hexafluorophosphate supporting electrolyte and using a platinum working electrode features reduction waves at -0.69, -1.09 and -1.24 V while oxidation waves are at 1.07 and 1.20 and 1.54 V vs SCE. (Electrochemistry measurements were performed in conjunction with Dr. Miguel Gervaldo (Gust-Moore group) at Arizona State University.)

#### *Break-junction measurements*

Break-junction measurements on the dyad samples were performed in a method very similar to the alkanes, explained in the previous section. All measurements were performed immediately after measuring the absorbance of the slides (to ensure monolayer formation). The STM probe was approached at -0.4 V sample bias. The negative sample bias was used in order to facilitate bonding of the pyridine to the gold STM tip. (On reversing the bias, the "steps" in the decay curves were sparse and not sufficient to construct a histogram.) (Andreasen et al., 1997; Cai et al., 1998) The current-time traces showed distinct steps (see figure 3.11 which were recorded and then selected with the help of the previously mentioned Labview program to create the conductance histogram. Note: This Labview program is the same as the one used for analyzing alkane data. We will be discussing

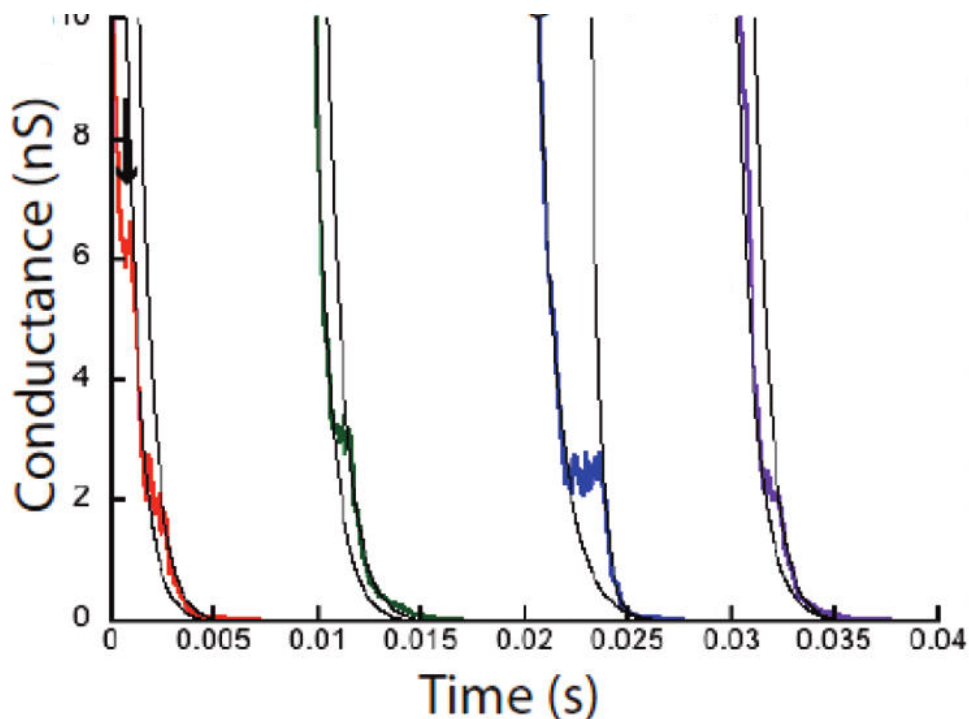


Figure 3.11: Typical conductance versus time traces as the probe is retracted at a speed of 20-40  $nm/s$  from the surface. The "steps" correspond to a dyad molecule caught in the ITO-gold probe junction. Exponential functions are fitted to each side of the "steps".(Battacharyya et al., 2011)

a new program which only takes into account the "steps" without the exponential background in the next section. The conductance histogram showed a (see figure 3.12) feature at around  $2.4 \pm 0.2$  nS. This feature seemed likely to correspond to the conductance of a single dyad molecule caught between the gold and the ITO electrodes. However, the feature was not as distinct as those obtained with the alkane molecules. This is due to the fact that the dyad molecules have a highly complicated geometry of attachment due to the complicated structure of the molecule. Hence, in spite of the fact that the raw current-time traces showing distinct steps, once put together into a histogram, the data appeared noisy and

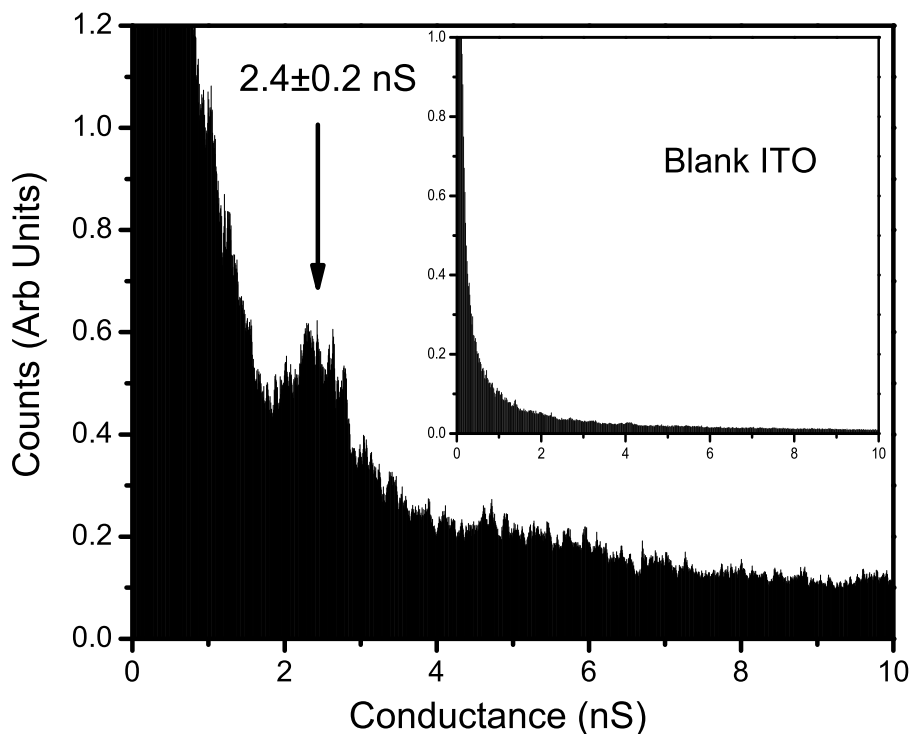


Figure 3.12: Conductance histogram of dyad molecules on ITO performed at -0.4V tip bias and 0.1 nAmp current set point. The standard deviation between different sets of measurements are reported as error. Inset shows control experiment at the same bias and current set point on blank ITO. (Battacharyya et al., 2011)

indistinct. Resolution was improved by using a different method for analyzing the data.

#### *Data analysis: "Step" analysis*

We saw, in the previous section, that it was difficult to discern the conductance peak in the Dyad histogram, in spite of the individual curves showing well-defined

"steps" in figure 3.11. One way to differentiate peaks from noise is to remove the sloping background from conductance histograms. The curves are essentially exponential decays, so a current versus time curve has more data points at low current. When these curves are compiled into a single histogram, it leads to significant sloping background, where very low conductance values have very high counts in the histogram. This can make it difficult to read peaks that may be lower in conductance. In order to remove the background of the histograms, it is beneficial to only compile the points within the step/plateau, and not the rest of the curve. (Chen et al., 2005) To counteract this problem, a step analysis program was created in Labview. This procedure has been previously reported in determining the conductance of oligoalanine. (Chen et al., 2005) This program has a window of a certain number of data points that was automatically slid over the entire decay curve. In order to determine if a step occurred within the window of data, a histogram of the data in the window was produced. The maximum and minimum count values in the window was calculated and if it was above a certain threshold, and if the maximum occurred in the middle of the window, then the position of that maximum value is assigned one single count. If it did not meet the criteria, then the count was still zero. The step analysis method proved successful for analyzing the data obtained for dyad molecules. Figure 3.13 shows a histogram of the conductance of dyad molecules analyzed by the step analysis

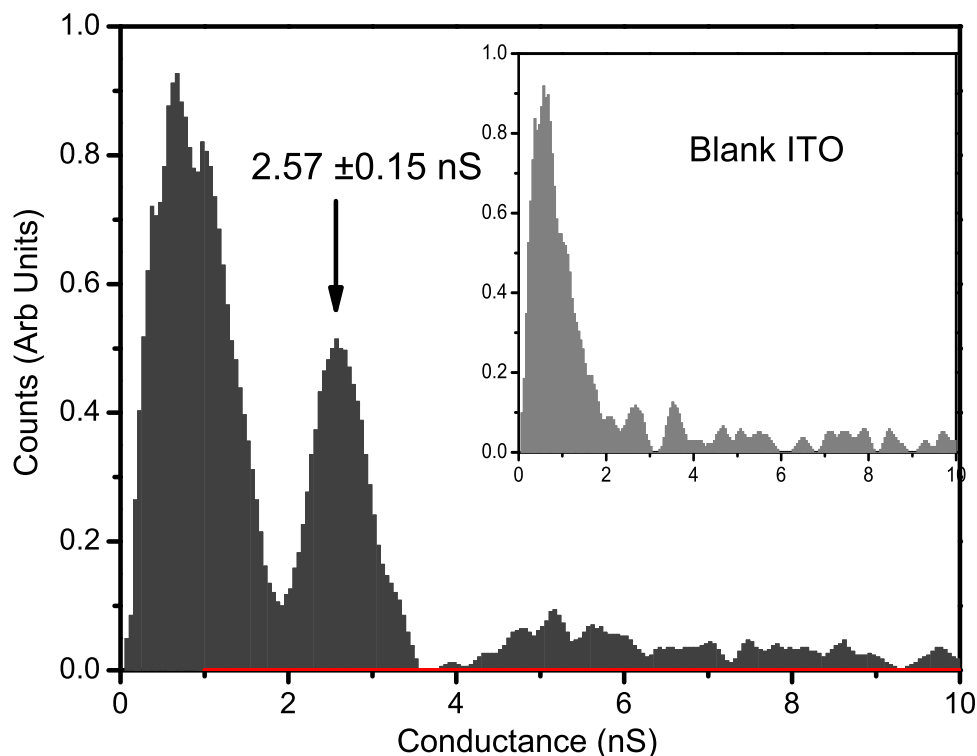


Figure 3.13: Conductance histogram of dyad after analyzed with the step analysis program. Removal of exponential background reduces noise and makes the first peak more obvious. Break-junctions on a blank substrate is shown as the inset.

program. When compared with figure 3.12, it is obvious that the value of the conductance does not change. However, the data looks more clean and the first conductance peak is readily identifiable. A point worth noting in this context is the feature at 1.0 nS which is pervasive in all histograms obtained with the "step" analysis program. This feature is an artifact of data analysis and is present even in the blank measurements. Hence, it will not be considered as the first conductance peak. Throughout the next chapter, "step" analysis will be the preferred method

of analyzing data and compiling histograms.

### 3.4 Conclusion

In this section, we found a proper and reproducible method to deposit monolayers of dyad molecules on the ITO surface. As a conclusion to this section, we can safely state that we have developed and perfected a method to collect and analyze the conductance data obtained from break-junction measurements on dyad molecules on ITO.



## Chapter 4

### STM break junctions under illumination

This chapter talks about the instrumentation involved in setting up a novel sample stage in order to conduct STM break junction measurements under illumination. This chapter also goes into details of how the molecular conductance varied with illumination. A significant and unexpected change in conductance was observed when Dyads were illuminated. Because of this, the STM results were also verified by fluorescence microscopy which will also be discussed in this chapter.

#### 4.1 Experimental Set-Up

Normally, STMs are not set-up to perform experiments under illumination. In fact, the microscope is normally positioned inside a Faraday cage and positioned on a vibration isolated stage to cut out the noise. Hence, operating the STM under illumination means setting up a system of fiber optics and lenses to deliver laser light onto the sample.

##### *Laser beam delivery*

The laser used for illumination was an Ar/Kr laser (CVI Melles-Griot, Albuquerque, NM) which could operate at a series of wavelengths from 476 to 676 nm. The maximum power obtainable was around 10s of milliwatts. A single mode optical fiber was attached to the laser and the other end of the fiber was

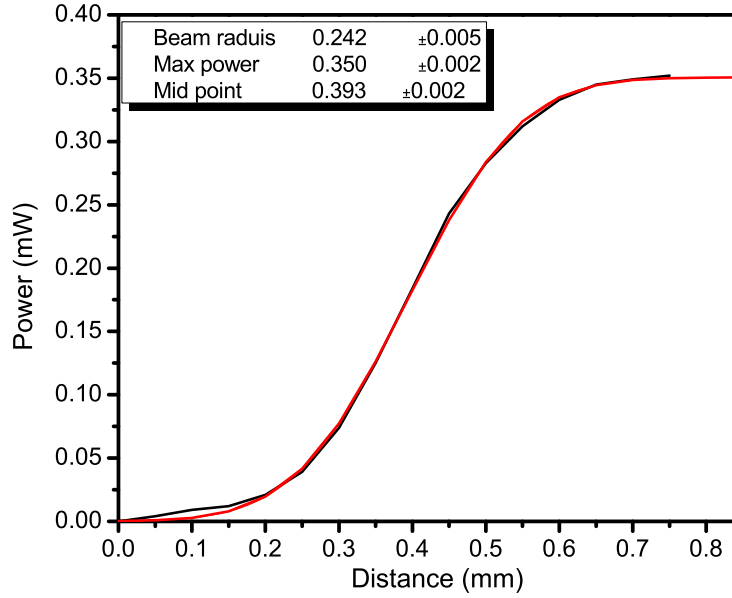


Figure 4.1: Error function fitting of data obtained from beam diameter measurement. The beam diameter was determined to be  $0.484 \pm 0.005$  mm.

coupled with a multi-axis lens positioner. The purpose of the lens positioner is to focus the laser beam into a tight spot on the sample.

#### *Beam diameter measurement*

The laser power at the sample could easily be measured with the help of a four quadrant detector (obtained from Thor labs). However, for the purpose of accuracy in measurements, it was important to know the power density. This determined by finding out the beam diameter of the laser at the point where it hit the sample. The laser was assumed to emit a beam that approximates a Gaussian profile. The width of the laser beam is taken as the distance between the points

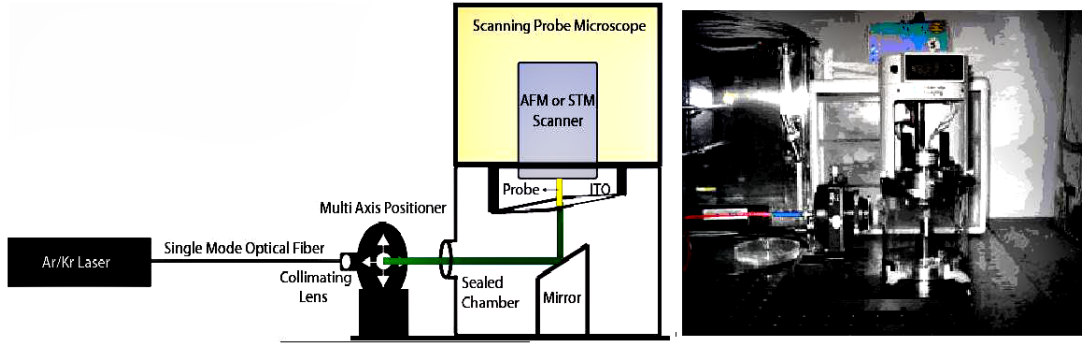


Figure 4.2: Right shows the instrumentation of the illuminated STM set-up. It can be used with the AFM as well. Left shows the actual microscope with the fiber optic connected to it.

where the intensity falls to  $1/e^2 = 0.135$  times the maximum value. The actual measurement was done by cutting the laser spot slowly with a blade attached to a micrometer and recording the intensity at frequent intervals. The data was then fitted to an error function and the beam diameter was determined from the graph.

Figure 4.1 shows the beam diameter to be  $0.484 \pm 0.005$  mm.

### *Illuminated STM*

The instrument design of the illuminated STM is depicted in figure 4.2. Due to the microscope design, the sample had to be illuminated from underneath the sample plate. Hence a hole was bored into the sample plate and the ITO sample was positioned right above the hole. The fiber optic (from the previous section) which was connected to a multi-axis lens positioner was placed on an aluminium bread-board. A 0.3 optical density neutral filter was placed in front of the multi-axis lens positioner for these measurements in order to get a very low illumination inten-

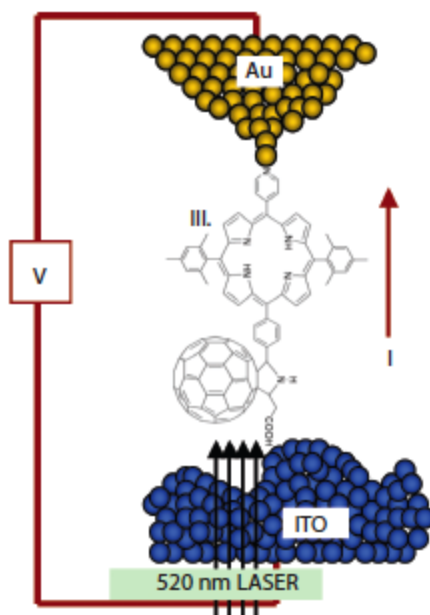


Figure 4.3: Schematic of break junction measurements of Dyads under illumination. (Battacharyya et al., 2011)

sity. A controllable optical shutter (Thor Labs) was placed in front of the filter and could block the beam or allow the light to pass through depending upon the applied voltage on the shutter (determined by a separate controller). Also on the breadboard was an environmental chamber which housed the microscope. The environmental chamber was designed to have an optical window which would allow the laser light to travel through. On entering the environmental chamber the collimated laser beam would hit a mirror positioned at a 45 degree angle and would then be directed to the sample plate and thereby the ITO sample. The schematic is illustrated in figure 4.3

Since the molecules are thought to be prone to irreversible photo damage, it

is important to understand whether any changes in conductance of the single molecules are due to illumination or photo damage. A single sample, therefore, needed to be measured in both the light and the dark during the same experiment. To accomplish this, the optical shutter controller was set to automatically open and close every ten minutes. To track which data were taken with the shutter open and which data were taken with the shutter closed, a signal line from the voltage output on the shutter controller was connected to the oscilloscope. Every recorded curve also recorded the voltage on the shutter, which could be used in data analysis in order to determine whether the sample was illuminated or not during a given tip retraction. In this way, the same part of the sample can be probed under light and dark conditions automatically, and the reversibility of any changes in the molecules examined.

#### *Sensitivity of dyads to atmospheric oxygen*

The dyad molecules proved to be extremely sensitive to atmospheric oxygen. In the presence of oxygen diradicals, the dyads would undergo irreversible chemical change and ultimately disintegrate into some other species over time. The time window for this chemical change was not too long and according to timeline studies, irreversible changes in conductance would be noticeable even after 3 hours under normal atmospheric conditions. This was an important observation because it proved the necessity of strict environmental control while performing

the measurements. This was done by freshly distilling the solvent mesitylene before each experiment. The distilled mesitylene was further sparged with Ar in order to expel the dissolved oxygen from the solvent. The whole STM was submerged in an air-tight environmental chamber filled with Ar gas. The solvent was changed every hour and the experiments were not allowed to run beyond 3 hours. Thus, data was collected over a period of two or three days (using a freshly prepared sample each time).

## 4.2 Results

The molecules tested by illuminated break junction method are shown in figure 5.2. The dyad molecules were the ones that were tested for the purpose of utilization as a photovoltaic device and the others (I and II) were meant to be controls to determine the exact mechanism of electron transfer in the Dyads. As mentioned before, the dyad molecules are extremely sensitive to atmospheric conditions. it was also found that they are sensitive to high laser power intensities. The threshold value of laser power intensity was established to be  $300\text{ mW/cm}^2$  beyond which molecule III showed irreversible photodamage. Therefore the laser power intensities tested were all below the threshold value. The figure 4.5 shows the conductance histograms performed at laser intensity of  $183 \pm 13\text{ mW/cm}^2$ . Recall, from chapter 3, that the peak between 0-1 nS in the histograms is an artifact of the data analysis and occurs in control experiments with clean samples as well. The

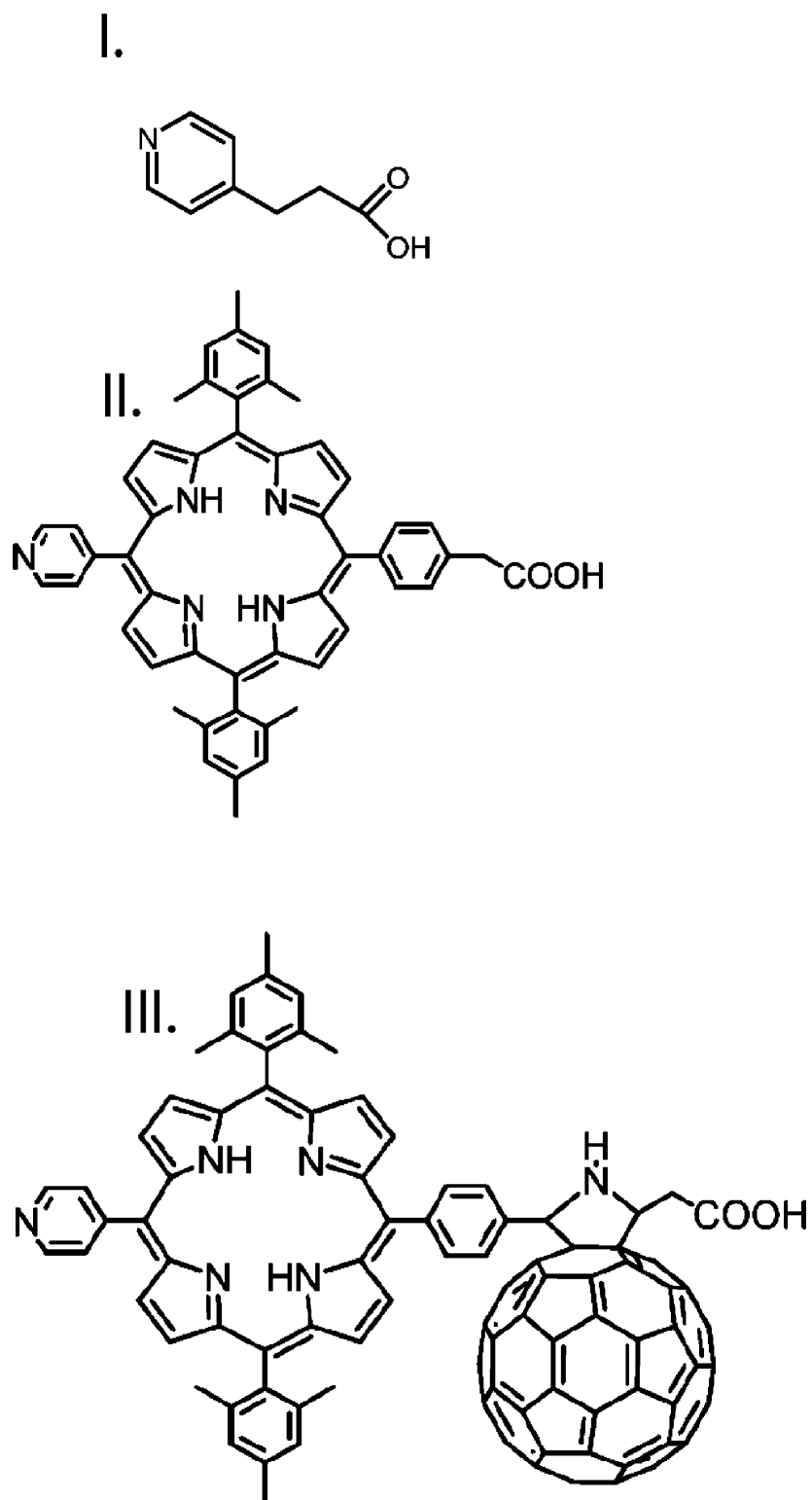


Figure 4.4: Molecules tested by illuminated break junction method. I: 3-(pyridine-4-yl)propionic acid, II: 5-(4-Carboxyphenyl)-20-(4-pyridyl)-10,15-bis(2,4,6-trimethylphenyl)porphyrin, III: Dyad (Battacharyya et al., 2011)

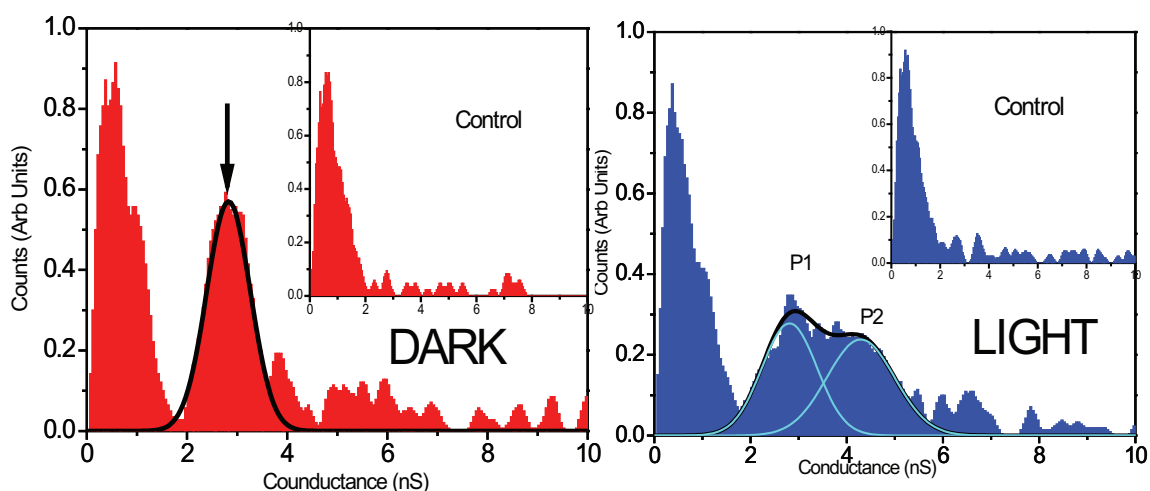


Figure 4.5: Right-Distribution of conductances for the dyad in the dark. The peak near zero nS is seen on a bare ITO substrate (inset). The feature at 2.5 nS (arrow) is only observed when a monolayer of the dyad molecules is present (solid line is a Gaussian fit). Left-Distribution of conductances for the dyad illuminated at 520 nm (200 mW/cm<sup>2</sup>). The current distributions were converted to conductance using the probe bias of -0.4V. Illumination generates a second conductance peak (P2) at 4.3 nS.(Battacharyya et al., 2011)

figure 4.5-right shows the conductance histogram of III without illumination and the figure 4.5-left shows the conductance histogram when the molecule III was under illumination. In the dark, the histogram shows the peak typical of the dyad molecules centered at 2.45 nS (P1). the inset shows the control measurement with no dyad molecules on ITO. The illuminated histogram looks remarkably different. While the peak centered at 2.45 nS still appears in the histograms, it is much broader than the ones typically seen in dark. In addition to that, there is another peak appears at 4.3 nS (P2) which is not seen in the dark. The feature disappears on cutting off the illumination but reappears on re-illumination. This happens



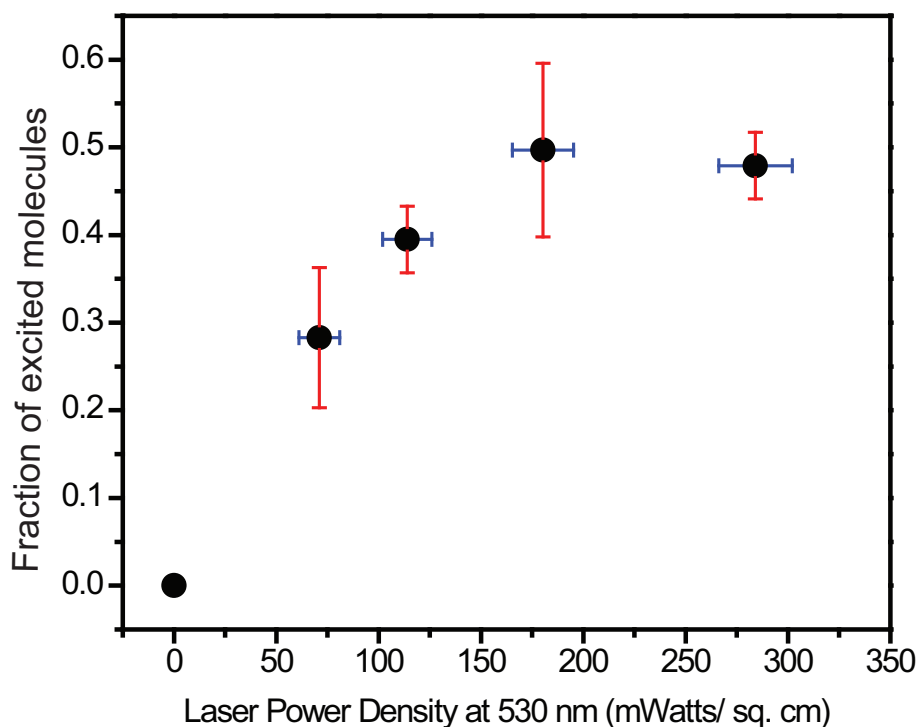


Figure 4.6: Fraction of molecules in the excited (P2) state as a function of laser power density. The number of molecules in each state is taken to be proportional to the product of the height and width of the Gaussian fits. The number of molecules in the high conductance (P2) state falls once the power density exceeds 200 mW/cm<sup>2</sup>. (Battacharyya et al., 2011)

repeatedly for the whole duration of the experiment (3 + 3 hours). This was clear evidence for a reversible increase in photoconductance, possibly due to the formation of a different species due to laser illumination at 520 nm.

The same experiment was repeated at various laser intensities to determine whether the changing photoconductance was, in any way related to the laser intensity. Initially, it was found that laser intensities above 300 mW/cm<sup>2</sup> caused

irreversible photodamage of the molecules. On trying various lower laser intensities, it was found that very low intensities (lower than  $50\text{ mW/cm}^2$ ) do not produce any significant change in the conductance histograms of the dyad molecules. Therefore, keeping in mind the small window of laser intensity, the various laser intensities tested out were:  $71 \pm 10\text{ mW/cm}^2$ ,  $114 \pm 12\text{ mW/cm}^2$ ,  $180 \pm 15\text{ mW/cm}^2$  and  $284 \pm 18\text{ mW/cm}^2$ . The first conductance peak obtained in both dark and under illumination was called P1. The peak appearing only under illumination was called P2. In order to estimate the number of molecules showing the enhanced photoconductance, the peaks were fitted with a Gaussian function. The area under the peaks were calculated using the formula:  $Area_{P1} = (FullWidthHalfMaxima)_{P1} \times (Height of Peak)_{P1}$  and  $Area_{P2} = (FullWidthHalfMaxima)_{P2} \times (Height of Peak)_{P2}$ . In order to obtain the fraction of molecules of changed photoconductance, the following formula was employed: Fraction with increased photoconductance =  $\frac{Area_{P2}}{Area_{P1} + Area_{P2}}$ . This fraction was plotted against the laser power intensities (as shown in figure 4.6). It was seen that, the fraction increased steadily with increasing the laser intensity until it reached a maximum of 50 % at  $183 \pm 12\text{ mW/cm}^2$ . On increasing the laser intensity further, this fraction did not increase any further but plateaued at around 50 %.

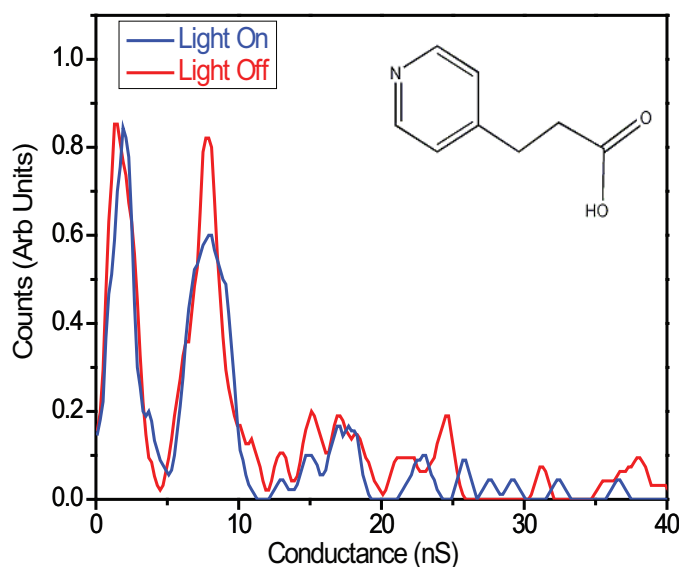


Figure 4.7: Control experiment with 3-(pyridine-4-yl)propionic acid (inset). Red line represents light off experiment and blue line represents light on experiment. This molecule has the same end groups as the Dyads but no porphyrin-fullerene moiety. No visible effect is observed in the molecule due to laser illumination proving the light-independent nature of the end groups

#### *Control experiments*

The dyad molecules have a complex chemical structure. In order to determine what the increase in photoconductance is due to, it was important to eliminate all other possibilities that could lead to increased conductance. Hence the molecules I and II were tested in the exact same way as the Dyads and the results were compared. Figure 4.7 shows the control experiment with molecules that have the same end groups as the dyads but no pyridine-fullerene moiety. The conductance histograms were plotted with lines and the light and dark histograms superim-

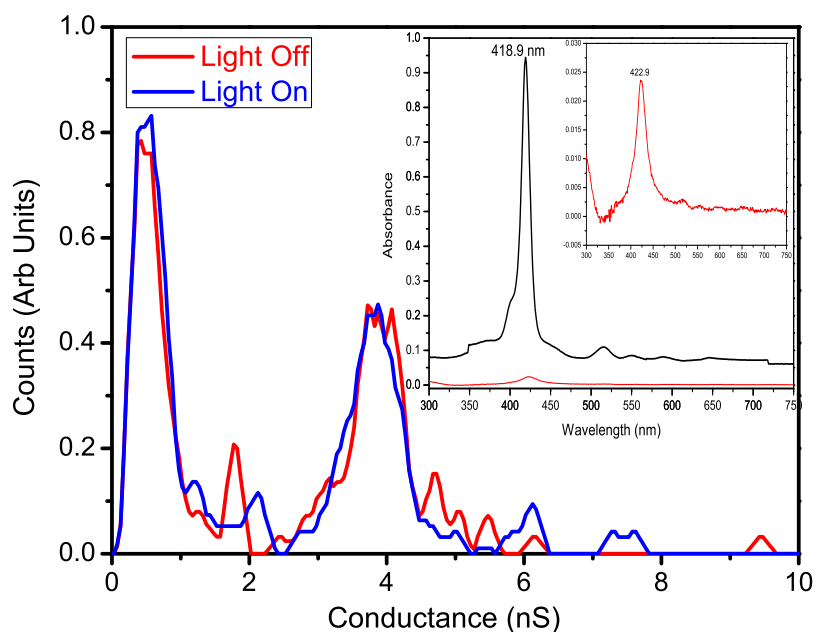


Figure 4.8: Control experiment with porphyrin without fullerene. No visible effect observed in histograms due to laser illumination proving the necessity of the fullerene group to produce a long-lived charge separated state. Inset: Black line shows porphyrin spectrum in solution and red line is porphyrin spectrum on ITO surface. Inset of Inset is a blown up spectrum of porphyrin on ITO which proves the presence of monolayers on the ITO surface.

posed to facilitate the comparison of the two histograms. This experiment with a molecule having the same end groups but no reaction center was done in order to determine whether the end groups undergo any change upon exposure to laser illumination. As seen in figure 4.7, upon laser illumination, there is no change in the conductance of the first peak. This proves that a donor-acceptor system is necessary to bring about changes in the photoconductance. The change is not due to polymerization of the end groups or some other non-photo induced transition.

The second molecule tested was was II. It has the identical same structure as the

Dyad sans the fullerene attachment. The purpose of testing this molecule was to determine the role of the fullerene and to get an insight into the conductance mechanism through the dyad. Figure 4.8 shows the conductance histograms in the dark (red) and after illumination (blue) of molecule II. The molecules were deposited in the same way as the dyad molecules and the absorbance spectrum was used to determine the monolayer formation (inset). Similar to the dyads, Soret band of II showed a slight shift on being deposited on the ITO (inset of inset). Interestingly, it was observed that there was no change in the conductance histogram of the molecule upon illumination. This proved that a fullerene (or an acceptor) is necessary to be positioned within very close proximity of the chromophore or the donor to facilitate the electron transfer.

### *Spectroscopy*

The data from the break-junction measurements indicated a species with enhanced conductance. It was not due to irreversible photochemistry or photocurrent (calculations will be discussed later in the next section). Therefore, the evidence was in favor of a charged species (Kodis et al., 2004; Zhang et al., 2002), possibly a  $\dot{P}^+ - C60^-$  (where P= porphyrin and C60= fullerene) that lived long enough to be detected by the electronic measurements. If that was a true prediction, then the  $\dot{P}^+$  should be detectable by other spectroscopic techniques as well. The only

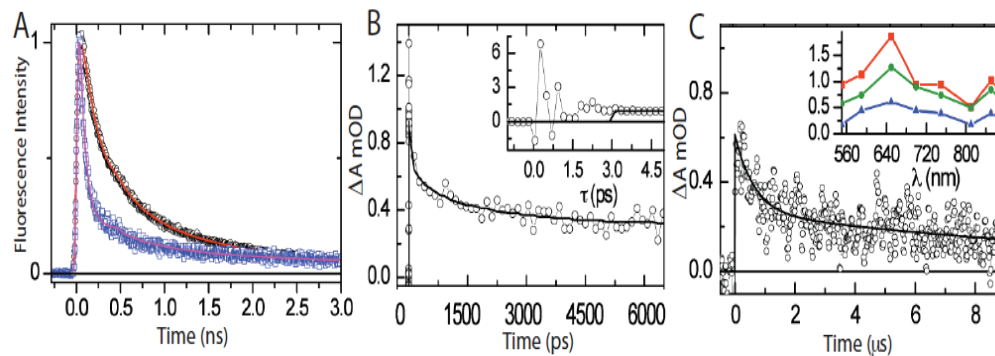


Figure 4.9: (A) Time-resolved fluorescence data for monolayer films of II (circles) and Dyads (squares) on ITO. (B) Transient absorption kinetics at 850 nm for a stack of six ITO-coated glass plates covered with films of Dyads following excitation at 520 nm. (C) The inset shows transient absorption spectra at 3 ps (red squares), 10 ps (green circles), and 2 ns (blue triangles) obtained with excitation at 520 nm for the Dyads. (Fluorescence spectroscopy done by Dr. Gerdenis Kodis) (Battacharyya et al., 2011)

problem was the fact that we were dealing with monolayers of Dyads which made the concentrations extremely low and hence, samples had to be prepared accordingly. Samples prepared for fluorescence studies had to be stacked together in order to enhance the fluorescence signal. The deposition of the monolayer was done in the same procedure as before. All fluorescence measurements were done with Dr. Gerdenis Kodis at Arizona State University. The molecules on the glass side of the slide was washed out using dichloromethane. The two slides thus prepared were stacked together with the glass sides facing each other and with air gap in between them. The air gap was purged with argon to keep the environment oxygen free as it has been noted previously that the molecules are susceptible to degradation when exposed to the atmosphere. Fluorescence decay studies were

conducted on films of II and III on an ITO-coated glass electrode in air and of III in mesitylene solution, with excitation into the Soret region at 420 nm (<10 pJ per pulse). The Figure 4.9A shows fluorescence decay kinetics for films of III (black circles) and for films of II (blue squares). the decay kinetics at 660 nm were fitted with exponential decays. The decay kinetics at 720 nm (not shown) of III in mesitylene solution were fitted with exponential decays and the majority (89%) of the molecules had lifetimes of 143 ps. The 143 ps lifetime is characteristic of singlet-singlet energy transfer from porphyrin to fullerene. Figure 4.9A shows fluorescence decay kinetics for films of III (black circles) and for films of II (blue squares). The decay kinetics at 660 nm were fitted with exponential decay and it was found that for film III, 90% of the molecules had a lifetime of 36 ps. The film of porphyrin II shows nonexponential fluorescence decay reflecting exciton migration from higher- to lower-energy states that result from heterogeneity of the molecular film. Transient absorbance measurements required stacks of six samples in order to enhance the signal sufficiently to be able to record measurements. Transient absorption pump-probe measurements were made with excitation at 520 nm ( 90 nJ, 100 fs pulse) to minimize excitation of the fullerene and ITO, and also at 430 nm near the Soert band of the porphyrin. Detection was conducted at 550-800 nm, a region which shows features of a porphyrin radical cation (see figure4.9B and C). Although the decays are non-exponential, they were fitted

with 5 exponents and showed a long-lived lifetime of 14  $\mu$ s. the other lifetimes were 40 ps, 290 ps, 1.95 ns. Control experiments were carried out with films of porphyrin II and the bare ITO on glass substrate. No measurable transient absorption signal at 700 nm was observed for either sample with excitation at 430 nm using 5 ns laser pulses.

### 4.3 Conclusion

The results obtained from the break-junction measurements point in the direction of a charge-separated state produced due to possible injection of electrons into the ITO. This charge injection would prevent the the swift recombination of the electron-hole pair and allow a state sufficiently long-lived to be detected in the break junction measurements. The absorption cross-section of the chromophores, calculated from the extinction co-efficient at 520 nm is  $1^2$  at 520 nm. A photon density of  $200\text{ mW}/\text{cm}^2$  corresponds to  $47\text{ photons}^{-2}\text{s}^{-1}$ . This means that 50 photons get absorbed by the molecule per second. The conductance value obtained is much greater than one would expect from photocurrent (which should be in the femtosecond range for a 1-3 molecules caught in the ITO-tip junction). Therefore, the state with enhanced conductance is most likely due to a charge separated state of the molecule. This theory is further supported by spectroscopic findings. The slightly higher fluorescence decay lifetime of film II on ITO is evidence of exciton migration over the film. This shows that con-



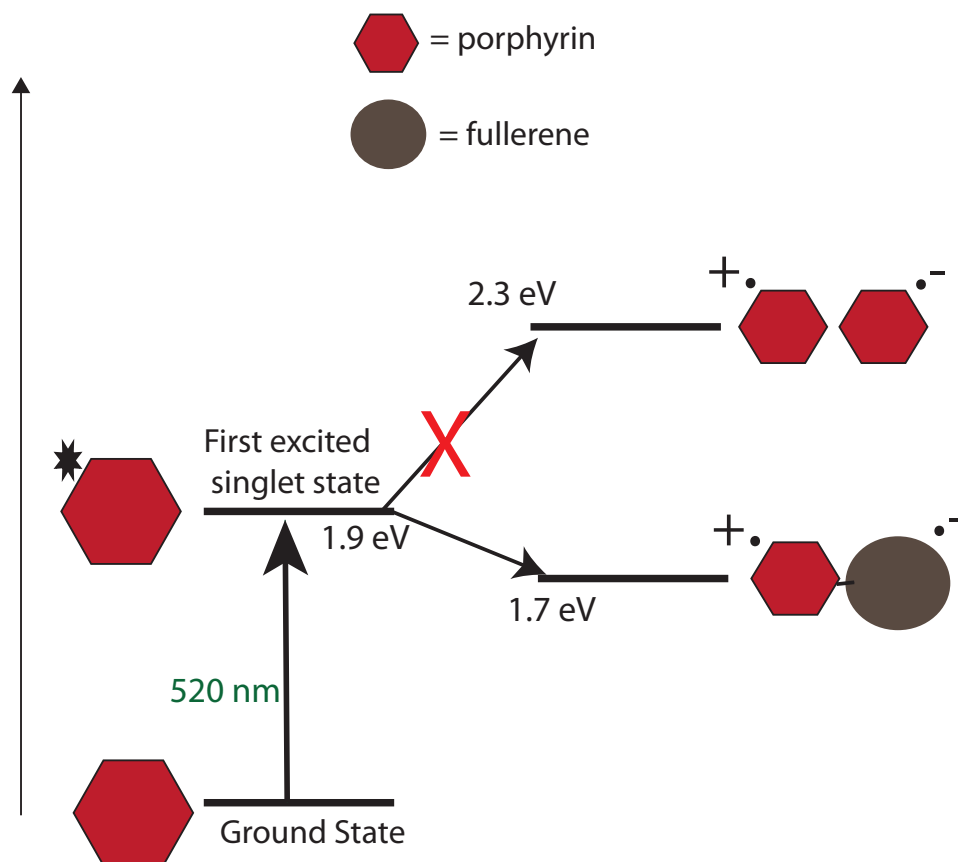


Figure 4.10: Energy level diagram of the possible processes occurring in the porphyrin-fullerene reaction center. (Energy levels drawn not to scale)

trol molecule II forms a film which is not highly ordered. However, the dyad (molecule III) on the other hand shows a much shorter lifetime of 36 ps. This is typically due to the formation of  $\dot{P}^+-\dot{C}_{60}^-$ . This is also seen in transient absorbance measurements which show a fast decay of 40 ps. Thus overall results are consistent with very fast decay of the porphyrin first excited singlet state by photoinduced electron transfer to yield molecular  $\dot{P}^+-\dot{C}_{60}^-$  charge-separated states, which migrate and decay over a variety of time scales forming long living polarons which exist for at least some microseconds. Spectroscopic evidence and

electrochemical measurements (figure 3.10) indicate that the energy of the first excited state of porphyrin is 1.9 eV. The  $\dot{P}^+ - \dot{C}_{60}^-$  species is at 1.7 eV and therefore electron injection into the  $C_{60}$  is a thermodynamically favorable process. However,  $\dot{P}^+ \dot{P}^-$  has an energy level of 2.32 eV and photoinduced electron transfer to this state is an endergonic process and therefore not favorable. This is depictorially depicted in figure 4.10 (Battacharyya et al., 2011; Gervaldo et al., 2010). The higher conductance of the charge separated species can also be explained with the HOMO-LUMO picture. Recall, from chapter 1 (equation 1.8) that the conductance increased with the decreasing HOMO-LUMO gap of the molecules. When the electron "hops" to the fullerene to create the  $\dot{P}^+ - \dot{C}_{60}^-$ , the HOMO-LUMO gap decreases. Therefore the charged species shows higher conductance. The conclusions deduced from this work are as follows:

- A large fraction of the porphyrin-fullerene Dyads remain in a charge separated state having enhanced conductance for at least a few microseconds.
- The recombination to the ground state occurs without any irreversible chemical change within a range of laser power densities.
- Spectroscopic evidence indicates the formation of  $\dot{P}^+ - \dot{C}_{60}^-$  which is absent in solution of on a film comprising of only porphyrins (Molecule II)
- Electrons are transferred (most likely by hopping conductance) into the

ITO which prevents rapid recombination

- These findings open new possibilities for charge extraction and may lead to new developments in the field of molecular photovoltaics.

## Chapter 5

### Molecular Rectification

This chapter looks at rectification in molecules, specifically for photovoltaic applications in a set of molecules synthesized by our collaborators at Yale. The goal is to design a rectifying molecule that facilitates electron or hole injection at the appropriate electrode to reduce recombination.

#### 5.1 Introduction

The concept of molecular electronics was illustrated in 1974 by Avi Aviram and Mark Ratner in a paper which outlined the design of an organic single molecule rectifier (Aviram and Ratner, 1974). The organic rectifier, like its solid-state counterpart, would allow current to pass only in one direction when connected between two electrodes and biased in that particular direction. Recall, from Chapter 1, that one of the major goals of molecular electronics is to mimic macroscopic electronic devices with molecules; the observation of molecular rectification is thereby rendered an important developmental milestone in this field. (Waldeck and Beratan, 1993) On the left side of the molecule is tetracyanoquinodimethane (TCNQ) which is an electron acceptor, meaning it can accept another electron at relatively low potential into its lowest unoccupied molecular orbital (LUMO). On the right side of the molecule (figure 5.1) is a tetrathiofulvalene (TTF) group.

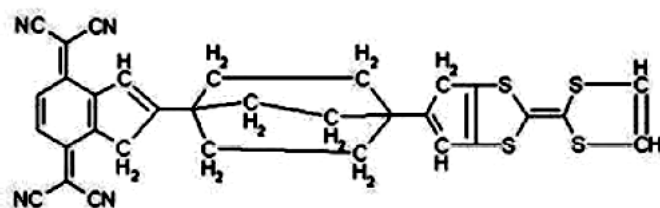


Figure 5.1: The Aviram-Ratner molecule (Aviram and Ratner, 1974)

This is a well-known electron donor, giving up an electron at low potential from its highest occupied molecular orbital (HOMO). The two groups are connected by a triple methylene bridge, so as to keep the orientation of the molecule stable. Recall figure 1.6 which shows the energy level diagram, once properly wired, for this molecular rectifier. The donor should be able to transfer an electron from its HOMO to the LUMO of the acceptor once the voltage reaches a certain threshold in one particular direction, but not when the bias is reversed. This means that the molecule should, theoretically, act in a similar manner to a solid state diode. Molecular rectification may occur when the molecules contain a dipole. If  $I$  is the measured current and  $V$  is the measured voltage, then for most molecules  $I(V) = -I(-V)$ . However, for some molecules,  $I(V) \neq -I(-V)$  and that is defined as rectification in molecules. (Mujica et al., 2002) Molecular rectification arises from asymmetry in the structure of molecules. First attempts to obtain molecular rectification were driven by Ratner and Aviram's proposal of 1974, where it was noted that a molecule, containing a donor (D) with low ionization

potential and an acceptor (A) with high electron affinity, separated by a saturated bridge (B), may act as a rectifier when located between two metallic leads. In the donor-insulator-acceptor (D-B-A) structure, the highest occupied molecular orbital (HOMO) and the lowest unoccupied molecular orbital (LUMO) are confined to two different parts of the rectifier, D and A respectively. The insulating bridge consists of  $\sigma$ -bonds and prevents the orbitals from "spilling over" to the other part. The Aviram-Ratner model can be thought to be occurring at two distinct stages. 1. At a particular value of applied voltage in the positive direction, the Fermi level of the electrode on A (cathode) aligns with the LUMO allowing electron tunneling from the Fermi level to the LUMO. Simultaneously, the D side aligns with the HOMO, resulting in electron transfer from the HOMO to the Fermi level of the electrode on D (anode). 2. At this voltage, the current rises sharply because the electrons can now be loaded onto the LUMO, then tunnel inelastically through the insulating bridge to the HOMO and then escape into the second electrode. This returns the molecule from its excited, ionized state to the ground state of the system D-B-A. In the opposite direction, a similar process does not occur until a much higher applied voltage. (Ashwell et al., 2004) The phenomenon of rectification is reversible and can be switched on and off with the voltage and no irreversible chemical change occurs in molecules. (He and Lindsay, 2005) Rectifying molecules can be applied in photovoltaics as it will allow electron

transport in one direction only, thereby preventing charge recombination.

## 5.2 Experimental procedure

The following molecules (refer fig 5.2) were synthesized (by Laura Allen, Yale) and according to theoretical calculations were supposed to show rectification. However, one of them was predicted to be more rectifying than the other. The electronic measurements were done "blindly", in that, we did not know the theoretical prediction at the time the measurements were made. As explained in the previous section, one of the ways to study molecular rectification is by performing I-V characteristics on a monolayer of the molecule using the STM.

### *Molecular monolayers*

In order to obtain reliable I-V characteristics, the first step was to get a proper monolayer on the surface of gold. This was achieved by tethering the molecules on the gold surface with the help of a gold-thiol bond. However, the molecules were obtained in the form of disulfides. Therefore, the first step was to break the disulfide bond in situ so the thiols attached to the gold surface. Once the disulphide bonds are broken in situ, the thiols react with the gold atoms and form a thermodynamically favorable Au-S bond. This bond is extremely exothermic and much more favorable, energetically, than the Au-N bond (see figure 5.2). Hence, it can be safely concluded that the actual binding to the surface occurs only at the thiol end and the N-rings are free for attaching to the STM

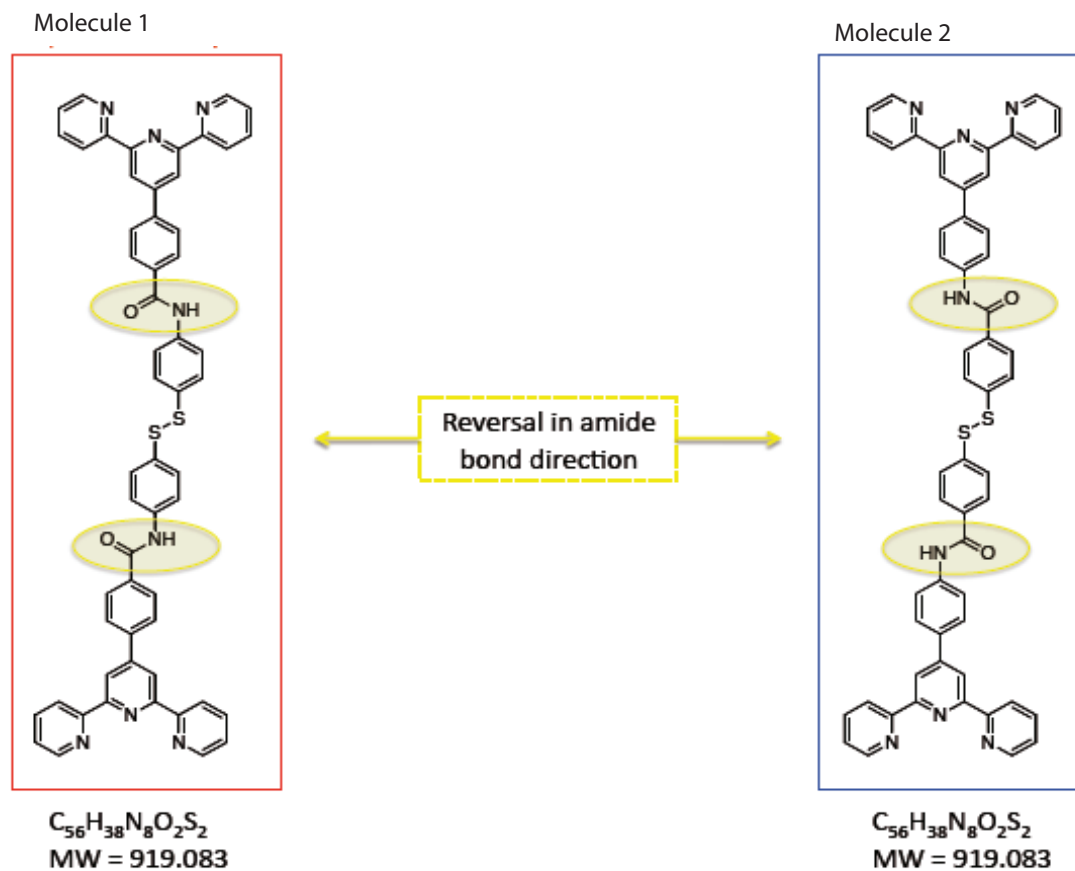


Figure 5.2: Molecules with identical molecular weight and formula but reversal in the direction of the amide bond. The molecule in the red box will be referred to molecule 1 and the one in the blue box will be referred to as molecule 2. (synthesized by Laura Martin at Yale)

tip. The breaking of the S-S bond was done using an equimolar amount of tris(2-carboxyethyl)phosphine hydrochloride (TCEP) (obtained from Sigma Aldrich) and the molecule 1 (see figure 5.2). 0.91 mg of the molecule 1 was dissolved on 1 mL DMSO to give 1mM solution of the molecule. 0.28 mg of TCEP was dissolved in the DMSO (obtained from Sigma Adlrich) and the solution was allowed to stand for 5 minutes. The gold substrate was cleaned using hydrogen flame



annealing and the sample was soaked in the solution previously prepared. The deposition time was varied (30 mins, 1 hour, 2 hours, 12 hours, overnight). After deposition, the sample was washed with copious amounts of DMSO, deionized water and finally acetone, dried in nitrogen and ellipsometry was performed to find out the thickness of the monolayer. The ellipsometry data is shown in the following figure.

Molecular dynamics mechanics (calculated using ChemDraw 3D) indicate that the length of the molecule should be roughly 18 Å. This figure clearly shows that 30 mins (first data point) deposition time is in closest agreement to what should be the thickness of the film if a monolayer was on the surface of gold. A deposition time of 15 minutes was also tested (data point not shown) but did not show the presence of any molecular layers on the gold surface. Hence the deposition time was maintained at 30 mins for the rest of the experiments.

Molecule 2 was also tested in the same manner as molecule 1. 0.91 mg of the molecule 2 was dissolved on 1 mL DMSO to give 1mM solution of the molecule. 0.28 mg of TCEP was dissolved in the DMSO (obtained from Sigma Adlrich) and the solution was allowed to stand for 5 minutes. The gold substrate was cleaned using hydrogen flame annealing and the sample was soaked in the solution previously prepared. The deposition time was varied (30 mins, 1 hour, 2 hours, 12 hours, overnight). After deposition, the sample was washed with co-

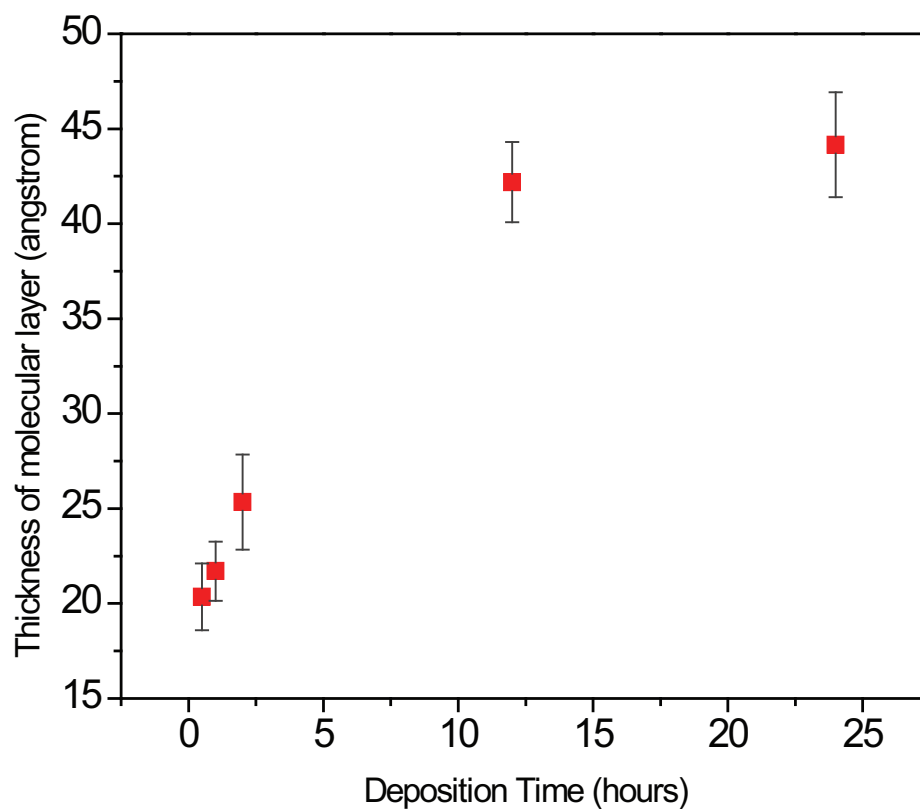


Figure 5.3: Ellipsometry data of molecule 1 deposited on gold. The deposition times were varied from 30 minutes to overnight and the thickness of the layer was measured for after deposition.

pious amounts of DMSO, deionized water and finally acetone, dried in nitrogen and ellipsometry was performed to find out the thickness of the monolayer. The ellipsometry data is shown in the figure 5.3. Molecular mechanics predicted the height of molecule 2 to be 18 Å as well. Ellipsometry data suggested that the optimal deposition time for molecule 2 was also 30 minutes.

Once the samples were prepared, the electronic measurements were done on them

immediately. Samples are not allowed to stand any longer than the normal time required for taking measurements. Samples are discarded after the measurements and not stored as the molecules may undergo chemical decomposition and then give erroneous results in subsequent measurements. The surface, once exposed to atmosphere may also undergo various changes or dirt may accumulate on the surfaces and hence a new surface is tested every time.

#### *Molecular conductance measurements*

Once the monolayers of the molecule on gold were obtained, the next step was to perform electronic measurements on them. The solvent in all cases was freshly distilled, oxygen-free mesitylene (obtained from Sigma Aldrich). Mesitylene was the solvent of choice because of its inert nature, high boiling point and low conductivity resulting in very low leakage current. The solvent was distilled before each use to ensure the removal of contaminants and bubbled with ultra-pure argon to make it free from oxygen. The STM tip was prepared from gold wire by electrochemical etching with hydrochloric acid and ethanol. The prepared STM tip was scanned with an optical microscope before use. The probe is surveyed for the presence of a "double tip" at the end which would lead to faulty images. If the tip appears symmetrical and tapers off at the end, then it is assumed that it has a single atom at the end (although this is not visible due to the resolution of the optical microscope) and is suitable for STM measurements. After etching, the tip

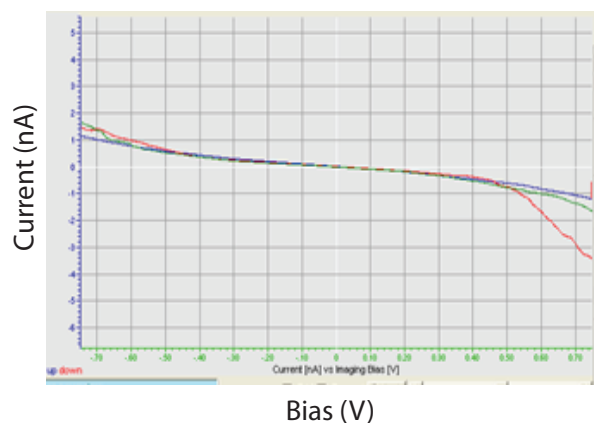


Figure 5.4: I-V curves of molecule 1 on gold

was cleaned with a mixture of concentrated sulfuric acid and hydrogen peroxide, mixed in a ratio of 3 : 1 by volume (all chemicals obtained from Sigma Aldrich) and washed with copious amounts of deionized water. The sample was prepared according to the procedure explained in the previous section. The sample was clamped onto the STM stage with the help of screws and a teflon cell positioned on it was filled with mesytilene to ensure the molecules being measured were in a liquid environment. The STM tip was connected to the scanner and approached to the sample surface at -0.5 V tip bias. Once the set-point current of 0.2 nSiemens was reached, the gold surface was scanned to obtain an image. The image indicated that the surface and the tip were sufficiently clean for conducting measurements. Then the tip was positioned on a flat terrace on the surface, the servo was disconnected and the voltage was scanned across a set range and the I-V characteristics were collected. This was repeated at several places on the surface. The gold tip was

approached at a tip bias of -0.5 Volts. The current set-point was varied from 0.2 nS to 1.8 nS in a step wise manner, incrementing progressively by 0.2 nS. The purpose of varying the current set-point was to bring the tip closer to the molecules. In STM measurements, the actual distance between the tip and the surface is not known and the distance is maintained by the current set-point. If the tip is too far away from the surface (as it probably is at a set point of 0.1 nA), there is gap between the tip and the molecules and the I-V curves do not give a true indication of the molecular characteristics. If the gap between the tip and molecule is too small (as it is at a current set point of 1.8 nS and above) the tip punches through the molecular layer and shorts the circuit by connecting directly with the gold. Hence, I-V curves were taken at various set points to find the optimal tip-molecule distance. For both sets of molecules, it was found to be around 1.4 nS. During an I-V sweep, the servo was temporarily cut-off and the voltage was swept from 0.7 volts to -0.7 Volts. Voltage sweeps beyond  $\pm 0.75$  gave results that were not reproducible hence the sweep was restricted to  $\pm 0.75$  Volts. Several locations on the surface was tested at each set point. This ensures the reproducibility of the data and is a proof of the fact that the results obtained are not artifacts due to surface contaminants. Approximately 200 curves were obtained at each set-point value. Some of them were perfectly symmetrical while some showed rectification as shown in figure 5.4. Molecule 2 also showed similar I-V curves but the number

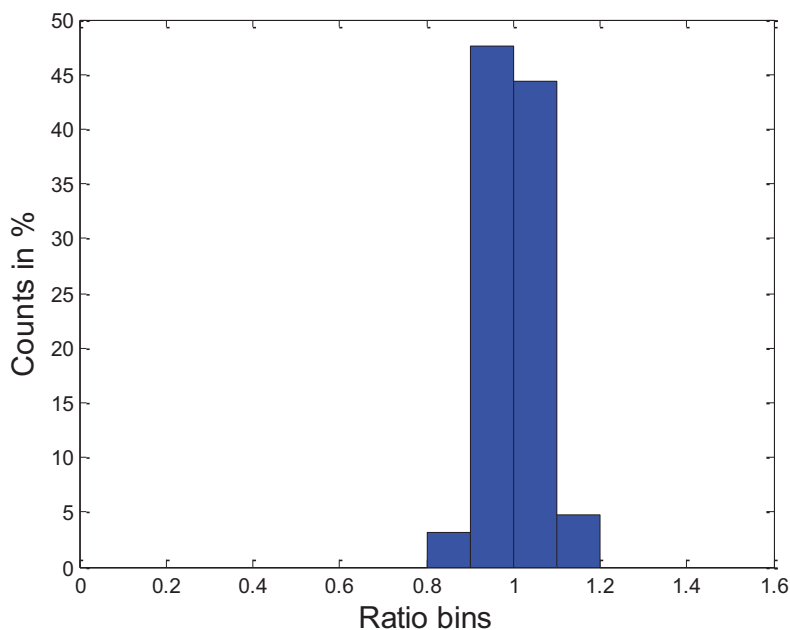


Figure 5.5: Distribution of  $\frac{I_{-0.7V}}{I_{+0.7V}}$  for the current set-point of 0.2 nS. The gold probe is not in contact with the molecules and no rectification is observed. Total number of curves analyzed = 200.

of curves showing rectification was greater.

### *Data Analysis*

Since the molecules 1 and 2 did not show any difference in the direction of rectification but only in the degree of rectification, a data analysis was performed to construct histograms of the percentage of rectification in the molecules. Data analysis was performed using a custom program written in Matlab. All the data sweeps at a particular current set-point were collected and the current at positive bias ( $I_{posbias}$ ) and current at negative bias ( $I_{negbias}$ ) was obtained. For both molecule 1 and 2, that particular voltage set-point was kept at 0.7 Volts. This particular bias was chosen as the rectification was clearly visible at this point.

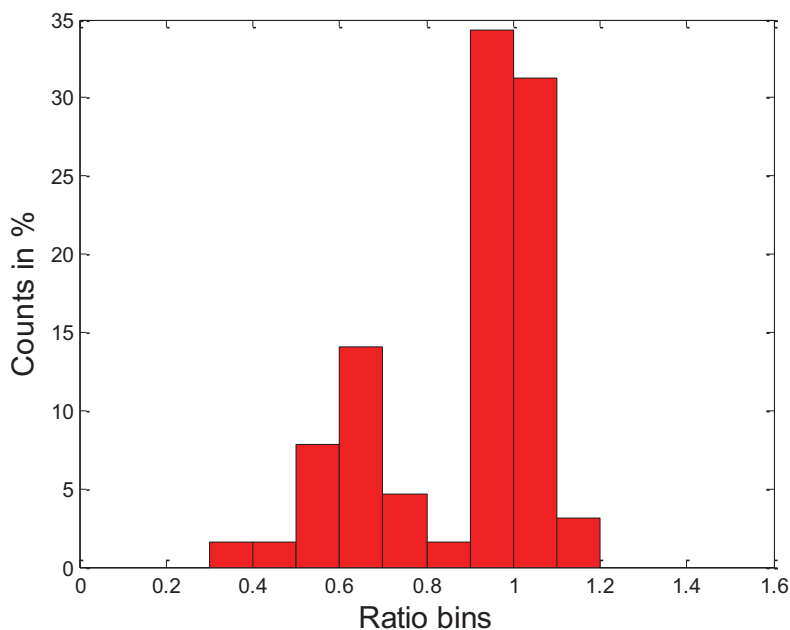


Figure 5.6: Distribution of  $\frac{I_{-0.7V}}{I_{+0.7V}}$  for the current set-point of 1.4 nS for molecule 1. The gold probe is in contact with the molecules and some degree of rectification is observed. The percentage of molecules showing rectification is  $14 \pm 3$  %. Total number of curves analyzed = 200.

Moreover, the molecules were stable and the data was without noise/ chemical alteration at this set point. Then the value of  $\frac{I_{negbias}}{I_{posbias}}$  was calculated for each of these curves. If the value of  $\frac{I_{posbias}}{I_{negbias}}$  was unity that meant that the curves were perfectly symmetric and hence not rectifying. However if  $\frac{I_{negbias}}{I_{posbias}}$  was lesser or greater than unity, then the curves were not symmetric and not rectifying. It was found that all the curves that were rectifying had the value of  $\frac{I_{negbias}}{I_{posbias}} < 1$ . In order to plot the data, the absolute value of  $\frac{I_{negbias}}{I_{posbias}}$  was calculated and binned to form histograms. Shown below are the data histograms for molecule 1. It was observed (as seen in figure 5.5) that at set point 0.2 nS, there is no rectification observed. The rea-

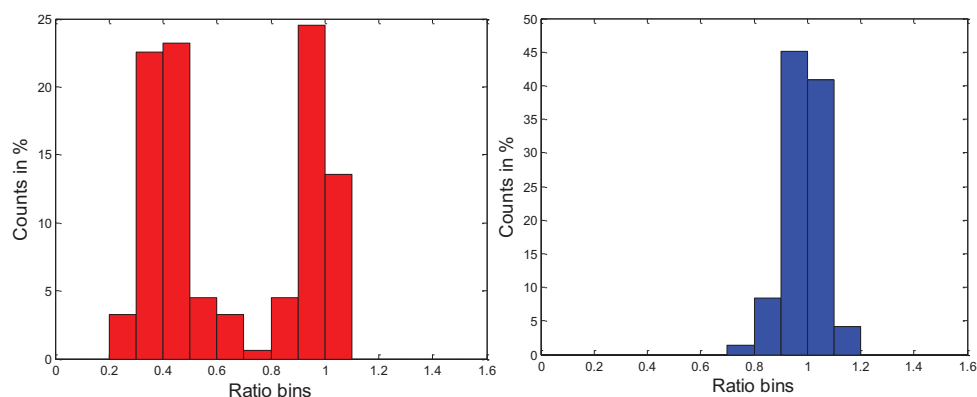


Figure 5.7: Distribution of  $\frac{I_{-0.7V}}{I_{+0.7V}}$  for the current set-point of 1.4 nS for molecule 2 (in red) and control of molecule 2 at 0.2 nS (in blue). The gold probe is in contact with the molecules at 1.4 nS and rectification is observed. The percentage of molecules showing rectification is  $25 \pm 2$  %. Total number of curves analyzed = 200 for each histogram.

son for this is the probe is not in direct contact with the molecules at this point.

Due to the gap between the probe and the molecules, the tunneling through the gap dominates the I-V characteristics. Therefore, the properties of the molecule was not observed at this set-point. At a set-point of 1.4 nS, the situation changes (see figure 5.6). There was a dramatic increase in the number of molecules showing rectification. Due to the current and the distance signals being convoluted in



the STM, there was no way to precisely predict the actual distance of the probe from the surface. But the onset of rectifying curves was a good indication that the probe was in contact with the molecules. Moreover, at higher set-points, the probes punched through the surface and came in contact with the gold substrate. However, for molecule 1, there was still a significant fraction of the molecules that were non-rectifying and showed perfectly symmetric I-V curves. For molecule 2, the fraction of molecules showing rectification was increased. The percentage of molecules showing rectification was around  $25 \pm 2$  % (see figure 5.7). Each set of measurements were repeated at least three times under identical conditions until reproducible data was obtained. Hence molecule 2 was more rectifying than molecule 1, just by the virtue of reversal of the direction of the amide bond.

### 5.3 Conclusion

The reversal of the direction of the amide bond changes the mode of electron transport through the molecules. It also dictates the conformational changes and the voltage through the molecules changes. Hence the I-V characteristics of the molecule 1 is different from molecule 2, the later being more rectifying than the former. Hence unimolecular rectification based on intramolecular stereochemical changes is observed and backed by computational evidence.

## Chapter 6

### Conclusion

This chapter will go into the conclusions drawn from projects one and two, the limitations and possible future directions of research.

#### 6.1 Conclusion of project one

Chapters 3 and 4 show a novel stage that generates reproducible conductance data for STM measurements under illumination. Chapter 3 explains the development and perfection of a method to collect and analyze the conductance data obtained from break-junction measurements on Dyad molecules on ITO. Chapter 4 illustrates that a significant fraction of the Dyads show an enhanced conductance state under illumination. This is due to a long-lived charge separated state that appears only on the ITO surface and opens up avenues for construction and charge extraction from novel photovoltaics.

#### 6.2 Future directions of project one

One of the limitations of the work was the inability to determine, with certainty, whether the pyridine end or the carboxylic acid end of the Dyad molecules were binding to the ITO. This is potentially an important problem as the binding of the end groups may dictate the charge injection into the ITO. Future research can be directed towards characterizing the nature of the Dyad-ITO binding in order

to establish the proper mechanism of charge injection from the molecule into the ITO.

### 6.3 Conclusion of project two and future directions

Chapter 5 concludes with the finding of a molecular rectifier showing statistically significant rectification behavior independent of dipole orientation. This not only matches theoretical predictions but is immensely important for photovoltaic applications as it will prevent charge recombination, thereby increasing the efficiency of the device. This opens up a lot of possibilities in terms of future directions for experiments with different sets of molecules. It is also worthwhile to test the same molecules but with hetero-junctional electrodes (by using platinum STM probes) and observe changes to the degree of rectification.

## BIBLIOGRAPHY

- Andreasen, G., M. E. Vela, R. C. Salvarezza, and A. J. Arvia (1997, December). Dynamics of pyridine adsorption on gold(111) terraces in acid solution from in-situ scanning tunneling microscopy under potentiostatic control. *Langmuir* 13(25), 6814–6819. [72]
- Armstrong, N. R., C. Carter, C. Donley, A. Simmonds, P. Lee, M. Brumbach, B. Kippelen, B. Domercq, and S. Yoo (2003, December). Interface modification of ito thin films: organic photovoltaic cells. *Thin Solid Films* 445(2), 342–352. [48, 54]
- Ashwell, G. J., W. D. Tyrrell, and A. J. Whittam (2004, June). Molecular rectification: self-assembled monolayers in which donor-bridge-acceptor moieties are centrally located and symmetrically coupled to both gold electrodes. *Journal of the American Chemical Society* 126(22), 7102–7110. [99]
- Aviram, A. and M. A. Ratner (1974, November). Molecular rectifiers. *Chemical Physics Letters* 29(2), 277–283. [16, 97, 98]
- Battacharyya, S., A. Kibel, G. Kodis, P. A. Liddell, M. Gervaldo, D. Gust, and S. Lindsay (2011, January). Optical modulation of molecular conductance. *Nano Letters* 0(0), 1–5. [62, 68, 70, 73, 74, 81, 84, 85, 86, 91, 95]
- Baykul, M. C. (2000, May). Preparation of sharp gold tips for stm by using electrochemical etching method. *Materials Science and Engineering B* 74(1-3), 229–233. [9]
- Berger, R., E. Delamarche, H. P. Lang, C. Gerber, J. K. Gimzewski, E. Meyer, and H.-J. Gantherodt (1997, June). Surface stress in the self-assembly of alkanethiols on gold. *Science* 276(5321), 2021–2024. [2]
- Berlin, A., G. Zotti, G. Schiavon, and S. Zecchin (1998, December). Adsorption of Carboxyl-Terminated dithiophene and terthiophene molecules on ito electrodes and their electrochemical coupling to polymer layers. the influence of molecular geometry. *Journal of the American Chemical Society* 120(51), 13453–13460. [54]
- Binnig, G., C. Quate, and C. Gerber (1986). Atomic force microscope. *Physical review letters* 56(9), 930–933. [13]
- Binnig, G. and H. Rohrer (1983, March). Scanning tunneling microscopy. *Surface Science* 126(1-3), 236–244. [6]

- Bird, R. and C. Riordan (1984). Simple solar spectral model for direct and diffuse irradiance on horizontal and tilted planes at the earth's surface for cloudless atmospheres. Technical report, Solar Energy Research Inst., Golden, CO (USA). [34]
- Brabec, C. J. (2004, June). Organic photovoltaics: technology and market. *Solar Energy Materials and Solar Cells* 83(2-3), 273–292. [41]
- Cai, W.-B., L.-J. Wan, H. Noda, Y. Hibino, K. Ataka, and M. Osawa (1998, November). Orientational phase transition in a pyridine adlayer on gold(111) in aqueous solution studied by in situ infrared spectroscopy and scanning tunneling microscopy. *Langmuir* 14(24), 6992–6998. [72]
- Chen, F., J. He, C. Nuckolls, T. Roberts, J. E. Klare, and S. Lindsay (2005, March). A molecular switch based on potential-induced changes of oxidation state. *Nano Letters* 5(3), 503–506. [28, 75]
- Chen, F., Z. Huang, and N. Tao (2007). Forming single molecular junctions between indium tin oxide electrodes. *Applied Physics Letters* 91(16), 162106. [53, 56, 61]
- Chen, F., X. Li, J. Hihath, Z. Huang, and N. Tao (2006, December). Effect of anchoring groups on Single-Molecule conductance: A comparative study of thiol-, amine-, and carboxylic-acid-terminated molecules. *Journal of the American Chemical Society* 128(49), 15874–15881. [24, 30, 31, 61]
- Commoner, B. (1976). *Poverty of power: energy and the economic crisis*. [33]
- Currie, M. J., J. K. Mapel, T. D. Heidel, S. Goffri, and M. A. Baldo (2008, July). High-Efficiency organic solar concentrators for photovoltaics. *Science* 321(5886), 226–228. [41]
- Dhirani, A.-A., R. W. Zehner, R. P. Hsung, P. Guyot-Sionnest, and L. R. Sita (1996, January). Self-assembly of conjugated molecular rods: A high-resolution stm study. *Journal of the American Chemical Society* 118(13), 3319–3320. [3]
- Evers, F., F. Weigend, and M. Koentopp (2004, June). Conductance of molecular wires and transport calculations based on density-functional theory. *Physical Review B* 69(23), 235411. [20]
- Fan, F.-R. F., J. Yang, L. Cai, Price, S. M. Dirk, D. V. Kosynkin, Y. Yao, A. M.

- Rawlett, J. M. Tour, and A. J. Bard (2002, May). Charge transport through self-assembled monolayers of compounds of interest in molecular electronics. *Journal of the American Chemical Society* 124(19), 5550–5560. [3]
- Fthenakis, V., J. E. Mason, and K. Zweibel (2009, February). The technical, geographical, and economic feasibility for solar energy to supply the energy needs of the us. *Energy Policy* 37(2), 387–399. [39]
- Fujihira, M., M. Suzuki, S. Fujii, and A. Nishikawa (2006). Currents through single molecular junction of Au/hexanedithiolate/Au measured by repeated formation of break junction in STM under UHV: effects of conformational change in an alkylene chain from gauche to trans and binding sites of thiolates on gold. *Physical Chemistry Chemical Physics* 8(33), 3876. [28]
- Gardner, T. J., C. D. Frisbie, and M. S. Wrighton (1995, July). Systems for orthogonal self-assembly of electroactive monolayers on au and ito: an approach to molecular electronics. *Journal of the American Chemical Society* 117(26), 6927–6933. [48, 54]
- Gervaldo, M., P. A. Liddell, G. Kodis, B. J. Brennan, C. R. Johnson, J. W. Bridgewater, A. L. Moore, T. A. Moore, and D. Gust (2010). A photo- and electrochemically-active porphyrin-fullerene dyad electropolymer. *Photochemical & Photobiological Sciences* 9(7), 890. [95]
- Gore, A. and T. Peters (1993). Creating a government that works better & costs less: The report of the national performance review. [33]
- Gratzel, M. (2004, June). Conversion of sunlight to electric power by nanocrystalline dye-sensitized solar cells. *Journal of Photochemistry and Photobiology A: Chemistry* 164(1-3), 3–14. [46]
- Green, M. (1993). Polycrystalline silicon solar cells. *Renewable energy: sources for fuels and electricity*, 337. [36]
- Green, M. A. (2002, April). Photovoltaic principles. *Physica E: Low-dimensional Systems and Nanostructures* 14(1-2), 11–17. [37]
- Gust, D. and T. A. Moore (1989, April). Mimicking photosynthesis. *Science* 244(4900), 35–41. [15, 49]
- Gust, D., T. A. Moore, and A. L. Moore (2000, November). Photochemistry of

- supramolecular systems containing c60. *Journal of Photochemistry and Photobiology B: Biology* 58(2-3), 63–71. [51]
- Gust, D., T. A. Moore, A. L. Moore, D. Kuciauskas, P. A. Liddell, and B. D. Halbert (1998, June). Mimicry of carotenoid photoprotection in artificial photosynthetic reaction centers: triplet-triplet energy transfer by a relay mechanism. *Journal of Photochemistry and Photobiology B: Biology* 43(3), 209–216. [49]
- Halls, J. J. M., K. Pichler, R. H. Friend, S. C. Moratti, and A. B. Holmes (1996). Exciton diffusion and dissociation in a poly(p-phenylenevinylene)-c60 heterojunction photovoltaic cell. *Applied Physics Letters* 68(22), 3120. [43]
- Haugeneder, A., M. Neges, C. Kallinger, W. Spirk, U. Lemmer, J. Feldmann, U. Scherf, E. Harth, A. Götz, and K. Müllen (1999, June). Exciton diffusion and dissociation in conjugated polymer-fullerene blends and heterostructures. *Physical Review B* 59(23), 15346. [43]
- He, J. and S. M. Lindsay (2005). On the mechanism of negative differential resistance in ferrocenylundecanethiol self-assembled monolayers. *Journal of the American Chemical Society* 127(34), 11932–11933. [99]
- He, J., O. Sankey, M. Lee, N. Tao, X. Li, and S. Lindsay (2006). Measuring single molecule conductance with break junctions. *Faraday Discussions* 131, 145. [21, 29, 60]
- Hipps, K. W. (2001, October). It's all about contacts. *Science* 294(5542), 536–537. [27]
- Hockett, L. A. and S. E. Creager (1993). A convenient method for removing surface oxides from tungsten STM tips. *Review of Scientific Instruments* 64(1), 263. [8]
- Hohenberg, P. and W. Kohn (1964, November). Inhomogeneous electron gas. *Physical Review* 136(3B), B864. [20]
- Kodis, G., P. A. Liddell, A. L. Moore, T. A. Moore, and D. Gust (2004, September). Synthesis and photochemistry of a carotene porphyrin fullerene model photosynthetic reaction center. *Journal of Physical Organic Chemistry* 17(9), 724–734. [90]
- Kuciauskas, D., S. Lin, G. R. Seely, A. L. Moore, T. A. Moore, D. Gust, T. Drovets-

- skaya, C. A. Reed, and P. D. W. Boyd (1996, January). Energy and photoinduced electron transfer in porphyrin-fullerene dyads. *The Journal of Physical Chemistry* 100(39), 15926–15932. [51]
- Lee, M. H., G. Speyer, and O. F. Sankey (2006, July). Electron transport through single alkane molecules with different contact geometries on gold. *physica status solidi (b)* 243(9), 2021–2029. [24]
- Li, X., J. He, J. Hihath, B. Xu, S. M. Lindsay, and N. Tao (2006, February). Conductance of single alkanedithiols: Conduction mechanism and effect of Molecular Electrodes contacts. *Journal of the American Chemical Society* 128(6), 2135–2141. [28]
- Liddell, P. A., J. P. Sumida, A. N. Macpherson, L. Noss, G. R. Seely, K. N. Clark, A. L. Moore, T. A. Moore, and D. Gust (1994, December). Preparation and photophysical studies of porphyrin-C<sub>60</sub> dyads. *Photochemistry and Photobiology* 60(6), 537–541. [50]
- Lindsay, S. M. (2010). *Introduction to nanoscience*. Oxford University Press, USA. [11, 20]
- Marcus, R. A. (1956). On the theory of oxidation-reduction reactions involving electron transfer. i. *The Journal of Chemical Physics* 24(5), 966. [25]
- McDonald, A. and L. Schrattenholzer (2001, March). Learning rates for energy technologies. *Energy Policy* 29(4), 255–261. [33]
- Milliron, D. J., I. G. Hill, C. Shen, A. Kahn, and J. Schwartz (2000). Surface oxidation activates indium tin oxide for hole injection. *Journal of Applied Physics* 87(1), 572. [48, 65]
- Mueller, K. (2006, January). Effect of the atomic configuration of gold electrodes on the electrical conduction of alkanedithiol molecules. *Physical Review B* 73(4), 045403. [24]
- Mujica, V., M. A. Ratner, and A. Nitzan (2002, August). Molecular rectification: why is it so rare? *Chemical Physics* 281(2-3), 147–150. [98]
- Nagahara, L. A., T. Thundat, and S. M. Lindsay (1989, October). Preparation and characterization of stm tips for electrochemical studies. *Review of Scientific Instruments* 60(10), 3128. [9]



- Nitzan, A. (2001, February). Electron transmission through molecules and molecular interfaces. *cond-mat/0102300*. [17]
- Nuzzo, R. G. and D. L. Allara (1983, June). Adsorption of bifunctional organic disulfides on gold surfaces. *Journal of the American Chemical Society* 105(13), 4481–4483. [2]
- O'Regan, B. and M. Gratzel (1991, October). A low-cost, high-efficiency solar cell based on dye-sensitized colloidal tio<sub>2</sub> films. *Nature* 353(6346), 737–740. [45]
- Osada, T., T. Kugler, P. Brams, and W. R. Salaneck (1998, July). Polymer-based light-emitting devices: investigations on the role of the indium–tin oxide (ito) electrode. *Synthetic Metals* 96(1), 77–80. [48, 65]
- Pagliaro, M., R. Ciriminna, and G. Palmisano (2008, November). Flexible solar cells. *ChemSusChem* 1(11), 880–891. [41]
- Parks, J. J., A. R. Champagne, G. R. Hutchison, S. Flores-Torres, H. D. Abruña, and D. C. Ralph (2007, July). Tuning the kondo effect with a mechanically controllable break junction. *Physical Review Letters* 99(2), 026601. [27]
- Poirier, G. E. (1997, June). Characterization of organosulfur molecular monolayers on au(111) using scanning tunneling microscopy. *Chemical Reviews* 97(4), 1117–1128. [3]
- Ratner, M. A. (2002, February). Introducing molecular electronics. *Materials Today* 5(2), 20–27. [15]
- Reed, M. A., C. Zhou, C. J. Muller, T. P. Burgin, and J. M. Tour (1997, October). Conductance of a molecular junction. *Science* 278(5336), 252–254. [27]
- Schoenfish, M. H. and J. E. Pemberton (1998, May). Air stability of alkanethiol self-assembled monolayers on silver and gold surfaces. *Journal of the American Chemical Society* 120(18), 4502–4513. [3]
- Slowinski, K., R. V. Chamberlain, C. J. Miller, and M. Majda (1997, December). Through-bond and chain-to-chain coupling. two pathways in electron tunneling through liquid alkanethiol monolayers on mercury electrodes. *Journal of the American Chemical Society* 119(49), 11910–11919. [23]

- Strachan, D. R., D. E. Smith, D. E. Johnston, T. Park, M. J. Therien, D. A. Bonnell, and A. T. Johnson (2005). Controlled fabrication of nanogaps in ambient environment for molecular electronics. *Applied Physics Letters* 86(4), 043109. [27]
- Sugiyama, K., H. Ishii, Y. Ouchi, and K. Seki (2000). Dependence of indium tin oxide work function on surface cleaning method as studied by ultraviolet and x-ray photoemission spectroscopies. *Journal of Applied Physics* 87(1), 295. [48, 65]
- Tao, N. J. (2006, December). Electron transport in molecular junctions. *Nat Nano* 1(3), 173–181. [23]
- Tomfohr, J. and O. F. Sankey (2004). Theoretical analysis of electron transport through organic molecules. *The Journal of Chemical Physics* 120(3), 1542. [20, 22]
- Venkataraman, L., J. E. Klare, I. W. Tam, C. Nuckolls, M. S. Hybertsen, and M. L. Steigerwald (2006, March). Single-molecule circuits with well-defined molecular conductance. *Nano Letters* 6(3), 458–462. [23]
- Visoly-Fisher, I., K. Daie, Y. Terazono, C. Herrero, F. Fungo, L. Otero, E. Durantini, J. J. Silber, L. Sereno, D. Gust, T. A. Moore, A. L. Moore, and S. M. Lindsay (2006, June). Conductance of a biomolecular wire. *Proceedings of the National Academy of Sciences* 103(23), 8686–8690. [30]
- Vitousek, P. M., J. D. Aber, R. W. Howarth, G. E. Likens, P. A. Matson, D. W. Schindler, W. H. Schlesinger, and D. G. Tilman (1997, August). Human alteration of the global nitrogen cycle: sources and consequences. *Ecological Applications* 7(3), 737–750. [34]
- Voss, D. (2000). Cheap and cheerful circuits. *Nature* 407(6803), 442–444. [15]
- Waldeck, D. H. and D. N. Beratan (1993, July). Molecular electronics: Observation of molecular rectification. *Science* 261(5121), 576–577. [97]
- Wang, W., T. Lee, and M. A. Reed (2003, July). Mechanism of electron conduction in self-assembled alkanethiol monolayer devices. *Physical Review B* 68(3), 035416. [23]
- Wang, Z.-S., C.-H. Huang, F.-Y. Li, S.-F. Weng, and S.-M. Yang (2001, May).

- Photosensitization of nanocrystalline  $\text{TiO}_2$  electrodes with ii b group metal-ion-bridged self-assembled films of 3,4,9,10-perylenetetracarboxylic acid. *Journal of Photochemistry and Photobiology A: Chemistry* 140(3), 255–262. [54]
- Williams, M. C., J. P. Strakey, and W. A. Surdoval (2005, April). The U.S. department of energy, office of fossil energy stationary fuel cell program. *Journal of Power Sources* 143(1-2), 191–196. [33]
- Wu, C. C., C. I. Wu, J. C. Sturm, and A. Kahn (1997). Surface modification of indium tin oxide by plasma treatment: An effective method to improve the efficiency, brightness, and reliability of organic light emitting devices. *Applied Physics Letters* 70(11), 1348. [48, 65]
- Xu, B. and N. J. Tao (2003). Measurement of single-molecule resistance by repeated formation of molecular junctions. *Science* 301(5637), 1221 –1223. [28, 61]
- Yan, C., A. Zharnikov, and M. Grunze (2000, July). Preparation and characterization of self-assembled monolayers on indium tin oxide. *Langmuir* 16(15), 6208–6215. [48, 54]
- Zahran, S., S. D. Brody, A. Vedlitz, M. G. Lacy, and C. L. Schelly (2008). Greening local energy: Explaining the geographic distribution of household solar energy use in the united states. *Journal of the American Planning Association* 74(4), 419–434. [35, 36]
- Zhang, J., Q. Chi, A. M. Kuznetsov, A. G. Hansen, H. Wackerbarth, H. E. M. Christensen, J. E. T. Andersen, and J. Ulstrup (2002, February). Electronic properties of functional biomolecules at metal/aqueous solution interfaces. *The Journal of Physical Chemistry B* 106(6), 1131–1152. [90]
- Zotti, G., G. Schiavon, S. Zecchin, A. Berlin, and G. Pagani (1998, March). Adsorption of ferrocene compounds on indium tin oxide electrodes. enhancement of adsorption by decomposition of ferrocenium molecules by oxygen. *Langmuir* 14(7), 1728–1733. [54]